GRAIN BOUNDARY MICROSTRUCTURE EFFECTS ON STRESS CORROSION CRACK INITIATION MECHANISMS IN ALLOY 600 AND ALLOY 690

Technical Milestone Report: M2LW-19OR0402031
September 2019

Z. Zhai, M. B. Toloczko, M. J. Olszta, and S. M. Bruemmer
Pacific Northwest National Laboratory

Research Project:
Stress Corrosion Crack Initiation of
Nickel-Base Alloys in LWR Environments
Project Manager: S. M. Bruemmer
Pacific Northwest National Laboratory

Conducted for:
Office of Nuclear Energy, U.S. Department of Energy
Light Water Reactor Sustainability Program
Materials Aging and Degradation Pathway
Pathway Manager: T. M. Rosseel
Oak Ridge National Laboratory

Table of Contents

Project Background

Objective

This research project addresses one of the least understood aspects of stress corrosion cracking (SCC) for light-water reactor (LWR) pressure boundary components - crack initiation. The focus of the work is to investigate important material (composition, processing, microstructure, strength) and environmental (temperature, water chemistry, electrochemical potential, stress) effects on the SCC susceptibility of corrosion-resistant, nickel-base alloys. The primary objectives are to identify mechanisms controlling crack nucleation, investigate the transition from short to long crack growth in these alloys under realistic LWR conditions and help establish the framework to effectively model and mitigate SCC initiation processes.

Approach

Alloy 600 materials were selected for the first phase of SCC initiation experimentation followed by testing on the more resistant Alloy 690 materials. For both alloys, material variants known to influence SCC response are being examined including cold/warm work (forged, rolled and tensile strained), banded/inhomogeneous microstructures (plate versus extruded tubing), grain boundary precipitation (heat-to-heat variations, mill-annealed, solution annealing and changes due to thermal treatments) and surface grinding (various damage depths, surface roughness and nanocrystalline layers). Materials and material conditions have been identified and obtained from an ongoing research project for the U.S. Nuclear Regulatory Commission (NRC) where stress-corrosion crack growth has been characterized, thus creating an important link between SCC initiation and propagation behavior. Detailed examinations have been performed using optical and electron microscopy to establish key bulk and surface microstructural features that may act as initiation precursors. Dedicated test systems with continuous in-situ detection of crack formation were designed and constructed enabling SCC initiation experimentation of a range of Alloy 600 and 690 materials. After SCC testing in high temperature autoclave systems, surface and near-surface characterizations were conducted to document nano-to-microscale initiation precursors leading to macroscopic stress corrosion cracks. The fundamental understanding of how the near-surface microstructure is degraded during high-temperature water exposure is essential to an improved predictive methodology for SCC initiation. Collaborations with ongoing PNNL projects supported by the NRC and EPRI play an important role in our research and has enabled testing on Alloy 600/690 and Ni-base alloy weld metals.

Focus of Current Report

Grain boundary (GB) microstructure, especially carbide distribution is one of the most important material variables influencing intergranular SCC behavior of Ni-base alloys. Although GB carbides have been demonstrated to improve resistance to SCC propagation for thermally treated (TT) Alloy 600 in hydrogenated PWR primary water, it remains unclear whether they have the

same effect on SCC initiation in Alloy 600. In addition, the influence of GB carbides on SCC behavior of Alloy 690 is of critical importance since data has been generated suggesting that solution-annealed (SA) material in the highly cold-worked (CW) condition is more resistant to SCC growth that TT materials. As a result, a better understanding on the GB carbide effects is necessary to predict possible long-term degradation in these alloys. This report summarizes the systematic studies carried out in FY19 on the effect of GB microstructure on precursor damage development and crack initiation in CW Alloys 600 and 690.

For Alloy 600, the GB microstructure effects were evaluated on an Alloy 600 heat in mill-annealed (MA), SA and TT conditions. These materials were 15% CW and SCC initiation response was investigated by constant load testing in simulated PWR primary water. Direct current potential drop (DCPD) technique was used for in situ detection of crack initiation. With periodic examination of the specimens, morphological and dimensional evolution of precursor damage including intergranular attack and short cracks was carefully documented and compared to data obtained from an EPRI program in which unstressed coupons with the same material conditions were exposed to the same environment. Results revealed a predominant role of mechanical factors in the development of precursor damage with no apparent improvement in SCC initiation resistance due to grain boundary carbides.

For Alloy 690, SCC initiation behavior continues to be evaluated by long-term constant load testing in simulated PWR primary water. Seven commercial Alloy 690 heats with different starting microstructures and cold-work levels are being tested at either 90% or 100% of the material yield stress. Previous studies have revealed GB cavity formation after 7,110 to 9,220 hours of exposure in some highly CW Alloy 690TT heats, serving as precursors to intergranular cracking. While the ongoing test evaluates multiple thermal histories, this report refines the scope to provide a detailed summary on GB cavity evolution from ~9,220 to ~28,000 hours in four Alloy 690TT heats in 21% and 31%CW conditions that have been characterized most extensively using scanning electron microscopy and transmission electron microscopy. It is demonstrated that even all in the TT condition, small differences in GB carbide size and spacing can lead to significantly differences in GB cavity formation and growth. Link-up of GB cavities has led to formation of long internal creep cracks, resulting in crack initiation detected by DCPD in a highly CW Alloy 690TT heat with a uniform, semi-continuous distribution of small GB carbides. In comparison, highly CW Alloy 690TT materials featuring larger and more widely spaced GB carbides did not show a significant increase in GB cavity density or size, nor were internal IG cracks identified after 28,000 hours of test exposure.

Experimental Methods

Unstressed Exposure Tests for Alloy 600

Corrosion tests on unstressed specimens were conducted in simulated PWR primary water to assess material condition effects on IGA in collaboration with a recent EPRI project [1] at PNNL. Three material conditions were evaluated: as-received, mill annealed (MA); solution annealed (SA) at 1100°C and thermally treated (SA+TT) at 705°C. Circular plate coupons prepared using electric discharge machining (EDM) that were ~15 mm in diameter and ~5 mm in thickness (Figure 2A) were used for the unstressed exposure tests. All surfaces of the as-machined coupons were removed with coarse SiC paper to eliminate contaminants introduced by the EDM process (S and Cu in particular). Both flat surfaces were then polished to 600 grit SiC and one side was further polished to an electron backscatter diffraction (EBSD) quality finish with 50 nm colloidal silica. In total three heats were evaluated, but the results presented herein focus on heat NX6106XK-11 since SCC initiation tests have only been performed for this heat. Coupons were produced from each material condition in triplicate with the intention of extracting one coupon from each material set at different exposure times of 1000 hours, 4400 hours and ~20,000 hours. The final exposure is still ongoing and has reached 16,000 hours at the time of this report. The fully assembled coupon tree installed into the stainless-steel autoclave is shown in Figure 1B. Coupons were suspended individually with a Pt wire wrapped in a ceramic sheath to prevent galvanic coupling. The edge of each coupon was also engraved with the sample name to confirm the material heat and thermomechanical history. A summary table of the coupons from the heat NX6106XK-11 and their exposure times are identified in Table 1.

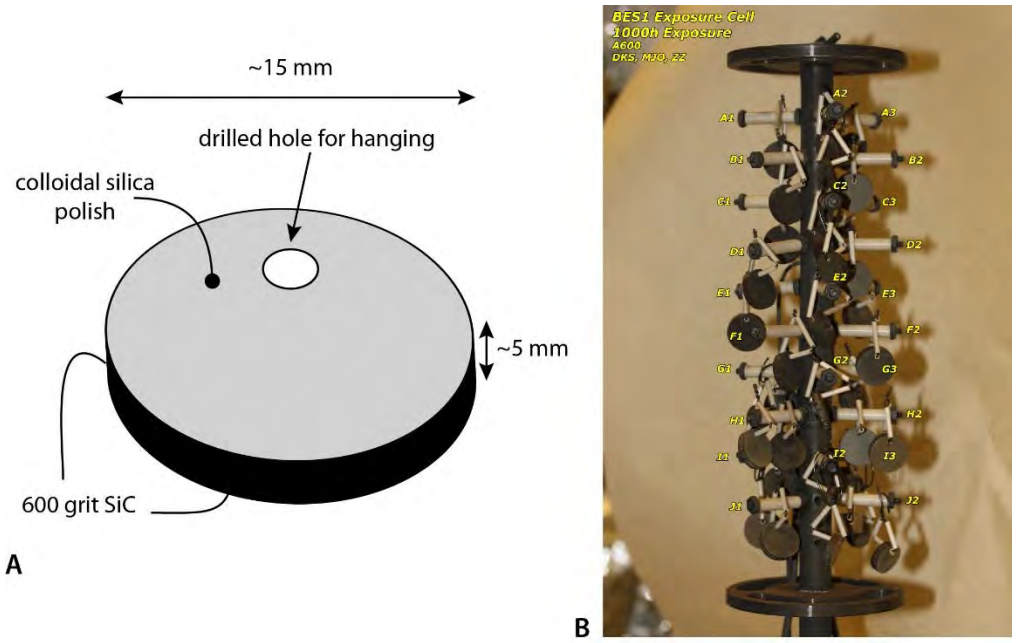

Figure 1. (A) Schematic illustration of the exposure coupon geometry and respective surface finishes. (B) Photograph of the exposure coupons on the tree mounted into the stainless autoclave. Coupons of each material condition were produced in triplicate and each coupon is suspended from the exposure tree by ceramic-encased Pt wire strung through a drilled hole.

Table 1. Summary of Alloy 600 heat NX6106XK-11 exposure coupons. Each row corresponds to an individual coupon of the indicated material condition and time exposed to 360°C simulated PWR primary water.

Thermal History	Cold Work	Time (h)
SA	0	1000
SA	0	4400
SA	0	16000+*
SA+TT	0	1000
SA+TT	0	4400
SA+TT	0	16000+
MA	15%	1000
MA	15%	4400
MA	15%	16000+
SA	15%	1000
SA	15%	4400
SA	15%	16000+
SA+TT	15%	1000
SA+TT	15%	4400
SA+TT	15%	16000+

* Ongoing exposure as of August 2019.

The water chemistry was established at 1000 ppm B and 2 ppm LiOH to simulate PWR primary water with temperature maintained at 360°C to facilitate accelerated testing of the IG corrosion/oxidation response. The electrochemical potential was set at the Ni/NiO line using a dissolved concentration of 25 cc H_2/kg H_2O where IGA/SCC susceptibility is expected to be maximized. At each target exposure time, the autoclave was cooled and drained then one coupon from each material condition was extracted, rinsed and dried for destructive examinations. The remaining coupons were returned to the autoclave to resume exposure to longer times.

SCC Initiation Tests for Alloys 600 and 690

Specimen Design and Surface Preparation

A key goal for this program is to correlate SCC initiation response to various aspects of materials processing including bulk microstructure, near surface microstructure, surface texture, existence of surface defects and applied stress level. Prior experience with alloys 600 and 690 has shown that their SCC resistance is extremely sensitive to the degree of plastic deformation, and therefore accurate characterization in the test specimen was an important factor in the specimen design. Several different specimen types were considered for the crack initiation testing including U-bend, bent beam, tensile, and blunt-notch compact tension (CT) geometries.

A tensile specimen geometry was the most attractive because it has none of the shortcomings associated with U-bend, bent beam and blunt-notch specimens. This design produces a uniaxial stress state, the gauge region is accessible allowing control over the surface microstructure, various types of micro/macroscopic defects can be generated and there are several ways to produce specimens with well-known amounts of uniform plastic strain. In addition, prior work at KAPL [2] has shown that DCPD can be effectively used to detect crack initiation. Several factors played into the specific design of the tensile specimens employed for SCC initiation testing [3], the most important was maximizing the ability of DCPD to detect crack initiation. The DCPD signal is affected not only by crack growth, but also by elastic and plastic strains including creep. Initiation tests are typically conducted at or near the yield stress where small amounts of creep occur at PWR primary water temperatures. To reduce the magnitude of the creep contribution to the DCPD signal, the gauge length was kept as short as possible while allowing a sufficient number of grain boundaries to be exposed. The short gauge length also played favorably for the desire to be able to fully survey the specimen gauge surface for cracks by scanning electron microscopy (SEM) in a reasonable length of time. This characterization is essential to assess crack precursors and the transition from intergranular attack (IGA) to micro-crack nucleation to short crack growth in Alloy 600. In addition, one practical issue was the desire to have an initiation specimen size that fit within the dimensions of a 0.5T CT specimen such that any material prepared for SCC crack growth studies could also be used for SCC crack initiation studies. The final tensile design was refined to the point that a crack initiation specimen could be cut from an SCC-tested 0.5T CT specimen as long the crack length to width ratio (a/W) in the CT specimen did not exceed 0.7. This a/W is below the range of typical crack lengths in SCC studies conducted by PNNL allowing routine extraction of crack initiation specimens as desired. Other factors for the design were the need to electrically isolate the specimen and eliminate any significant stress risers.

The effect of resistivity change on the DCPD signal for Ni-base alloys exposed to PWR relevant temperatures was measured and subtracted from the gauge signal. This was accomplished by monitoring a larger diameter region of the specimen where the stress is approximately 15% of the gauge stress (depending on gauge diameter). For this low stress region, neither crack initiation nor any substantial amount of creep will occur and the inherent resistivity change of the material can be measured. The specimen dimensions along with a photo of the specimen are shown in Figure 2. After taking into account all design considerations, a 30.5 mm tall tensile specimen with a 4.0 mm gauge length was selected.

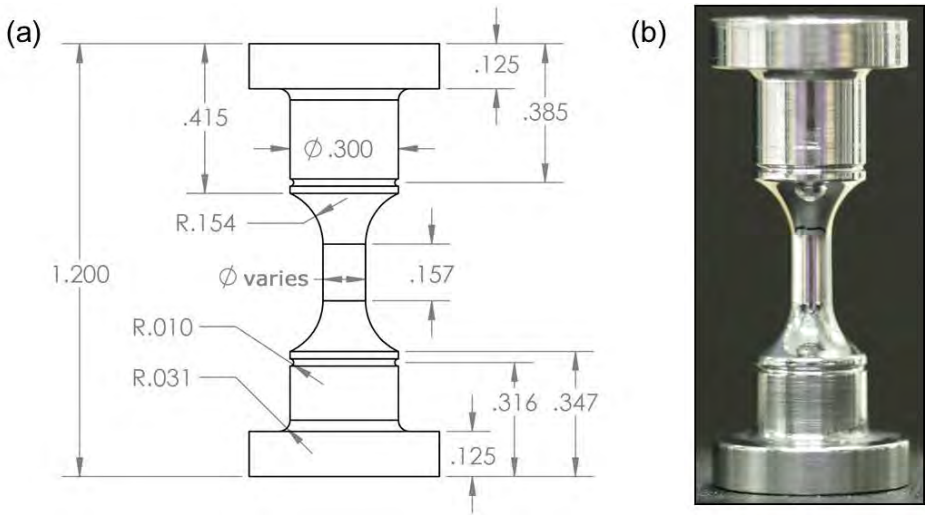

Figure 2. PNNL initiation specimen design. Gauge diameter is selected based on material strength and can be varied from 2.75-4.5 mm (0.11-0.18 inches) and the gauge length is 4.0 mm (0.157 inches). Overall height is 30.5 mm (1.2 inches).

Materials have been tested in various material conditions with or without cold work. Cold working was typically achieved either by cold rolling or cold forging. Cold rolling performed on the plate material was done such that the rolling direction was the same direction as the original plate processing direction. Specimens taken from CRDM tubing were cut with the gauge axis parallel to the CRDM tubing axis. The gauge axis of specimens cut from the plate material was parallel to the "S" direction relative to the plate processing. Prior to insertion of the specimens into the autoclave, the gauge section either was polished to a 1 μm finish or was rough ground. A "C" finish used for some of the specimens attempts to emulate the surface damage layer created by typical service component grinding operations [4]. The details of the surface preparation procedure have been provided elsewhere [5, 6]. Generally, aggressive grinding produces a nanocrystalline layer that promotes corrosion across the entire surface and delays water access to bulk grain boundaries. This has been found to have a small effect on initiation times as discussed in earlier publications [5, 7]. In comparison, a highly polished surface ensures that all grain boundaries reaching the surface are immediately exposed to water. From an examination perspective, a ground surface impairs observation of surface cracks due to the rough surface and microscale fold-overs that often have a crack-like appearance. A polished surface eliminates these complicating factors and enables a better optical and SEM assessment of IGA and crack nucleation as a function of the material, environment and test conditions, therefore most specimens tested after 2015 were given a highly polished surface finish.

Test Methods

Figure 3 shows the load train and DCPD instrumentation for the typical SCC initiation specimen set up at PNNL. Currently two smaller SCC initiation systems and one large SCC initiation system are being used under the scope of LWRS. The two small SCC initiation systems have been converted to test up to 6 fully instrumented specimens during the past year, and the large

SCC initiation system allows 36 specimens be tested simultaneously with up to 24 specimens instrumented. The load frame in both types of systems is designed to sustain the load even when individual specimens fail during the test enabling the test to continue for the other specimens loaded in the same string. To make this possible, the controlling software is programed to partially unload the system when a sharp strain increase in an individual specimen is detected by DCPD. The load decrease (typically to ~80% of the starting value) enables the SCC-initiated tensile specimen to fail safely without significantly impacting the entire system. After the failure of the specimen is confirmed (usually by losing DCPD signal), the load is brought back to yield stress again while monitoring stress versus strain curve using DCPD for every specimen. It is important to note that none of the LWRS Alloy 600 or Alloy 690 specimens have been allowed to fail during an SCC initiation test and all specimens have been removed shortly after DCPD-indicated initiation to assess cracking.

A reversing DCPD technique developed by General Electric [8] and KAPL [9] was adapted with the configuration shown in Figure 4. DCPD voltage across the gauge section is sensitive not only to reduction in cross-sectional area of the gauge region due to crack formation, but also to changes in gauge length and diameter from creep strains that occur during testing. Resistivity drift caused by exposure of Alloy 600 or Alloy 690 at elevated temperature can also produce a substantial contribution to the DCPD signal. In order to minimize the impact of the latter on DCPD data, a reference voltage was also measured across a thick section where significant creep strain and SCC initiation would not occur, and this was subtracted from the gauge voltage. Since creep deformation is believed to have the primary influence on the resistivity-corrected DCPD signal up to the point of initiation, it was decided to report the DCPD response as a strain value. A formula for strain as a function of voltage starts first with the dependence of voltage on gauge dimensions:

$$V = \rho(L/A) \cdot I \tag{1}$$

V is the measured voltage, ρ is the material resistivity, L is the distance between measurement points, A is the cross-sectional area and I is the applied current. Because plastic strain (including creep) is volume conservative, the relationship can be rewritten as:

$$V = (\rho/v)L^2 \cdot I \tag{2}$$

where v is the volume of material between the voltage measurement points. By rearranging this equation to solve for L and inserting it into the equation for true strain ($\varepsilon = \ln(L/L_o)$), strain is obtained as a function of voltage from the following formula:

$$\varepsilon_{\text{referenced}} = \frac{1}{2}\left[\ln\left(\frac{V_{\text{gauge}}}{V_{\text{gauge}_0}}\right) - \ln\left(\frac{V_{\text{ref}}}{V_{\text{ref}_0}}\right)\right] \tag{3}$$

where $\varepsilon_{\text{referenced}}$ is the resistivity corrected creep strain, and "gauge" and "ref" are measurements across the gauge section and reference region, respectively.

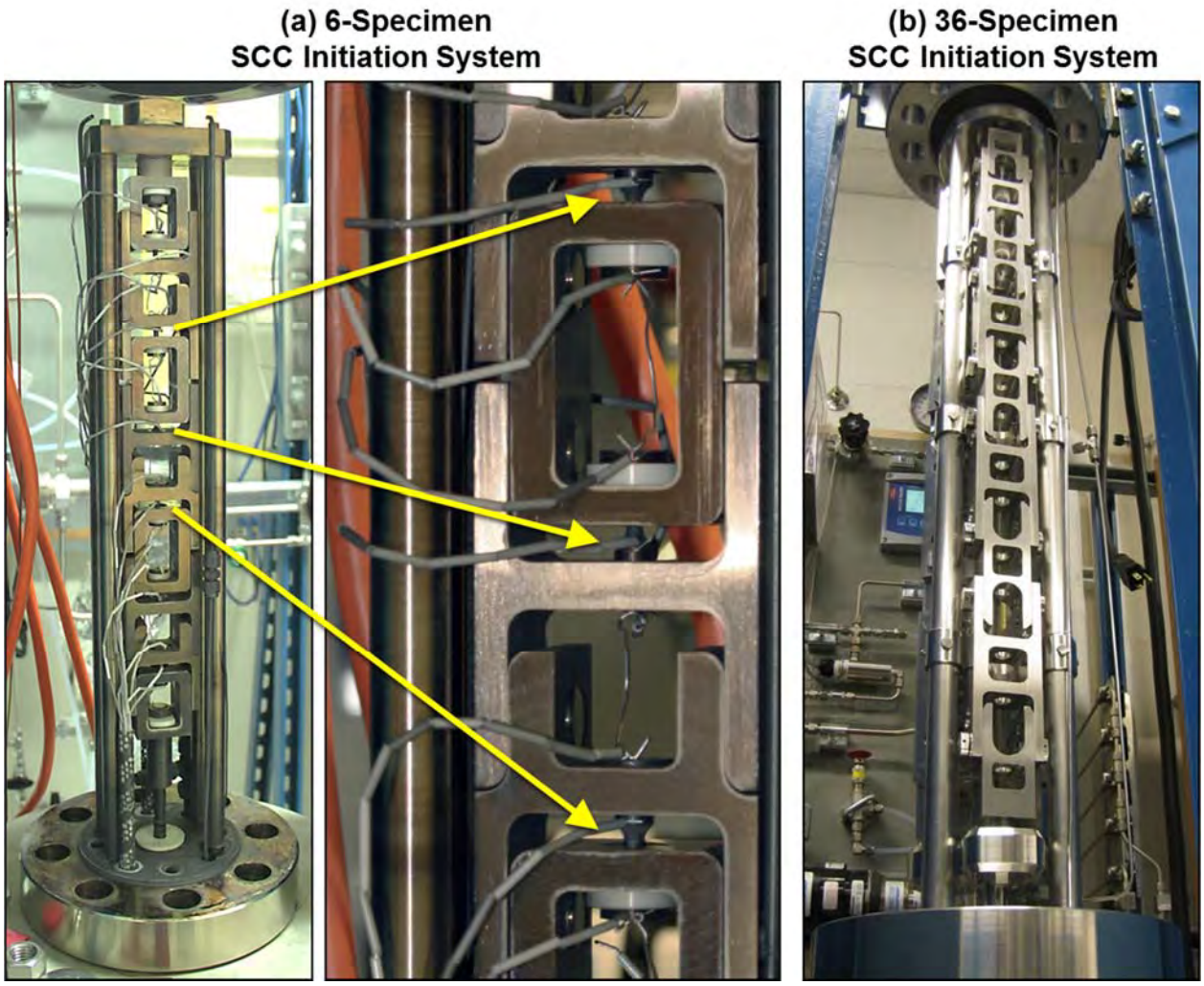

Figure 3. Crack initiation test system load train at PNNL in the (a) small SCC initiation test system with capacity of testing up to 6 fully instrumented specimens and the (b) large SCC initiation test system with capacity of testing up to 24 instrumented specimens and up to 36 specimens in total.

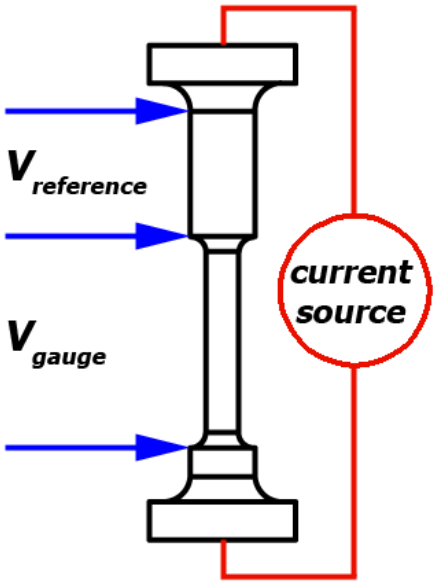

Figure 4. Sketch of the tensile specimen showing desired DCPD measurement points.

Due to the difficulty of spot-welding the wires for DCPD at the idealized voltage measurement points, the actual voltage pickup points were at slightly different locations. The deviation in voltage from idealized pickup points was assessed using finite element modeling (FEM), and a simple linear correction factor as a function of gauge diameter was found to compensate for the non-ideal voltage measurement points. Further details on the development of this DCPD technique can be found in Ref. [10].

Most SCC initiation tests were conducted in an environment that simulates the PWR primary water (1000 ppm B, 2 ppm Li) at 360°C and 20.4 MPa with a dissolved hydrogen concentration of 25 cc/kg to maintain a electrochemical corrosion potential (ECP) at the Ni/NiO stability line. Test temperature effects on SCC initiation have also been evaluated on selected Alloy 600 materials and the dissolved hydrogen content adjusted to maintain the ECP at the Ni/NiO stability. Nearly all specimens have been tested at their yield stress under constant load with a small number evaluating the influence of lower applied stresses. Full load was applied to the specimens within 1-2 days of reaching the test temperature enabling specimens to be pre-oxidized before loading. At the start of a test, the target load (the load at ~0.2% plastic strain) was achieved over a period of ~1 hour at a constant strain rate of ~10^{-5} mm/s. This rate was chosen to load specimens to their yield stress sufficiently fast to reduce the risk for SCC formation during the initial loading. It also allows DCPD to monitor the stress-strain evolution with a sufficiently low noise level during this loading step. As shown in Figure 5, one specimen would sometimes yield slightly earlier than the others in a multi-specimen load train system due to intrinsic difference in yield strength and/or gauge diameter. In this case, small amounts of plastic strain up to ~1.5% were allowed in order to achieve yield in the other specimens. The specimens were then held at actively controlled constant load until crack initiation. All relevant environmental parameters and DCPD data were monitored and continuously written to a file. If

a test was interrupted for surface examinations of precursor damage, or if a specimen had exhibited crack initiation, the remaining specimens were taken back to their original load upon restart of the test, again while monitoring stress versus strain during loading. Figure 6 shows the evolution of both non-referenced and referenced strains throughout exposure of a plate specimen. As mentioned in the previous section, by subtracting the reference voltage from the gauge voltage, the contribution of resistivity drift is eliminated in the referenced strain response. While creep and cracking are both likely to be simultaneously contributing to the measured response, the SCC initiation time is determined as any obvious increase in strain rate. Tests were stopped after clear confirmation of DCPD-based initiation to allow detailed characterizations of the specimen just after the onset of initiation as well as any accompanying specimens that had not yet initiated.

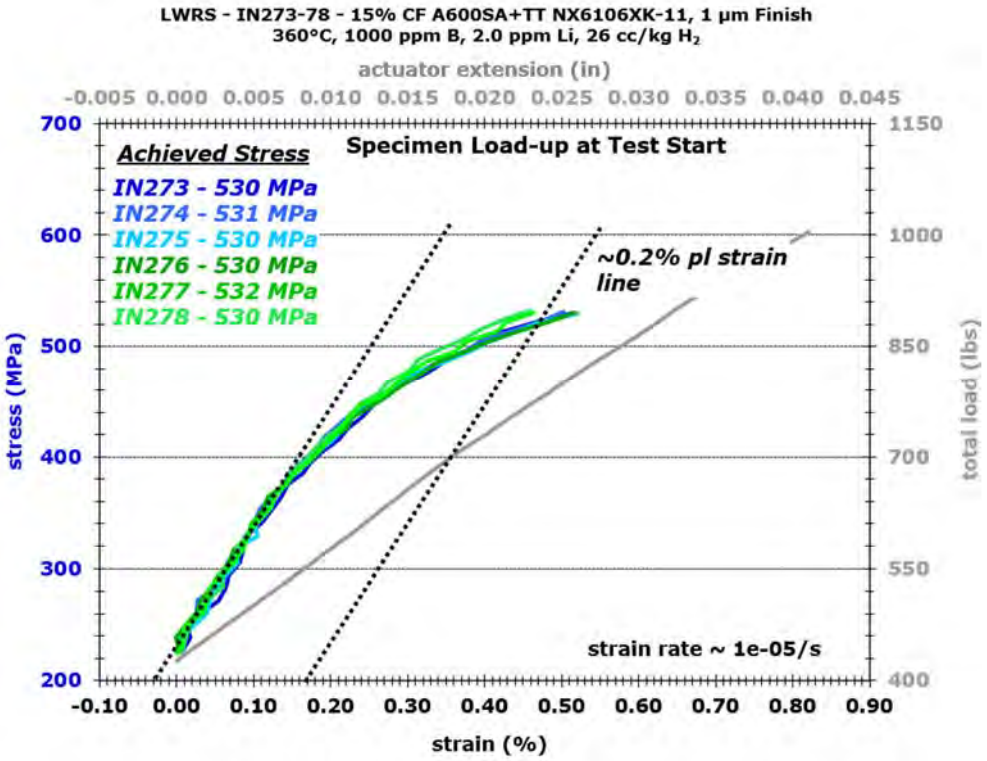

Figure 5. Example of stress versus strain plot during initial loading of tensile specimens for SCC initiation testing. The displacement in actuator and the total load is plotted in the secondary x (upper) and y (right) axis, respectively.

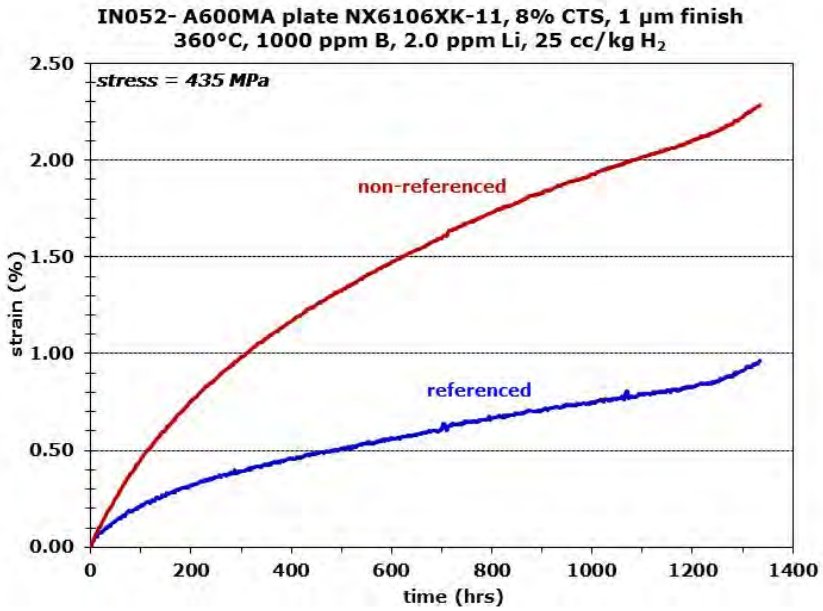

Figure 6. Non-referenced and referenced DCPD strain response for IN052, an 8%CW specimen from Alloy 600MA plate heat NX6106XK-11.

Microstructural Characterizations

The microstructural characterizations focus mainly on acquiring morphological and quantitative information of IGA and cracks for further analyses. Most examination was performed using a JEOL 7600 scanning electron microscope (SEM) in the backscatter electron (BSE) mode. The characterization procedure for each test will be detailed in the following sections. Supplementary high-resolution characterizations by transmission electron microscopy (TEM) and atom probe tomography (APT) were also performed on a subset of the specimens as part of the collaborative EPRI project. These exams were conducted to better understand the IG corrosion/oxidation behavior as a function of GB chemistry and are reported elsewhere [11].

Examination of Alloy 600 Unstressed Exposure Coupons

The exposure coupons taken out at each test interruption were cut in half using EDM. One half of each coupon was mounted into epoxy and mechanically polished to a "mirror finish" using colloidal silica for SEM examinations in cross-section. It is critical to ensure that the edge of the cross-sections do not curve during mechanical polish, otherwise it will easily lead to inaccurate measurements of the depth (usually less than 2 µm) of IGA located on these edges. To accomplish this, the cross-sectioned coupons were clamped between two stainless steel fixture plates like a sandwich using coiled spacers (Figure 7). The whole set was then mounted into epoxy and polished to an EBSD quality finish with 50 nm colloidal silica. The material of the stainless steel plates had a similar hardness as the test coupons so that material was removed evenly during polishing to provide a sufficiently flat edge for reliable IGA depth measurement. The other half was left unmounted to enable more facile preparation of TEM and APT specimens as needed.

Low acceleration voltage was used during SEM imaging to reveal detailed compositional contrast of the IGA. For each examined coupon, the IGA depth measurements were performed on at least 50, as many as 120, neighboring high-energy GBs. This provides a representative sample size for statistical analysis. In addition, the IGA morphology at some GBs were documented at higher magnifications enabling comparisons between material conditions and exposure times.

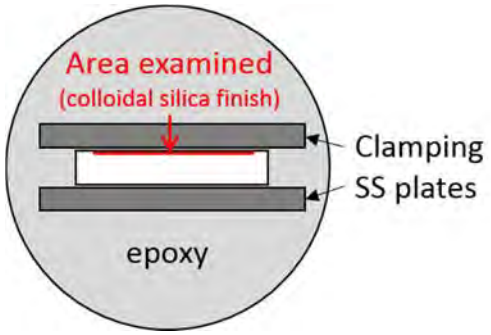

Figure 7. Schematic of the mounted exposure coupons for cross-section examination. In this study, only the side with a colloidal silica finish on the surface was examined.

In supplementary of the SEM observations, transmission scanning microscopy and atom probe tomography were performed on representative IGA in selected coupons. Dual-beam FIB/SEM systems (either Thermo Fischer Quanta or Helios) were used to make site-specific specimens for higher-resolution characterization by TEM and APT. Each specimen was protected by a bilayer of electron-beam and ion-beam deposited Pt. Sculpting of the TEM foil and APT needles used a 30 kV Ga^+ ion beam followed by low energy 2 kV Ga^+ cleanup to minimize ion-beam damage. Further details on FIB liftout procedures can be found elsewhere [12-14]. Analytical TEM characterization was accomplished by energy dispersive x-ray spectroscopy (EDS) with a JEOL JEM ARM 200CF equipped with a Centurio EDS detector and a high-angle annular dark field (HAADF) detector. APT characterization utilized a CAMECA LEAP 4000X HR operated in laser pulsing mode (λ = 355 nm) [15]. The APT base temperature and pressure were 40 K and < 2E-11 Torr, respectively. The CAMECA IVAS software package (version 3.8.0) was used to reconstruct and analyze the APT data. Error bars in the APT concentration profiles indicate 1σ from standard counting error as $\sigma_i = \sqrt{c_i(100 - c_i)/N_T}$ where c_i is the measured concentration of element i and N_T is the total number of atoms in the sampled volume.

Examination of Alloy 600 SCC Initiation Specimens

One key focus of this study is to evaluate the evolution of precursor damage and crack formation in the Alloy 600 having different thermomechanical histories. Therefore periodical examinations were performed on the surface and cross-section of SCC initiation specimens at ~480 hours, ~1000 hours and whenever it is necessary to remove initiated specimens before they fail in the system. More specifically, the surface examination was performed on all specimens after each test interruption using a JEOL 7600 SEM. Oxford Aztec software was used to automate stage movement such that the entire gauge surface could quickly be mapped enabling montages to be

created. In order to achieve this, four fiducial scribe marks (90° to one another) were made at the button ends of each specimen to keep track of the specimen orientation. Each of the four orientations was then mapped using high-keV BSE montage imaging so that features covered by thin surface oxides can be revealed. As shown in Figure 8, the surface of the entire gauge section and most of the fillet region of the specimens was examined on each rotation.

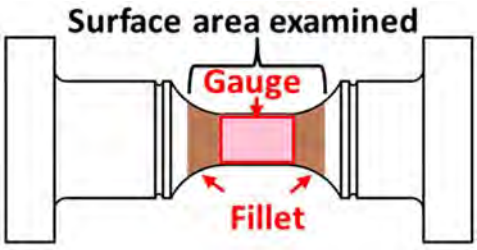

Figure 8. Schematic of the surface area of one rotation mapped in SEM for pre-test examination. The gauge surface mapped in SEM is highlighted in pink and the surface in the fillet region mapped in SEM is highlighted in taupe.

Destructive examinations for precursor damage was also performed in one SCC initiation specimen removed at every test interruption. The specimens for this observation were sliced into two halves along axial direction using EDM with one half mounted into epoxy and carefully polished to an EBSD quality finish with 50 nm colloidal silica. Similar to the observation conducted on the cross-section of unstressed exposure coupons, low-keV SEM-BSE imaging was performed on more than 100 neighboring high-energy GBs to reveal detailed compositional contrast of the IGA and to measure their depth.

Examination of Alloy 690 SCC Initiation Specimens

Surface examinations on the gauge and fillet region were routinely performed on all Alloy 690 SCC initiation specimens at test interruptions using the same JEOL 7600F SEM and the same procedure described above for Alloy 600 specimens. To better examine the distribution of GB cavities and IG cracks in the bulk, some specimens were sectioned in half along the axial direction using EDM and the two halves were manually polished to a colloidal silica finish on the cross-sections through a serial polishing procedure. It started with placing the cross-section of the specimens in a vibratory drum and metallographically polishing the face using a sequentially smaller grits of SiC paper (ranging from 240-1200 grit) followed by 9, 6, and 1 µm grit diamond paste in oil, and lastly finishing with a 50 nm colloidal silica solution to remove any latent damage in the sample. High-kV, SEM-BSE montage imaging was first performed on the entire gauge cross-sections followed by low kV, higher resolution imaging at a number of sites that appear to contain GB cavities and IG cracks based on indications from the montage images. Compositional analyses were also carried out when needed using energy dispersive x-ray spectroscopy (EDS). The EDS data was collected using a 170 mm^2 X-max EDS detector (Oxford). In addition, a FEI Quanta field-emission-gun, dual-beam focused-ion-beam (FIB)/SEM system was employed to create shallow trenches to correlate surface and cross-

section morphology on selected features, as well as to prepare site specific TEM samples from cross-sections of highly polished initiation samples post testing.

Since previous post-test examinations on SCC initiation specimens suggested a key role of creep by inducing the formation and growth of grain boundary cavities at carbide interfaces leading to intergranular cracking, the main focus of this report is to quantify the cavity evolution to better investigate the effect of GB microstructure on this process. However, it is clear that high levels of cold work can produce GB damage and complicates the quantitative evaluation of damage evolution during testing in high-temperature water. Therefore, it is crucial to understand how to properly examine and classify this type of damage in the pre-test condition and establish its evolution with time. As a result, we developed observational protocols to best prepare sample surfaces to avoid inducing artifacts and to perform subsequent examinations utilizing SEM, FIB and TEM to assess the formation and development of GB cavities. While the methodology for performing high resolution SEM analysis will be described here, results of characterizations on actual samples will be presented in more details later in the Alloy 690 section.

Determination of Proper Imaging Condition for Precursor Damage Examination

Two of the major sources of subjectivity within SEM are the choice of accelerating voltages as well as the type of signal collected (e.g., secondary versus backscatter). Understanding the interaction volume of an electron beam with a sample is essential for effective SEM analysis. Not only is the interaction volume dependent upon the accelerating voltage important, but the density of the material also plays a large role. The higher the accelerating voltage, the deeper the data can originate from a sample. Conversely, the denser the sample the less the volume probed. Therefore, tailoring the probe parameters in relation to the sample type and required spatial resolution defines the experiment. Additionally, the choice of signal collection and interpretation of the data in relation to the spatial resolution required is necessary for proper analysis. Whereas secondary electrons (SEs) originate from the surface, backscatter electrons and x-rays start at a deeper and from a larger volume. SE contrast, while providing a very good spatial resolution of the surface at nearly all accelerating voltages, can suffer from various artifacts when even slight topography is introduced. A smooth surface with small voids, cracks or interfaces where there is a solid surface adjacent to a region with no material such as a void or crack can act to create bright contrast in the image that could hinder detection of the size and shape of the feature. BSE contrast on the other hand originates deeper into the sample, but typically does not suffer from artefacts created by adjacent voids or cracks. Since the signal depth depends upon the accelerating voltage, it is necessary to take into account the desired feature shape/density in question and tailor the probe conditions. A higher kV probe will sample a deeper region, which can often tend to convolute data. At a higher voltage, a void or crack on the very surface of the sample could be outweighed by the material beneath it (Figure 9).

Therefore, the interaction volume of the desired probe should be calculated in Monte Carlo type simulations such as using the program *Casino* (Figure 10). A plot of the trajectory of 2000 BSEs for accelerating voltages ranging from 5-20 keV in a model Ni60Cr30Fe10 alloy illustrates how

increasing the voltage could drastically change the information observed in a sample if the desired microstructural information is on the order of 10-100s of nanometers.

As shown in Figure 9, the carbides in the highly CW Doosan material range from 1-5 µm and at 7.5 kV, the edges of the carbide are sharp as are the small voids at carbide interfaces and cracks in the carbides. At 20 kV, the edges of the carbides and voids become blurred, and even the thinner parts of the carbides are skewed by the matrix underneath. Additionally, the majority of very small voids adjacent to carbides observed at 7.5 kV have disappeared at 20 kV due to the matrix outweighing the signal. While it can be demonstrated in Figure 9 that latent voids deeper into the sample might be expressed at higher kV, their resolution will always be convoluted by the metal above it and do not provide a better opportunity in observing damage. Being able to appropriately apply this technique to understand GB damage evolution is necessary not only to correctly identify the analyzation parameters, but also determine how to best interpret the signals. As noted, once data has been properly collected, the assignment and definition of contrast can affect the overall analysis.

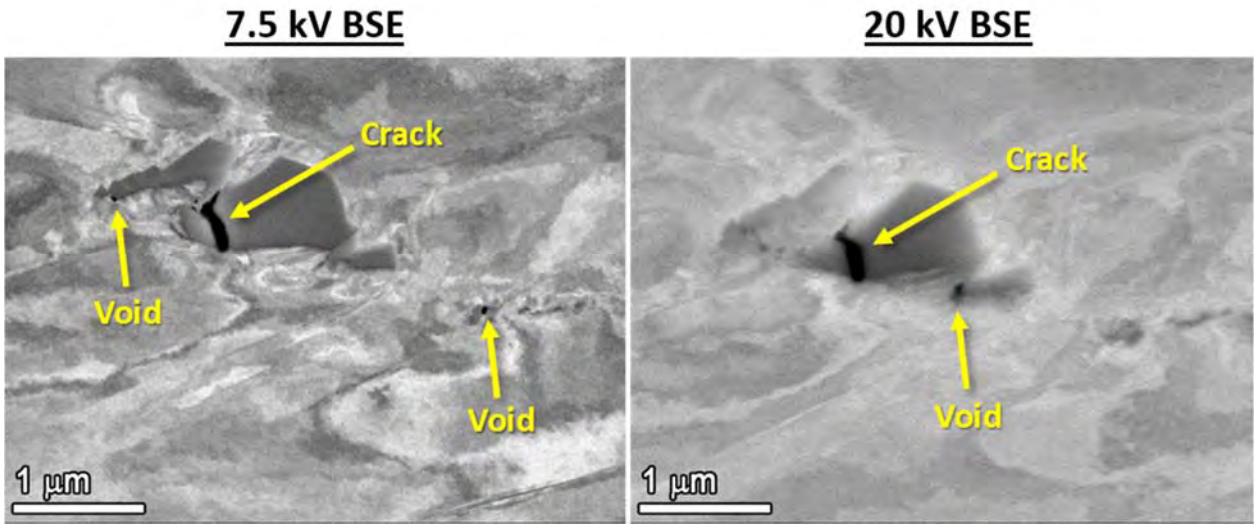

Figure 9. SEM-BSE of the Doosan heat observed at 7.5 kV and 20 kV, illustrating the effect of interaction volume on imaging conditions.

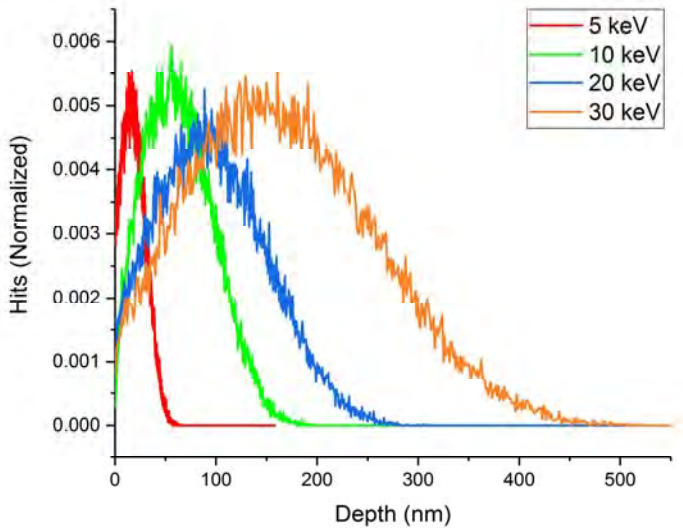

Figure 10. Monte Carlo simulation showing plot of hits versus depth for backscatter electrons in a simulation of Ni60Cr30Fe10 which indicates where BSE signal originates.

Sample Preparation

The additional parameter that needs to be addressed when discussing high resolution SEM analysis is sample preparation. With the increased resolution and detection limits of next generation SEMs being pushed via the utilization of low kV imaging, especially with in-line BSE detection, the requirement for improved surface preparation has become an integral part of fundamental microstructural analysis. Traditional metallographic preparation of metals for SEM consisted of polishing to a "mirror finish", which to the human eye could be to a roughness on the order of micrometers. This translates to a subsurface damage volume approximately on the same order. For higher kV analysis, the interaction volume typically would reach deeper than this damage layer, and any subsurface damage would not be detectable. At lower accelerating voltages, subsurface damage becomes noticeable and will convolute small microstructural changes such as voids or cracks. Therefore, subsequent surface preparation down to colloidal silica or microdiamond polish becomes necessary to reduce the final depth of polishing damage to the order of nanometers.

Aside from assessing the microstructural damage associated with the type of testing, it is important to note and understand common sample preparation artifacts. Metallographic polishing of these alloys for high resolution analysis has become even more stringent based on the advent of low kV analysis. As shown in Figure 10, the use of low kV BSE imaging can provide high resolution analysis due to the very small (20-50 nm) interaction volume of the beam. Therefore, any surface defects induced by sample preparation may be detected. Figure 11 highlights the scale and appearance of two major sample preparation artifacts that are most often observed, namely polishing contamination and remnant colloidal silica.

To achieve the highest possible metallographic finish, it is first necessary to grind the material with increasing finer SiC grit paper. The material removed from the sample surface is most

often transported away in the liquid media utilized (e.g., oil or water), but when the sample in question contains larger cracks such as in a crack growth test, portions of the deformed material can be redeposited. The appearance of redeposited metal is most often observed on the order of 10s of micrometers with contrast close to that of the base metal. The key factor in distinguishing polishing contamination is the inclusion of small, dark, rounded particles on the order of 10s of nanometers to micrometers. SEM-EDS analysis of these particles shows they are typically rich in Cr and O, but also contain Al and Si. EDS elemental maps show the surrounding material is rich in Ni and Fe. SEM analysis of the local composition and microstructure is enough to identify it as polishing contamination for any future sample analysis. This microstructure is almost always observed in larger cracks and has not been identified in small voids/cracks on the order of 10-100s of nanometers.

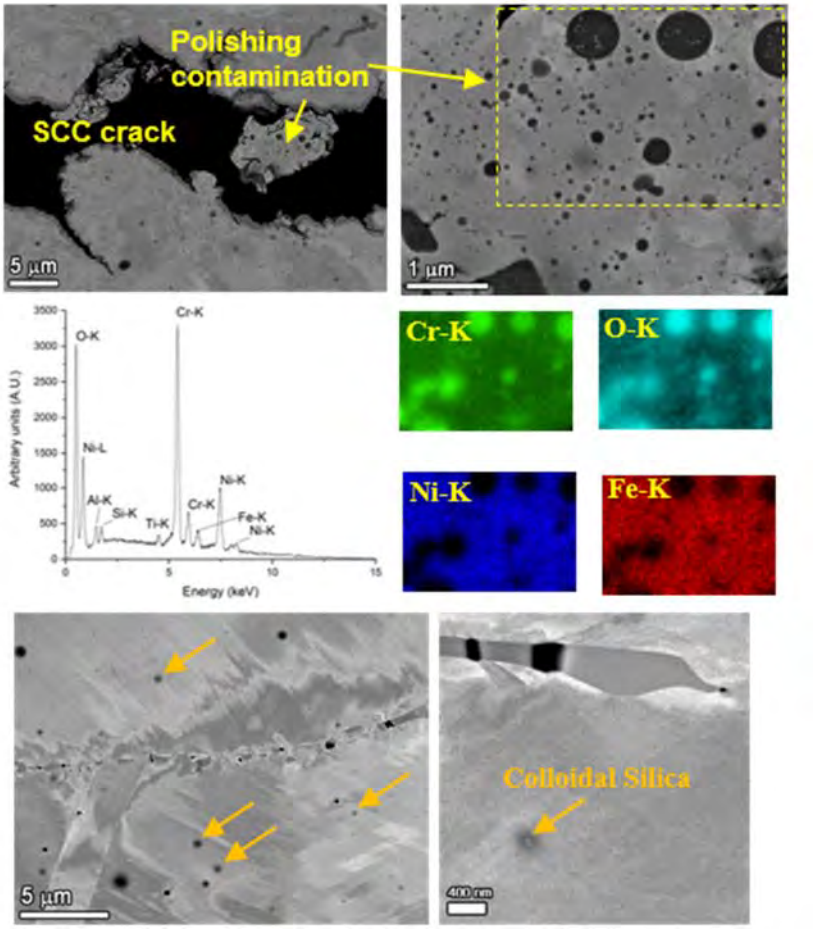

Figure 11. SEM-BSE and EDS elemental mapping of polishing contamination deposited in the middle of an open crack as well as remnant deposition of colloidal silica on the surface (orange arrows).

While increasingly smaller SiC grit can provide a better metallographic polish, colloidal silica is still required to remove the final surface damage imparted by even the finest of SiC grits (e.g., 1200 grit). Colloidal silica works to both slightly etch the surface (depending on the liquid

media) as well as gently mechanically polish via small (100s of nanometers) SiO_2 spheres. Depending on how well the samples are cleaned post preparation, remnant silica spheres may be detected as they are on the order of the interaction volume of the beam at low kV. They are almost always present as singular spheres on the surface and is occasionally detected in smaller cracks as a Si signal in EDS.

The presence of cracked IG carbides (or nitrides) in these alloys also presents a second source of possible sample preparation artifact in the analysis of GB damage, namely precipitate fallout. Beyond comparing regions of various levels of strain assessing cavity formation and crack formation to illustrate a gradient of damage, it is necessary to be able to differentiate the appearance of cracked carbides. In rare instances for these samples, voids were observed from the fallout of a cracked carbide (Figure 12). Such carbide fallout was only observed in the Doosan CRDM Alloy 690 material where the carbides were on the order of micrometers. In the few examples where isolated carbide fallout was detected, the subsurface remaining carbide could be identified, or the adjacent carbide at the surface appeared to be faceted (suggesting the carbide cracked along a crystallographic plane). The presence of the subsurface and faceted carbides suggests that the carbide was most likely already cracked and fell out during the final polishing stages. It should be emphasized that these observations were very rare. While this type of cracked carbide fallout was possible, it was not a major contributor to the presence of detected GB damage.

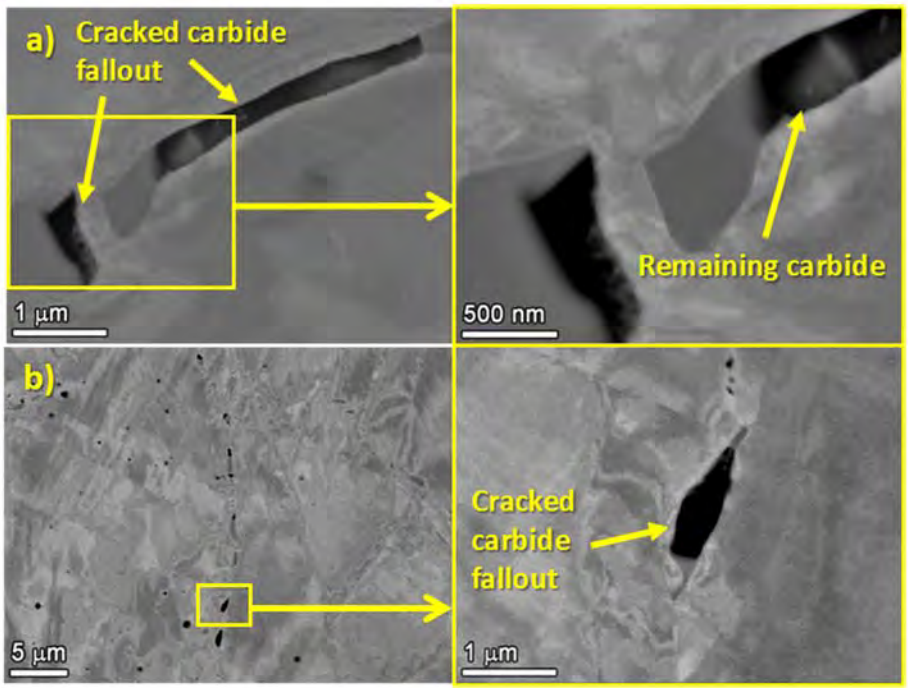

Figure 12. SEM-BSE of highly CW Doosan CRDM Alloy 690 showing examples of carbide fallout as a result of cracked carbides.

Quantification on GB Cavity Evolution

Systematic quantification of GB cavities was also conducted in cross-sectioned specimens to better understand their evolution with a focus on the effect of starting microstructure and applied stress. As described above, great care was taken during specimen preparation to avoid precipitate fallouts, and with image acquisition to differentiate cavities from artefacts to obtain reliable data for analysis. Finite element modeling (FEM) also was performed on selected SCC initiation specimens prior to SEM examination to analyze the stress distribution from the gauge mid-position to the fillet region where a gradually increasing diameter results in a decreased stress. The locations corresponding to an applied stress of 85%, 70%, 50% and 15% of the YS were identified (Figure 13). An area with a fixed size of 150x150 μm^2 near the centerline was selected at each location based on low-magnification montage image where GB cavities were indicated. The size of the squared area was chosen such that multiple grains can be included irrespective of heat. BSE images were acquired along every high-energy GB included in the area using a magnification of 15,000X, which allows sufficient resolution for nm-sized cavities. Low-kV imaging with fixed contrast and brightness was used to prevent any unwanted bias in cavity size due to change in imaging settings. Generally, 100 to 150 images were taken in each area, stitched together and processed in *Image J*, an open source image processing program. While this software can effectively remove most unrelated objects and background in the images, further correction was manually made on erroneous features by comparing the processed images to the original ones. These mainly include unremoved TiN precipitates and surface contamination that produced a contrast similar to that of the cavities, as well as partially missing cavities due to accumulation of polish remnants. More details on this topic can be found in a previous publication [16]. Upon completion of image processing on the GBs, data on the number and size of the cavities were automatically collected using *Image J*. Two parameters, cavity density and cavity coverage, were chosen to quantify the distribution of GB cavities using expressions listed below:

$$\text{Cavity density} = \frac{\sum \text{number of IG cavities}}{\text{GB length}} \quad (1)$$

$$\text{Cavity coverage} = \frac{\sum \text{height of IG cavities}}{\text{GB length}} \ \% \quad (2)$$

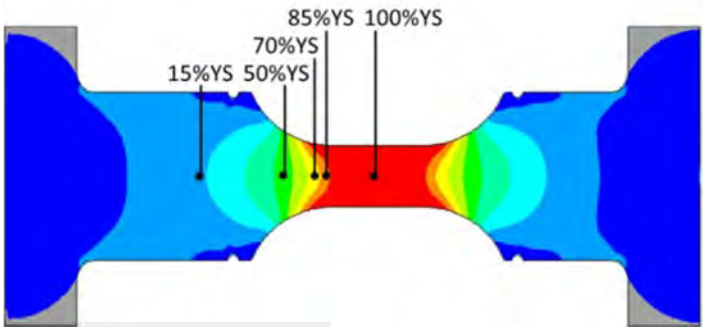

Figure 13. FEM analysis of the Von Mises stress distribution in the specimen when the gauge section is loaded at yield stress.

Evaluation of Grain Boundary Microstructure Effects on SCC Initiation in Alloy 600

Materials and Pre-Test Microstructure

As described in prior milestones reports [6, 17-19], extensive SCC initiation testing has been performed on five different Alloy 600 heats in various cold-worked conditions. The current work focuses on one heat (NX6106XK-11) because of its high bulk carbon concentration and susceptibility to SCC initiation in the as-received mill-annealed (MA) condition. This high bulk carbon level enabled the microstructure to be effectively modified by heat treatment. The basic information and bulk composition of this heat are listed in Table 2.

Table 2. Bulk compositions (wt%, unless specified otherwise) and initial condition of Alloy 600 material investigated in this study.

Material and Heat No.	Source and Description	Composition	Heat Treatments
Alloy 600MA NX6106XK-11	Special Metals 2-inch thick plate	Ni-16.4Cr-8.5Fe-0.06C-0.23Mn-0.22Si-0.22Al-0.30Ti-0.01Cu-0.001S-0.004P-83 appm B*	927°C for 3.5 hr + WQ

*The B content is measured by glow discharge mass spectrometry (GDMS).

To evaluate the effect of material condition and GB carbides on SCC, the as-received material was first heat treated at 1100°C for 30 minutes and water quenched (WQ) to dissolve pre-existing carbide precipitates. This SA material was then given a TT anneal at 704°C for 12 hours followed by air cooling to produce a semi-continuous distribution of GB carbides. The MA, SA, and SA+TT materials for SCC initiation testing were all cold forged (CF) to a 15% reduction in thickness and the specimens were all evaluated along the S-L orientation. SEM examinations were performed prior to the tests to document microstructures of these material conditions with details presented below.

Microstructure of Mill-Annealed (As-Received) Condition

The plate heat NX6106XK-11 was received in the form of a 5.08 mm (2 in) thick plate and in the MA condition reported as 927°C for 3.5 hours followed by a water quench. As reported earlier [20], this material features an average grain size of 65 μm with transgranular (TG) carbides on ghost grain boundaries and a non-uniform distribution of IG carbides (Figure 14). At lower magnifications, carbide banding were also observed in the material as shown in Figure 15. In addition, optical examinations on the etched cross-sections of this material revealed bands of larger and smaller grains along the processing direction (Figure 16). Some of the large "balloon" grains were highly elongated exceeding 1 mm in length.

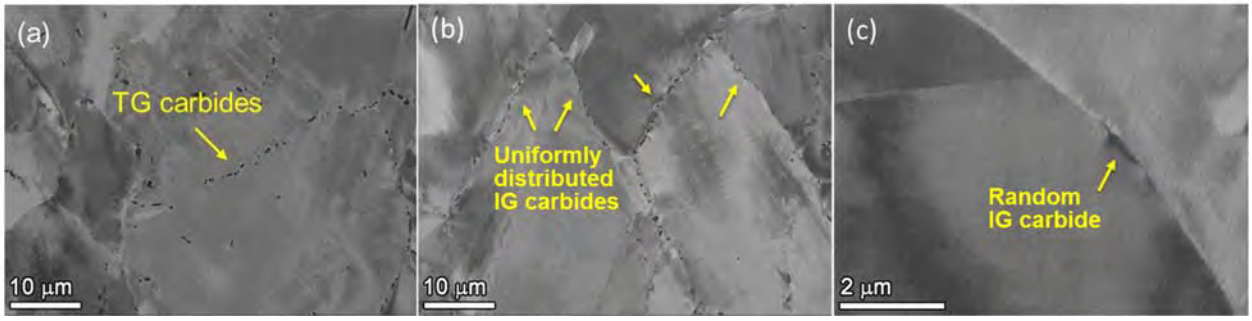

Figure 14. SEM-BSE images of carbide distribution in the Alloy 600MA heat NX6106XK-11 material: (a) most grains show primarily TG carbides, (b) few grains show higher density of IG carbides, and (c) more typical grain boundaries exhibiting low density of IG carbides.

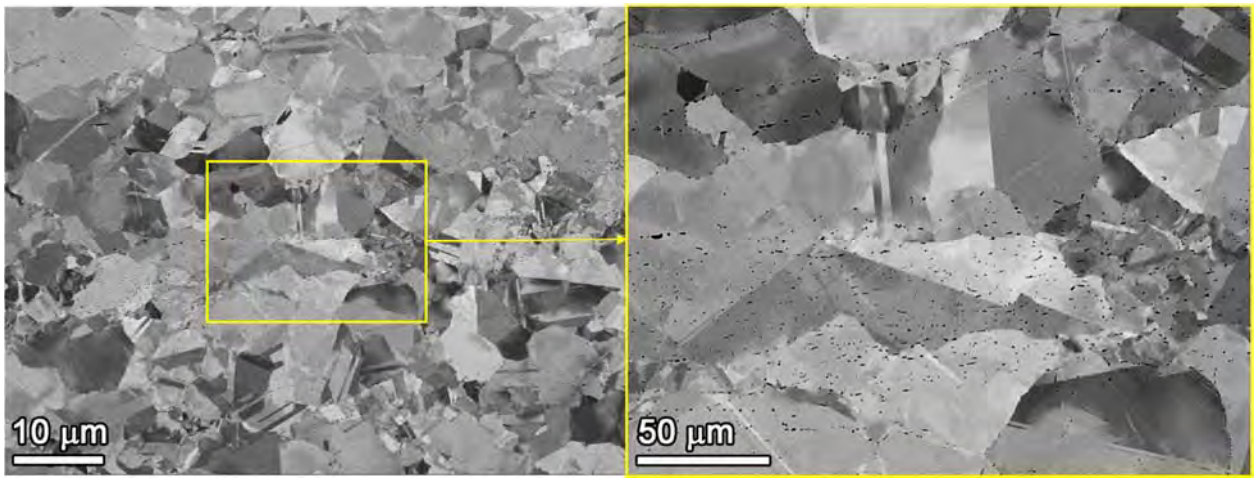

Figure 15. SEM-BSE images of carbide distribution in the as-received Alloy 600MA heat NX6106XK-11 material.

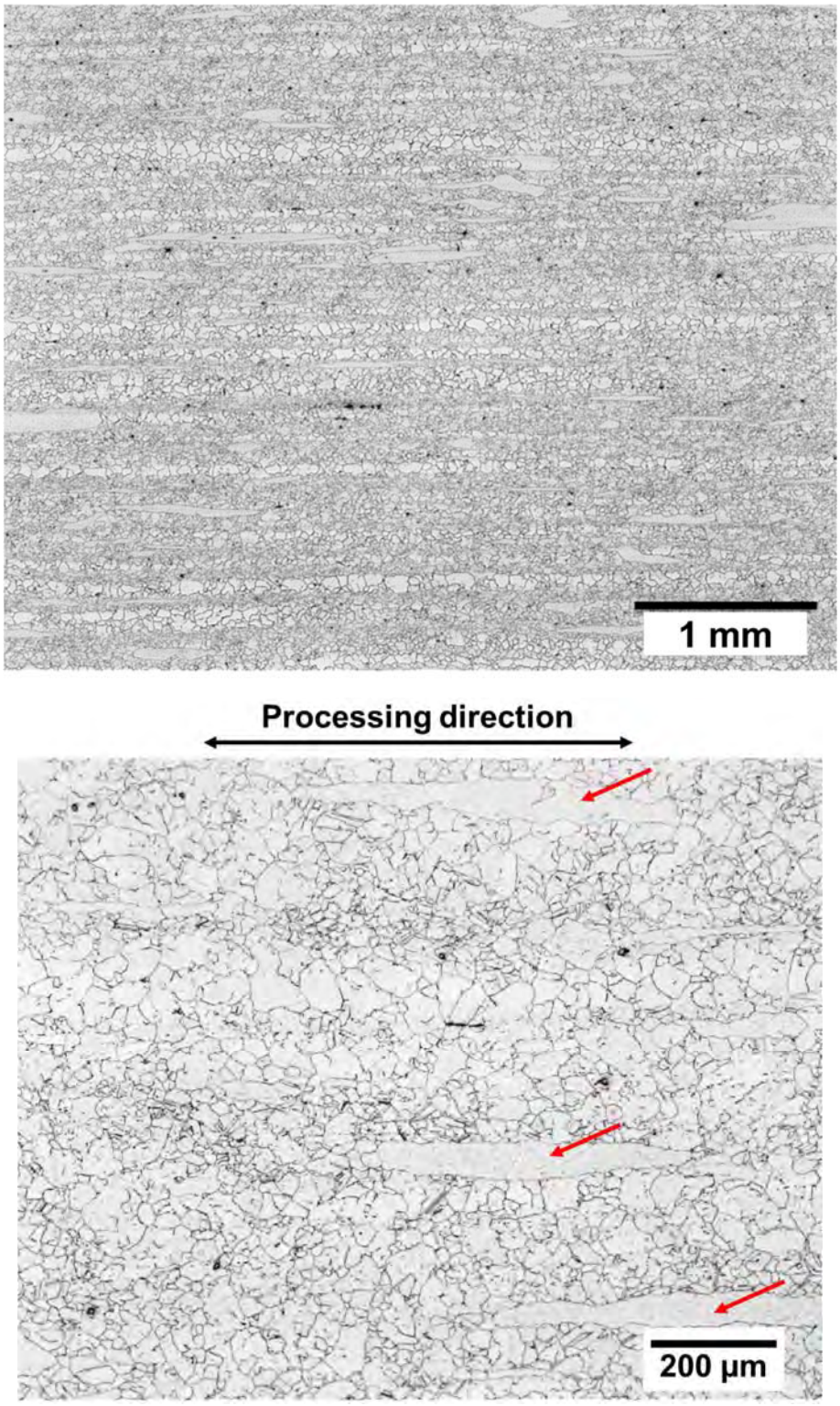

Figure 16. Optical image of the etched Alloy 600MA heat NX6106XK-11 material showing the inhomogeneous microstructure with large elongated grains highlighted by arrows.

Limited APT characterizations were performed on heat NX6106XK-11 in the MA condition in support of the SCC initiation testing in this material condition. These characterizations were performed to give some indication of how this heat's relatively high concentrations of B and C influenced GB segregation and precipitate compositions. APT elemental maps and concentration profiles corresponding to an IG Cr carbide/metal interface are presented in Figures 17 and 18. The atom map gives a visual sense of the elemental partitioning between the carbide the alloy matrix in addition to segregation of B and P to the carbide/metal interface. The carbide is typical for Alloy 600 with strong enrichment of Cr, C and B relative to the matrix. The concentration profile indicates the B concentration within the carbide is ~1 at.% and peaks at ~6 at.% at the carbide/metal interface. The interface is also enriched in P (~0.1 at.%), Si (1.2 at.%), Ti (0.9 at.%) and Nb (~0.2 at.%). The metal adjacent to the carbide is depleted of Cr (~5.5 at.%) and enriched in Fe (up to 12 at.%) as a result of the carbide precipitation during the MA treatment. What is most significant here is that despite the relatively high B concentration of heat NX6106XK-11 (83 appm by GDMS), the observed IG precipitate is a Cr carbide that also captures a significant amount of B. Strong interfacial segregation of B could eventually lead to Ni-boride precipitation, but to date such precipitates has not been identified in the characterizations of this heat in either the MA or the SA+TT condition.

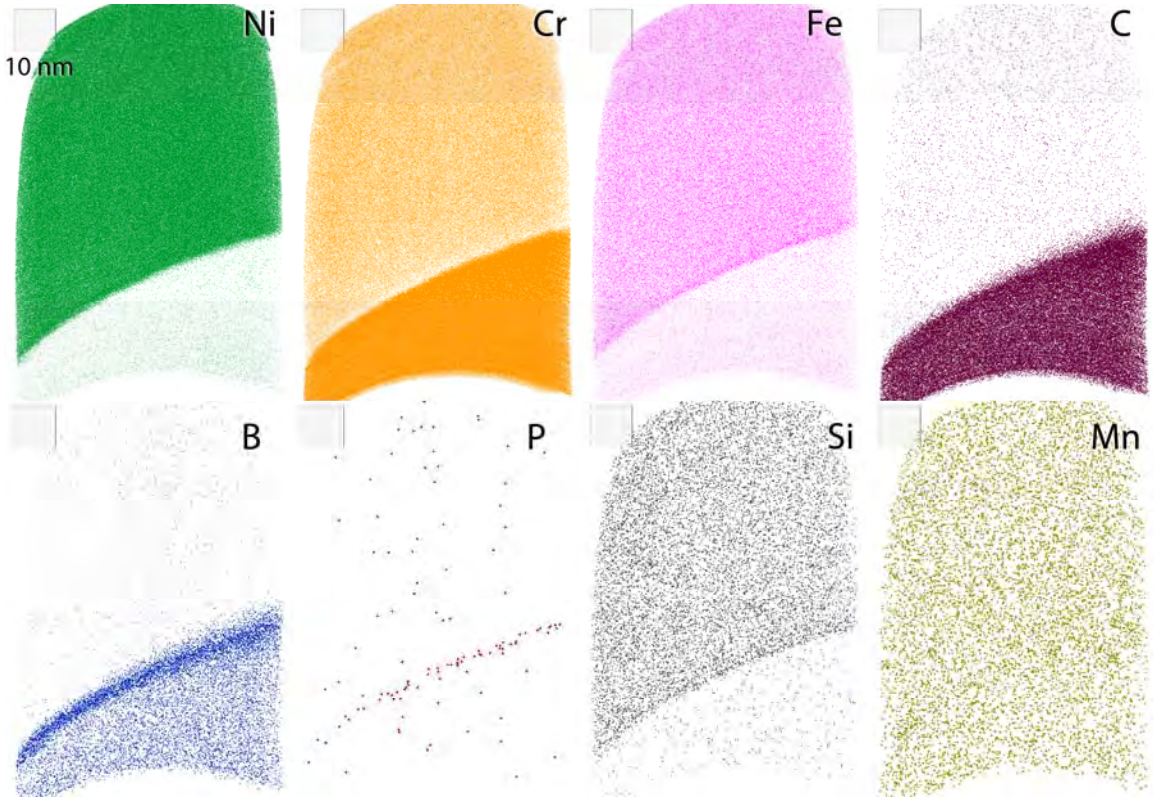

Figure 17. APT elemental atom maps (20 nm image depth) at the interface between an IG Cr carbide and the surrounding alloy matrix for heat NX6106XK-11 MA. Interfacial segregation is readily apparent for B and P and B also exhibits strong partitioning to the carbide phase.

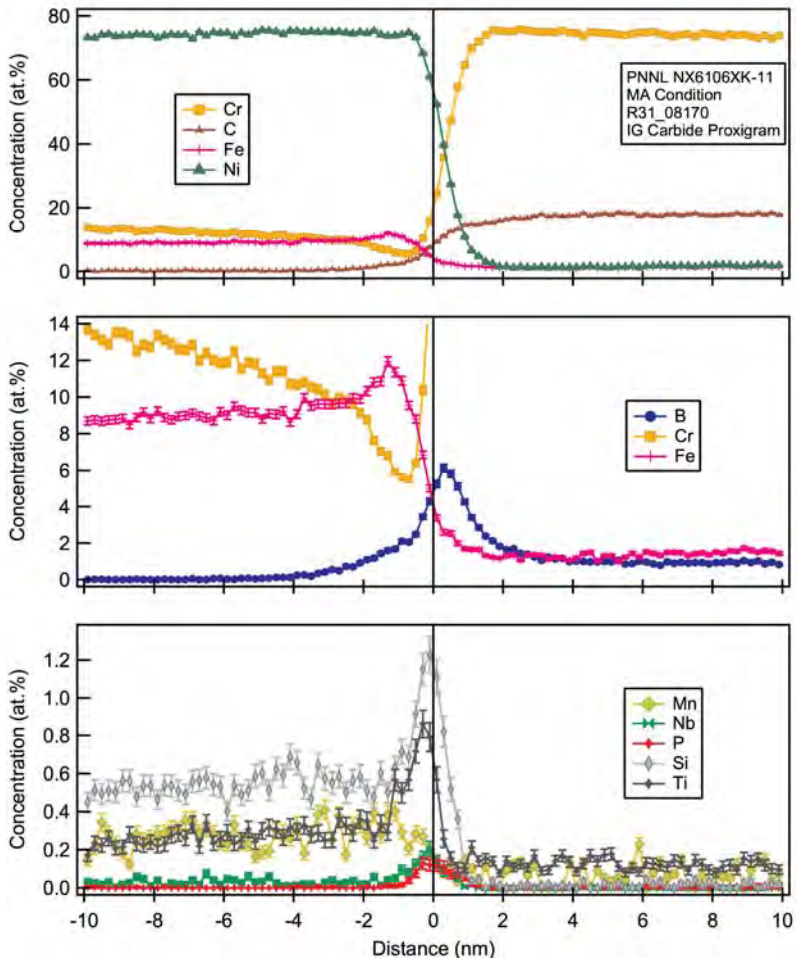

Figure 18. APT proximity histogram across an IG carbide/metal interface for heat NX6106XK-11 in the MA condition. Significant interfacial segregation is found for B, Si, Ti, P and Nb in addition to Cr depletion and Fe enrichment in the adjacent metal matrix.

Microstructure of Solution-Annealed Condition

The general microstructure after solution annealing and cold forging of the Alloy 600 heat NX6106XK-11 material is presented in Figure 19. An increase in grain size to 100-300 µm was observed after the solution annealing. Even though not all carbides in the matrix was dissolved, this heat treatment effectively removed most of carbides from high-energy GBs as shown in Figure 20, resulting in a very low GB carbide coverage.

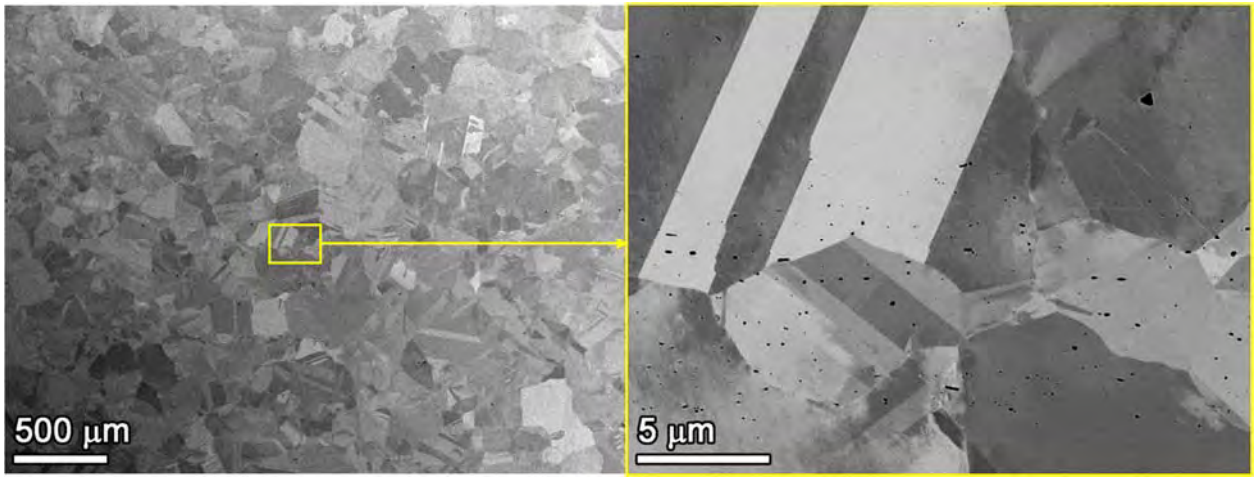

Figure 19. SEM-BSE images of grain size and carbide distribution in the Alloy 600 heat NX6106XK-11 material after solution annealing and cold forging.

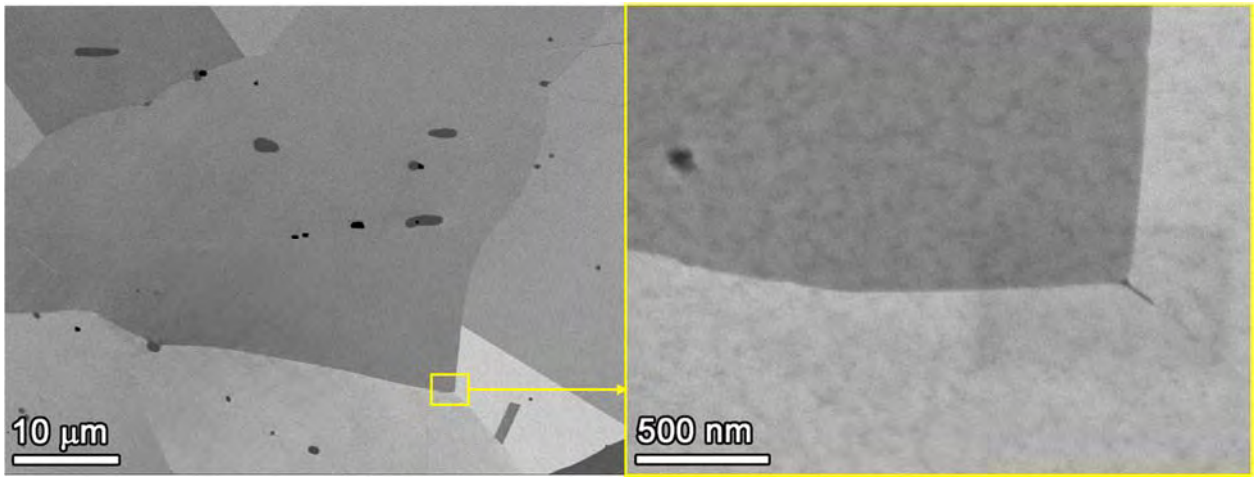

Figure 20. Representative SEM-BSE images of the GB in the 15%CF Alloy 600SA heat NX6106XK-11 material prior to testing.

Microstructure of Thermally-Treated Condition

Similar to the SA material, the SA+TT Alloy 600 heat NX6106XK-11 material exhibit a grain size varying from 100-300 µm. A semi-continuous distribution of carbides was observed at high-energy GBs in this material (Figure 21). The carbides produced by the thermal treatment were mostly ellipsoidal in shape and 100s of nm in size. In addition, a high density of transgranular (TG) precipitates were found along with the IG precipitates. These were usually

rod-shaped and crystallographically aligned with the alloy matrix. No significant crystallographic faceting was observed, suggesting the precipitates do not exhibit strong alignment with the fcc alloy matrix. Detailed SEM examinations of polished surfaces were performed to assess the GB carbide coverages. The SA+TT material was estimated to have a linear carbide coverage of ~52%, while the SA material exhibited very few GB carbides. It is also noteworthy that cold forging produced some permanent GB damage in the TT+15%CF specimen, including occasional small cavities at carbide-matrix interfaces and cracked carbides.

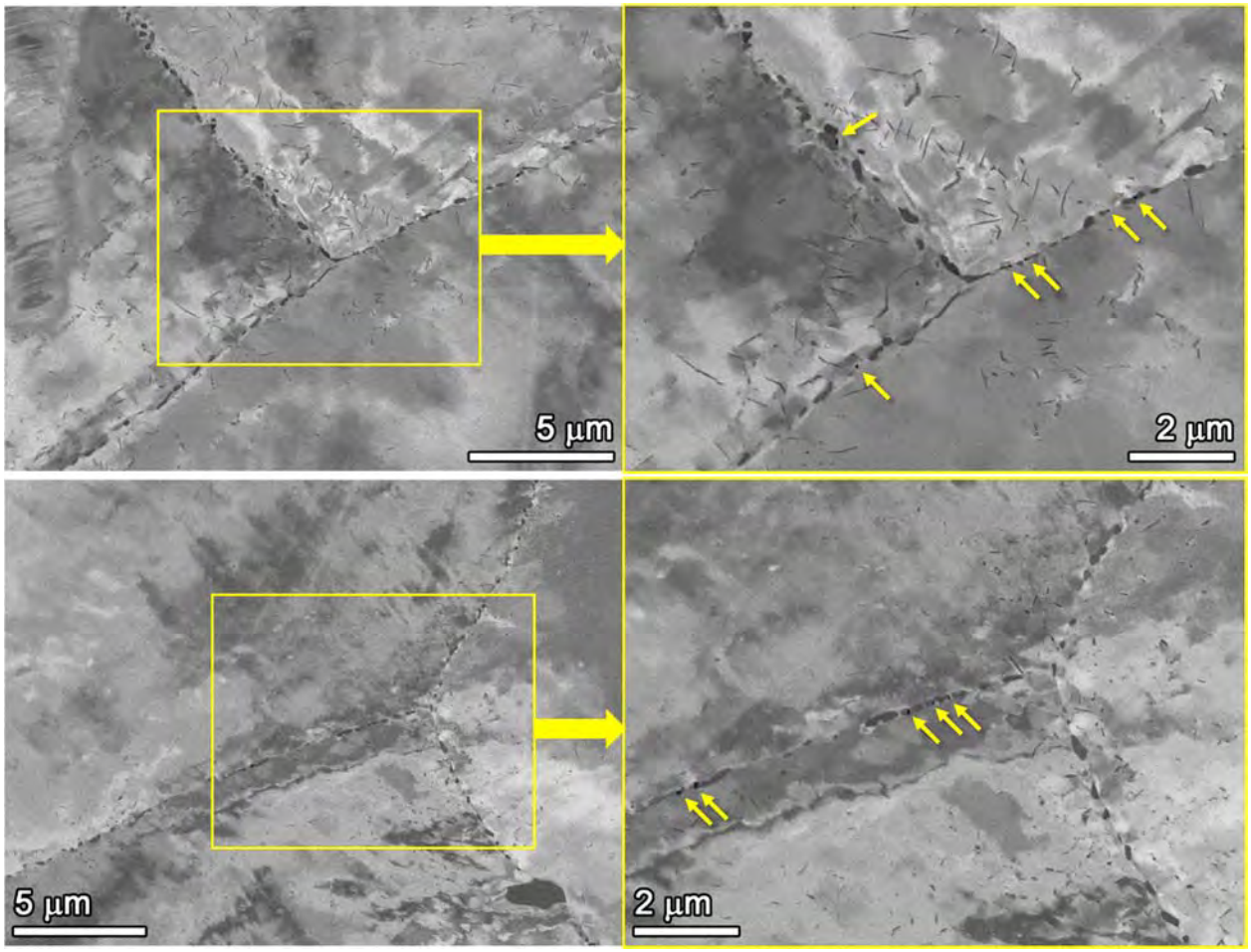

Figure 21. Representative SEM-BSE images of the GB carbides coverage of the 15%CF Alloy 600TT heat NX6106XK-11 material prior to testing. Arrowed features are cavities at carbide-matrix interface or cracks inside carbides produced by cold forging.

Precursor Damage Characteristics and Evolution

SEM examinations revealed that nearly all high-energy GBs exhibited some degree of precursor damage soon after the start of the test in all material conditions in both the unstressed exposure coupons and SCC initiation specimens. In this section, the typical morphology of precursor damage acquired using SEM will be shown for each material condition. Analytical high-resolution TEM examinations of IGA in unstressed exposure coupons will also be presented for the SA+ and SA+TT conditions. These provide a snapshot of the resultant behaviors at the

nanoscale and complement the synopsis of the IGA response summarized by the more comprehensive microscale SEM measurements. The quantitative analysis on the depth evolution of precursor damage will be summarized for all three material conditions, providing insights on differences among materials and GB damage evolution.

Precursor Damage in Heat NX6106XK-11 MA Condition

The representative morphology of IGA in the MA+15%CF unstressed exposure coupon after 1000 hours of exposure in 360°C simulated PWR primary water is shown in Figure 22. Since the MA condition features GBs both with and without carbides, one example of IGA on each type of high-energy GB is shown. Both examples show IGA of a depth of ~500 nm with corrosion extending ~100-200 nm into the grain at each side and a darker contrast at the center along the original GB. In particular, the IGA shown in Figure 22b terminates at an IG carbide, where the contrast at GB became darker and wider indicative of porosity. In addition, the carbide at the leading IGA front appears to have lost its integrity. This is reflected by the irregular hollow with rough edges where IGA is protruding into, which is unique to the carbides that are in contact with IGA.

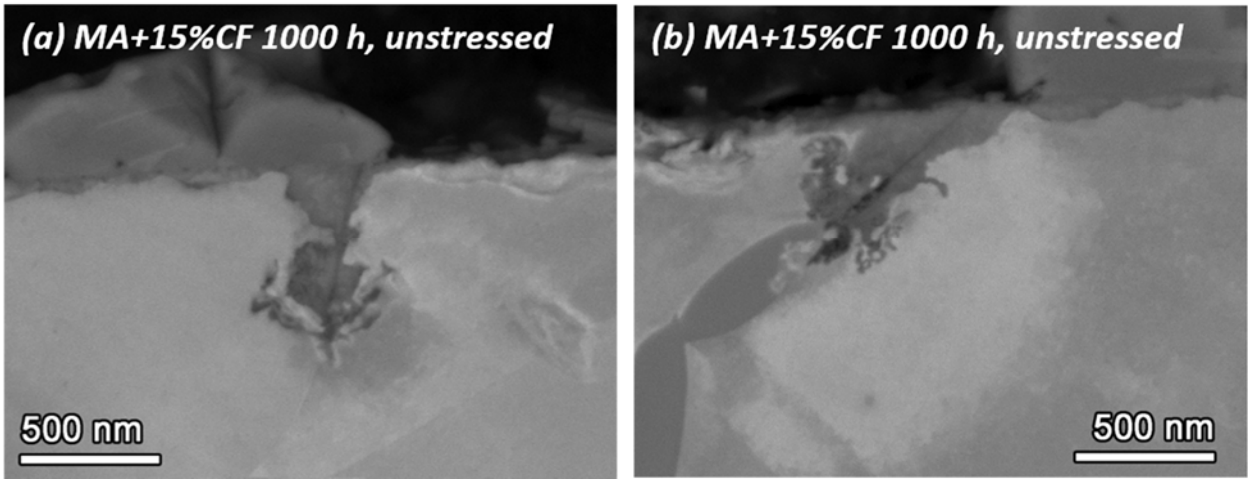

Figure 22. SEM-BSE images of representative IGA in the 15%CF Alloy 600MA heat NX6106XK-11 unstressed coupon after 1000 hours of exposure in 360°C simulated PWR primary water.

Typical morphology of precursor damage in the MA+15%CF SCC initiation specimens removed after 260 hours (a and b) and 456 hours (c-f) of exposure in 360°C simulated PWR primary water is shown in Figure 23. Detection of SCC initiation by DCPD occurred early for all the tested MA+15%CF specimens, therefore no specimen reached the same 1000 hours of exposure time as the unstressed exposure coupons at their first test interruption. In this figure, the precursor damage is also shown for high-energy GBs both with and without carbides for IN292 at 260 hours of exposure (Figure 23a and b) and IN146 at 456 hours (Figure 23e and f).

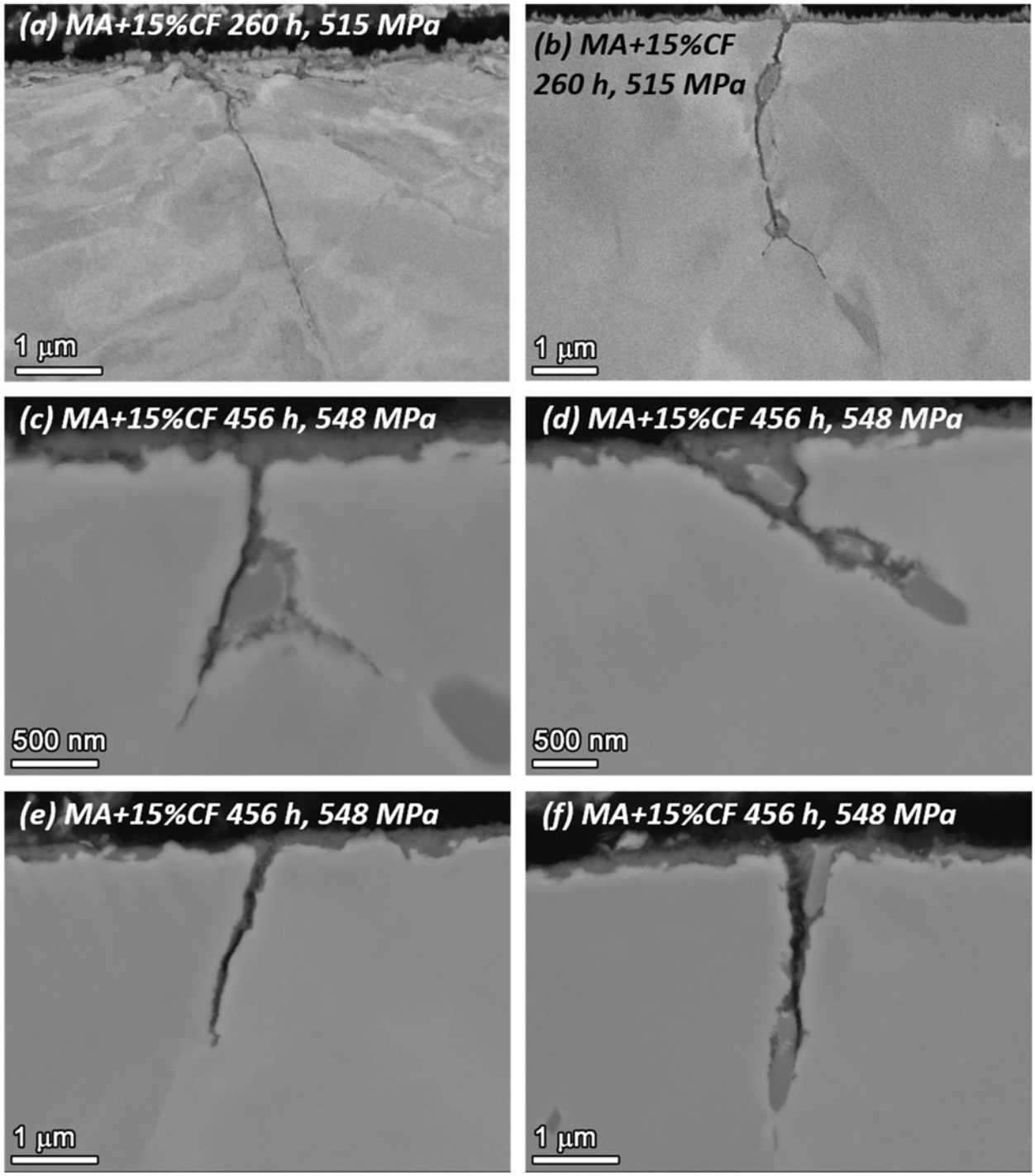

Figure 23. SEM-BSE images of representative IGA in the 15%CF Alloy 600MA heat NX6106XK-11 SCC initiation specimens IN292 after 260 hours of exposure (a, b) and IN146 after 456 hours of exposure (c-f) in 360°C simulated PWR primary water.

More cracks have started to form in IN146 as shown in Figure 23c, e and f. It is interesting to note that the existence of GB carbide does not seem to have affected the depth of IGA or the likelihood of cracking. In addition, examples of IGA in presence of GB carbides is shown in

Figure 23c and d for the SCC initiation specimen. They exhibit similar morphology as the carbides exhibiting irregular shapes in the unstressed exposure coupon, usually featuring a hollow where they first meet IGA. A similar feature will be analyzed by TEM in more detail in the TT condition, which will be presented later.

Precursor Damage in Heat NX6106XK-11 SA Condition

SEM Examination of SA+15%CF unstressed and stressed specimens

Representative examples of precursor damage in both the unstressed exposure coupons and constant load SCC initiation specimens in the SA+15%CF condition are shown in Figure 24. Compared to the IGA observed in the unstressed coupon (Figure 24a-b), the stress-assisted IGA in the initiation specimens appear to be more tightly confined along GBs (Figure 24c-f). Narrower brightly contrasted areas observed along the oxide indicate a lower degree of Ni enrichment/Cr depletion in the adjacent metal matrix in the initiation specimens. Instead, a portion of the stress-assisted IGA shows a darker contrast at the oxide/metal interface intersecting the surface due to crack formation. As shown in Figure 24e-f, a darker contrast streak emanated from the surface, extended down along the oxide/metal interface, and ended in lighter colored oxides. The cracked portion in most of the IGAs observed after 1004 hours of SCC test exposure exhibited a depth of 1-2 μm. Meanwhile, oxides that fully opened were also found in the SA+15%CF specimens after this test time. As shown in Figure 25a-b, some of these open cracks were only ~1 μm deep, which are shorter than the cracked IGAs shown in Figure 24e-f. It also is worth noting that the depths of some uncracked IGAs were longer than the ones that are fully cracked (Figure 25c-d), indicating boundary-to-boundary variability in initiation susceptibility. To avoid confusion, the partially and fully cracked IGAs are denoted as short cracks hereafter.

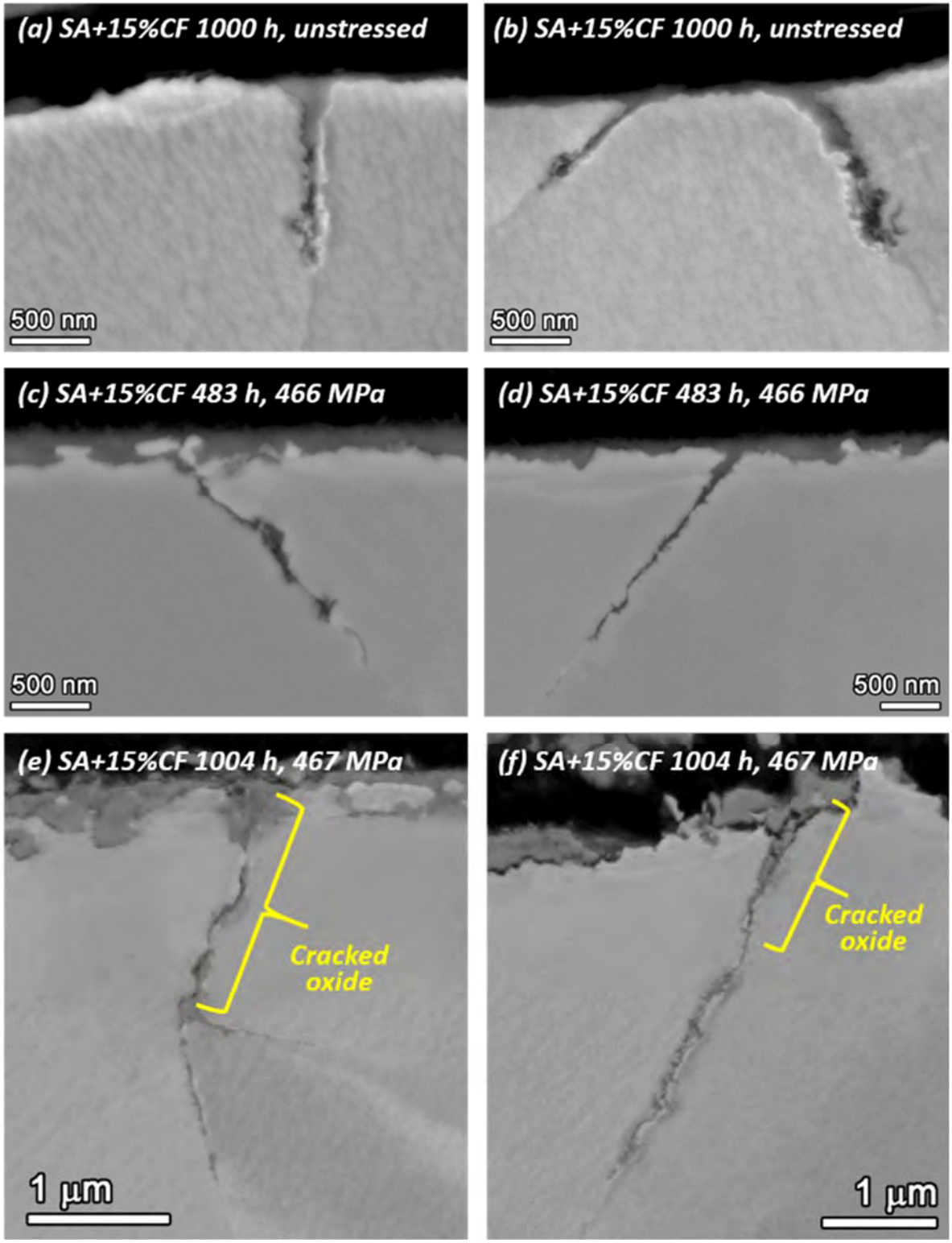

Figure 24. SEM-BSE images of representative IGA in the 15%CF Alloy 600SA heat NX6106XK-11 unstressed coupon after 1000 hours of exposure (a, b) and SCC initiation specimen IN282 after 483 hours of exposure at yield stress (c, d), and cracked IGA in IN284 after 1004 hours of exposure at yield stress (e, f) in 360ºC simulated PWR primary water.

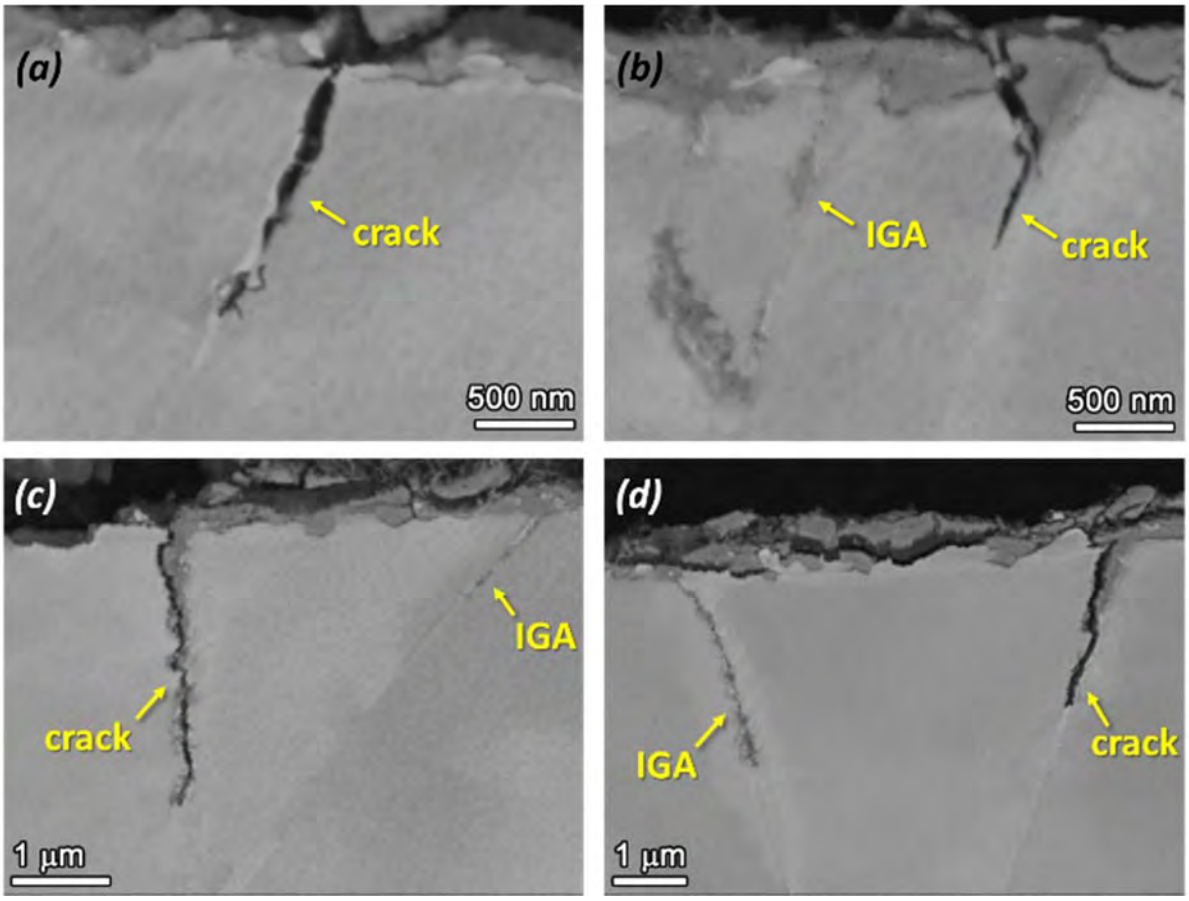

Figure 25. SEM-BSE images of IGA regions and short IG cracks observed in the 15%CF Alloy 600SA heat NX6106XK-11 SCC initiation specimen IN284 after 1004 hours of exposure at yield stress in 360°C simulated PWR primary water.

TEM Examination of non-CW SA unstressed specimen

Based on SEM examinations, the IGA in the non-CW Alloy 600SA NX6106XK-11 unstressed exposure coupon exhibited similar morphological characteristics as those observed in the SA+15%CF SCC initiation specimens. To better understand this localized corrosion/oxidation, TEM analysis was conducted on a representative IGA from an unstressed SA coupon after 1000 hours of exposure. Low magnification scanning (S)TEM annular dark-field (ADF) and bright field (BF) images of the IGA are shown in Figure 26. At 1000 hours, the IGA in this cross-section appears to be ~450 nm deep from the exposed, polished surface. The leading IGA (deepest 200–250 nm of length) is very tight to the boundary, only flaring out into the surrounding matrix near the leading tip, while the shallower IGA (< 200 nm from the exposed surface) exhibits a characteristic wedge shape that is wider at the surface and gradually narrows down to the grain boundary. Within the IGA is a central channel with muted contrast in ADF and brighter contrast in the BF image, suggesting the presence of a lower atomic number (Z) material along the centerline of the IGA. This zone aligns with the GB plane ahead of the leading IGA and is believed to be the location of the original boundary before exposure.

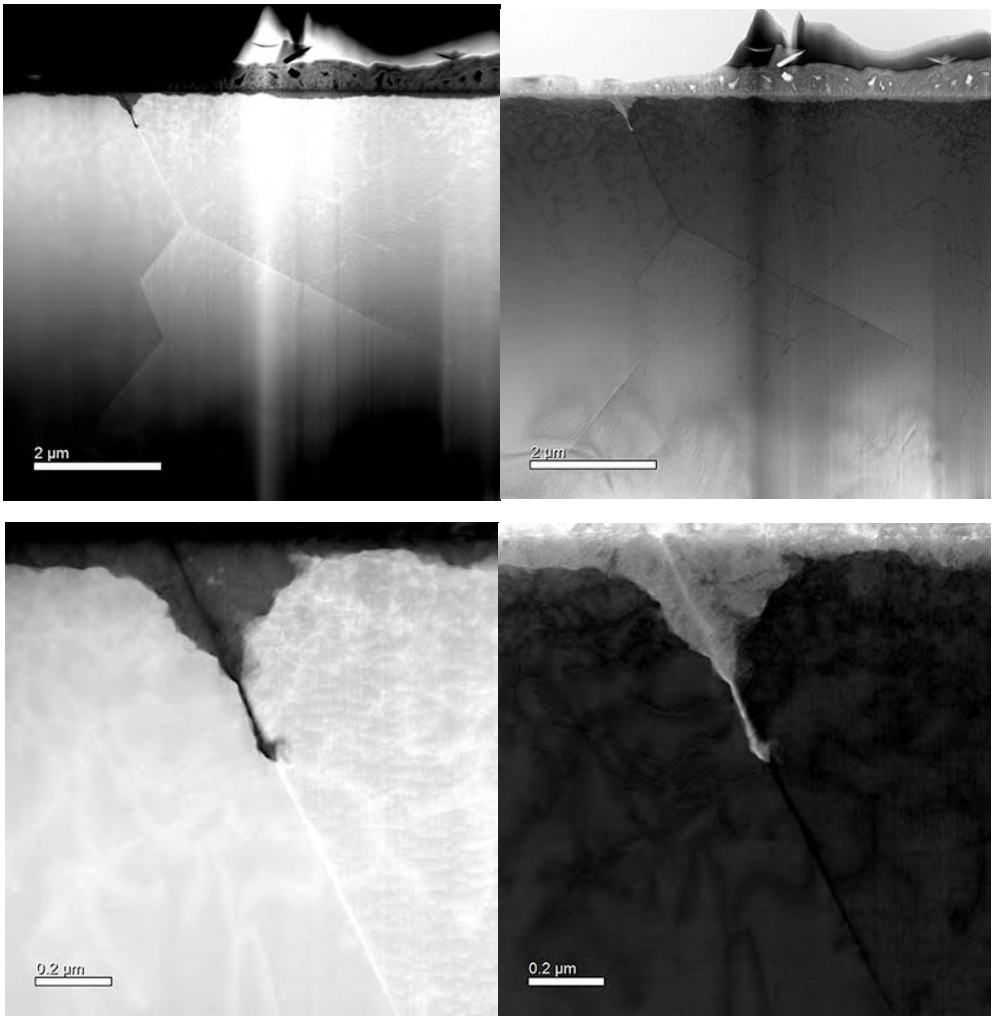

Figure 26. STEM (ADF/BF) low magnification images showing the surface microstructure of the non-CW Alloy 600SA heat NX6106XK-11 unstressed coupon after 1000 hours of exposure in 360°C simulated PWR primary water.

STEM EDS elemental mapping of the IGA is shown in Figure 27 and provides more insight into the composition variations between the various regions of the attack. Noticeably, there is minimal chemical signal along the thin, muted Z-contrast region in the center of the IGA. A strong Cr-rich oxide accents both sides of this dark stripe all the way to the leading IGA. The surface oxide is also Cr rich, but not as strongly as the center line of the IGA oxide. A thin (<5 nm) region of Cr depletion was also observed at the metal/oxide interface along the majority of the IGA. A weak S signal is also associated with the Cr-depleted oxide/metal interface. The Fe signal is depleted for much of the IGA near the original GB plane, while the oxide extending further into the matrix, especially near the surface, has a similar Fe signal as the surrounding alloy matrix. Lastly, the Ni signal appears highly depleted for both the IGA and TG oxides while the GB ahead of the oxidation front is Ni rich.

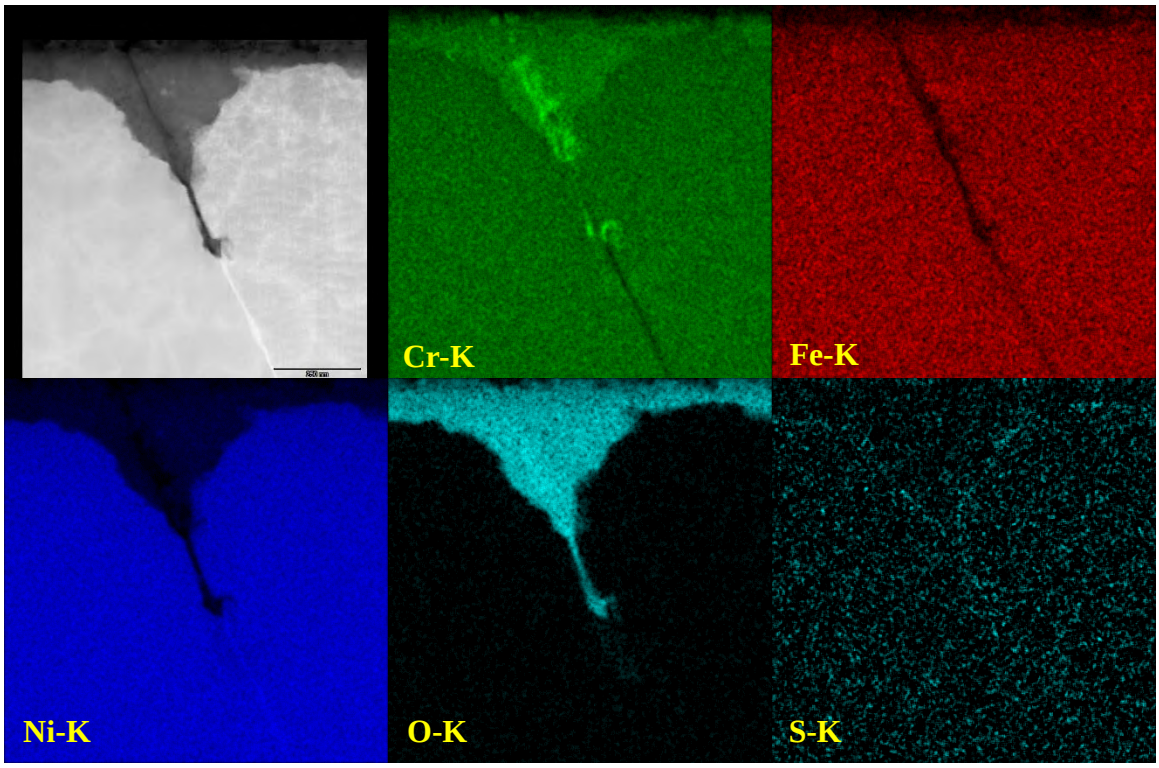

Figure 27. STEM (ADF) and EDS elemental maps showing the IGA in the non-CW Alloy 600SA heat NX6106XK-11 unstressed coupon after 1000 hours of exposure in 360°C simulated PWR primary water.

The GB ahead of the leading IGA was titled on edge and EDS elemental mapping was performed to understand the extent of composition changes and/or GB migration as a result of the IGA (Figures 28 and 29). Both Cr and Fe are depleted to ~700 nm ahead of the leading IGA, with Ni being enriched (Figure 28). The width of elemental depletion (~20 nm) indicates some GB migration has occurred during the corrosion experiment. Box sum scans taken at various distances ahead of the leading IGA (Figure 29) provide further quantification of the Cr and Fe depletion. Near the leading tip the Cr depletes from ~17 at.% to 12 at.% and Fe depleted from ~10 at.% to 6 at.% and Fe had an identical depletion profile as Cr. Deeper line scans (LS 2 and 3) show that Cr is depleted to greater depths than Fe, which is generally expected as Cr should exhibit higher GB diffusivity than Fe in a Ni-base alloy.

The 3D nature of the leading IGA and the GB ahead was studied by performing a tilt series normal to the boundary (Figures 30 and 31). The micrographs were taken at 5˚ tilt steps and corroborate the initial impression from EDS elemental maps in Figure 27 that at the IGA extends from the primary GB plane into the surrounding matrix at the leading tip. However through the tilt BF tilt series (Figure 30), it also becomes apparent that the GB ahead of the IGA twists into the plane of the page. This twisting is clearly coincident with the sudden jog of the oxidation from the primary GB plane, but the exact causality and interpretation are unclear.

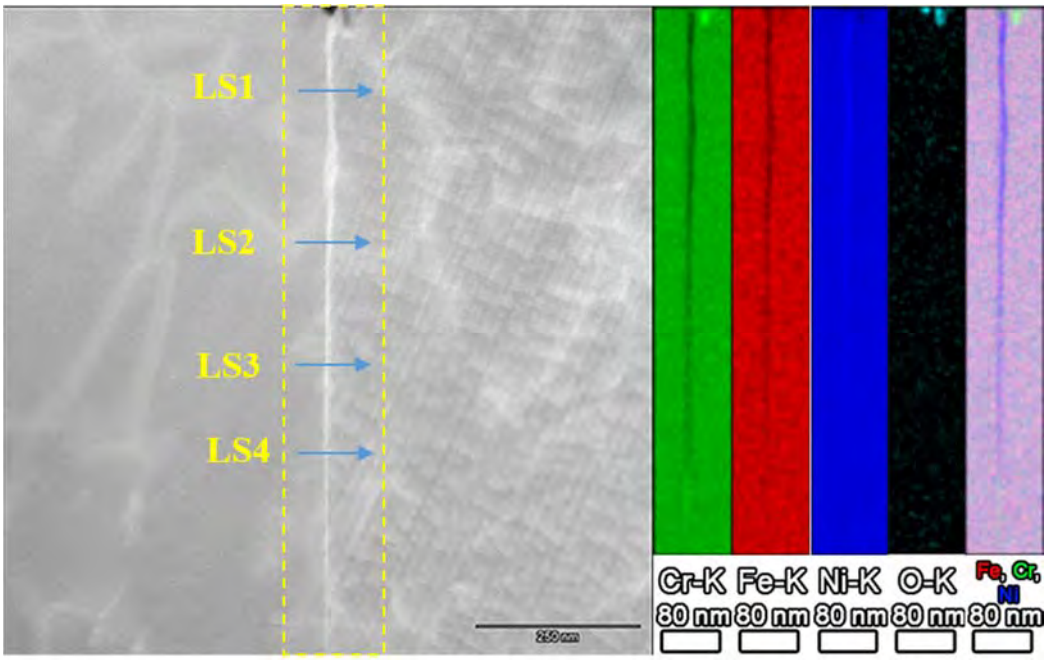

Figure 28. STEM (ADF) and EDS elemental maps of the grain boundary ahead of the leading IGA.

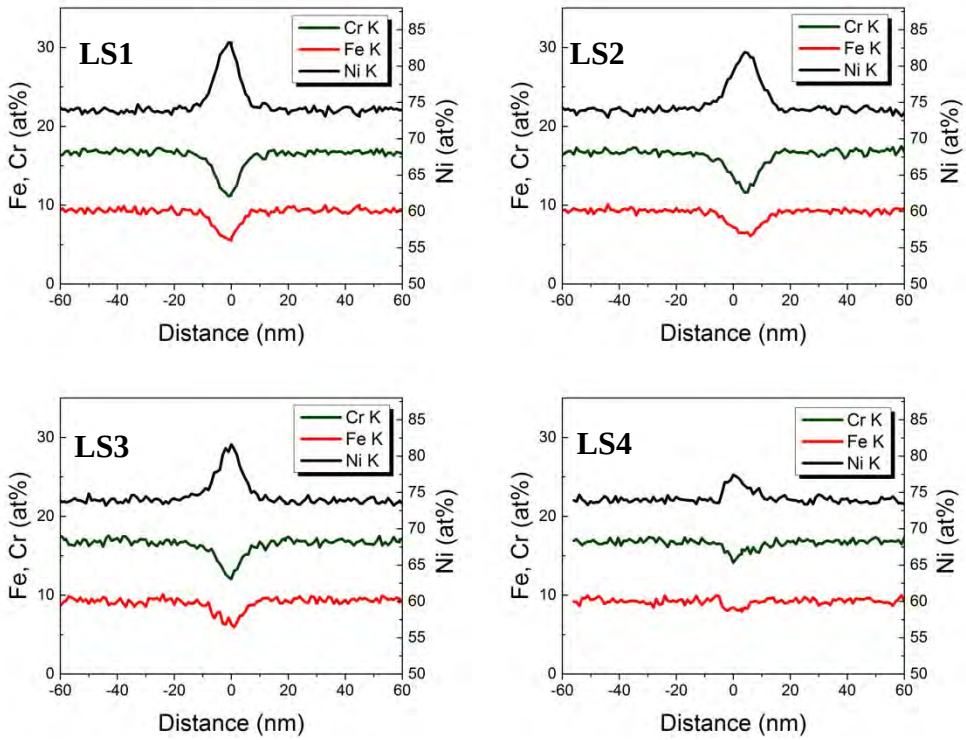

Figure 29. EDS compositional linescans (see annotations in Figure 28) of the metallic grain boundary ahead of the leading IGA.

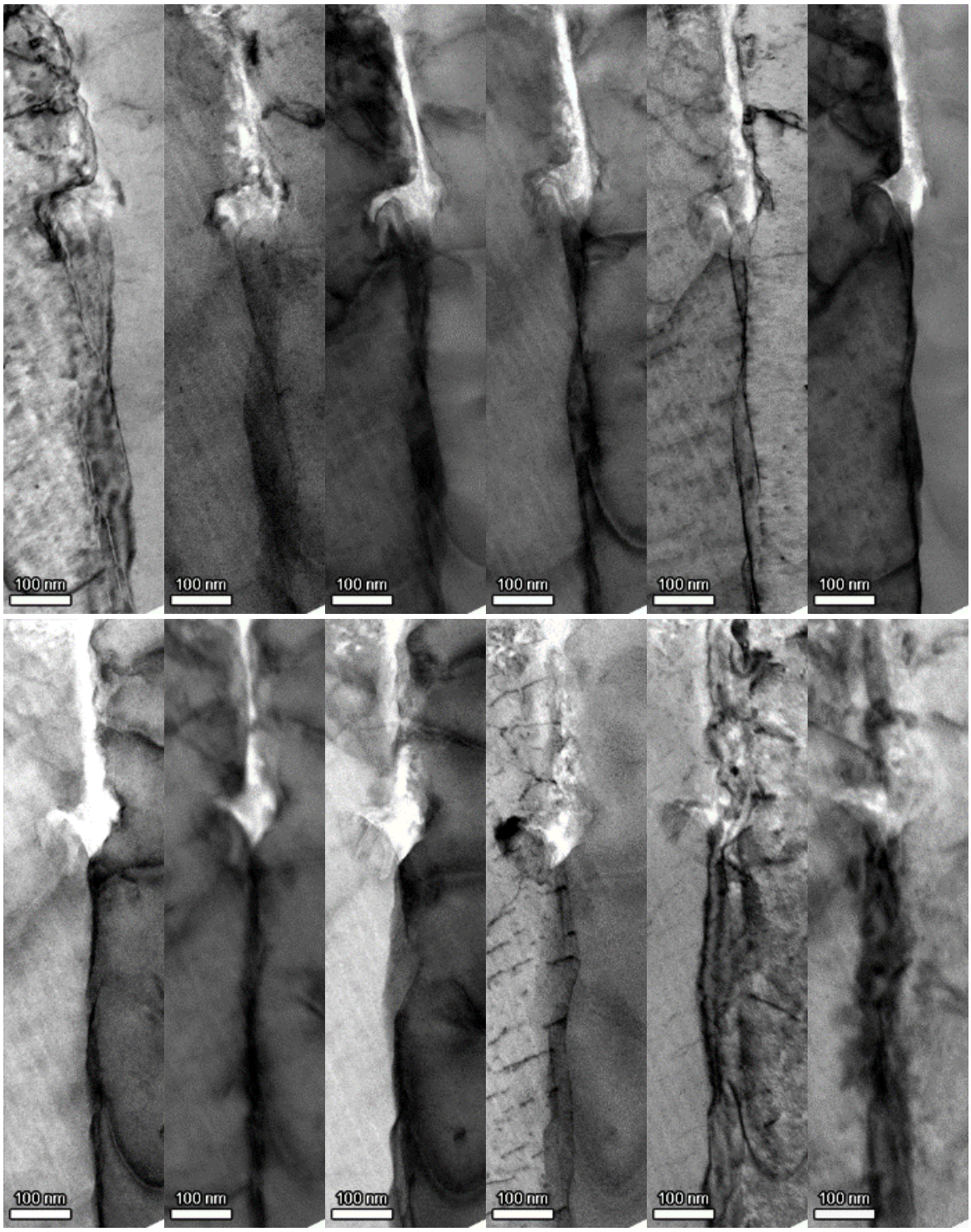

Figure 30. STEM(BF) tilt series (5˚ steps) across the leading IGA showing the 3D structure of both the terminal IG oxide and the metallic GB ahead.

Close inspection of the BF tilt series is that the oxidation is in fact still IG with the oxide chasing the abrupt twist of the GB plane near the oxide terminus. While the 3D nature of the APT data make clear that it is in fact still an IG oxide, a single TEM projection cannot provide similar

interpretation. This is overcome, to some extent, in the current example with the TEM tilt series that provide quasi-3D interpretation of these fine details. Mechanistically, it is unclear why the GB exhibits these abrupt jogs or twists near the terminal oxide or if has a potential role in the IGA or IGSCC behavior of the material.

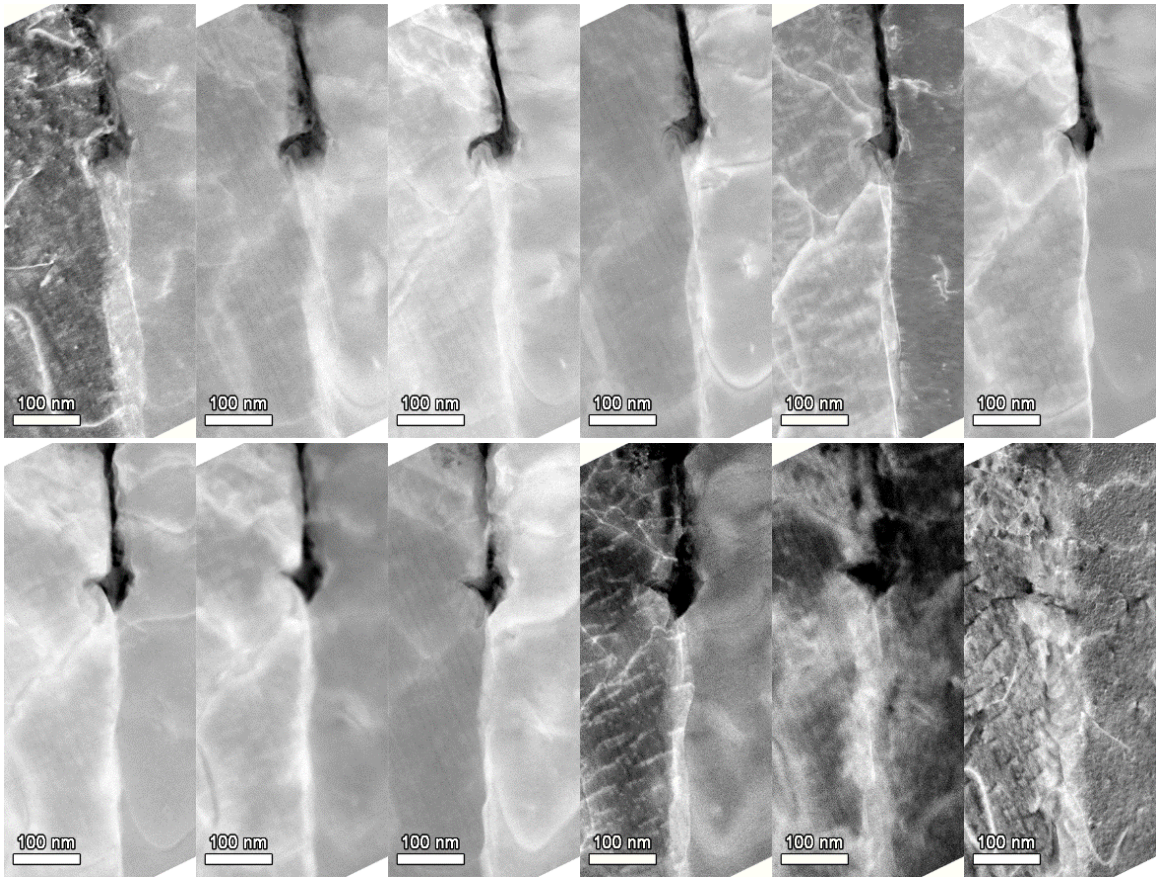

Figure 31. STEM(ADF) tilt series (5˚ steps) across the leading IGA showing the 3D structure of the terminal IG oxide and the metallic GB ahead of the oxidation front. Note the twisted nature of GB plane just ahead of the oxidation and how the oxide extending laterally from the primary GB plane appears to "chase" the twisted portion of the boundary at its terminus.

Precursor Damage in Heat NX6106XK-11 TT Condition

SEM Examination of TT+15%CF unstressed and stressed specimens

Figures 32 and 33 show typical morphologies of precursor damage in both unstressed exposure coupons and constant load SCC initiation specimens in the TT+15%CF condition. Unlike the SA materials, IGAs in the TT materials were deflected around the periphery of GB carbides, resulting in thicker IGAs in both the unstressed and stressed specimens (Figure 32a-d). The most significant difference between the unstressed and stressed specimens is that the precursor damage obviously went deeper after similar exposure times in the SCC initiation specimens, which will be documented in more detail later. In addition, IG cracks were found on some GBs in the SCC initiation specimens starting from 473 hours of exposure whereas no cracking was

observed in the unstressed coupon. As shown in Figure 33c and d, a few IG cracks went more than 7 μm deep in the TT+15%CF SCC initiation specimen after 1000 hours of exposure.

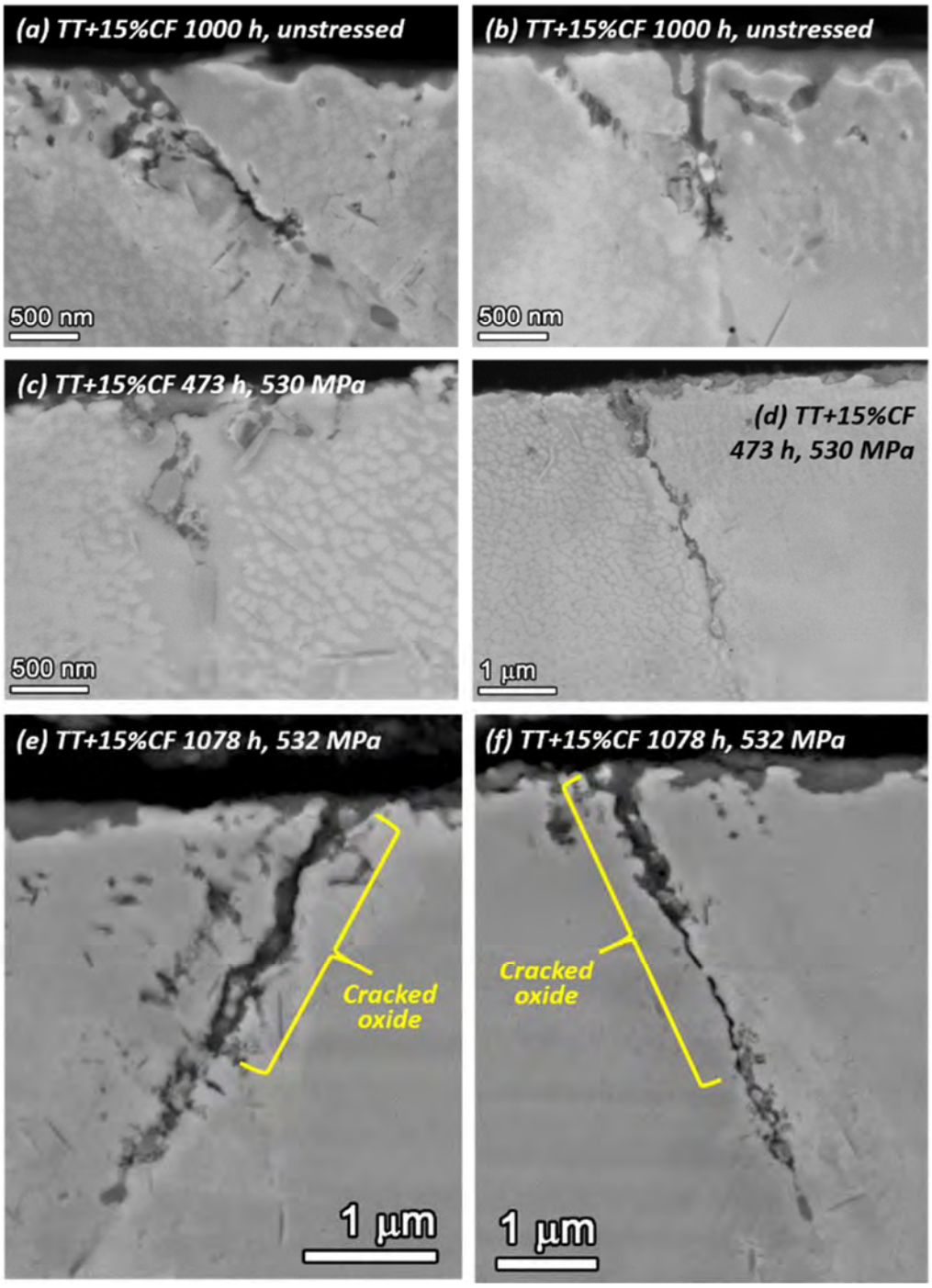

Figure 32. SEM-BSE images of representative IGAs in the 15%CF Alloy 600TT heat NX6106XK-11 exposure coupon after 1000 hours of exposure (a, b) and SCC initiation specimen IN278 after 473 hours of exposure at yield stress (c, d), and cracked IGAs in IN276 after 1078 hours of exposure at yield stress (e, f) in in 360°C simulated PWR primary water.

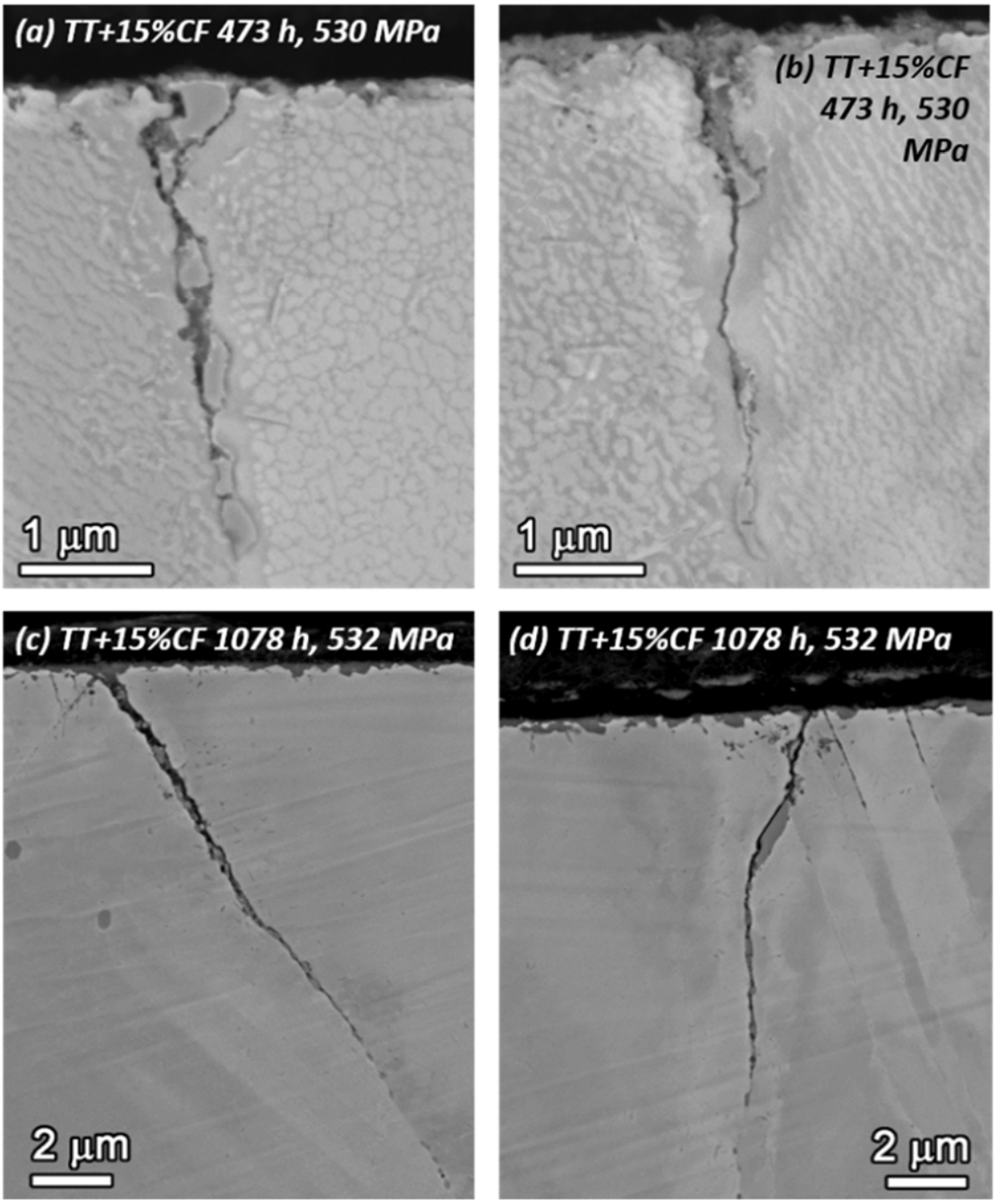

Figure 33. SEM-BSE images of representative short IG cracks observed in the 15%CF Alloy 600TT heat NX6106XK-11 SCC initiation specimen IN278 after 473 hours (a, b) and IN276 after 1078 hours (c, d) of exposure in 360°C simulated PWR primary water.

TEM Examination of non-CW TT unstressed exposure coupon

Figure 34 shows a STEM BF/ADF pair at low and medium magnifications of the IGA for a non-CW Alloy 600TT heat NX6106XK-11 unstressed coupon after the 4400 hours of exposure. The GB is decorated with a high density of precipitates in addition to the IGA. Large (200–500 nm)

spinels were observed at the surface directly above the IGA. A moderate density of TG precipitates were also observed adjacent to the grain boundary. In addition to the localized IGA, TG corrosion near the surface was also observed. The IGA itself extends approximately 1.5 µm in depth, terminating at an IG carbide. In general, the oxide microstructure is much more complex than that found for the SA material. The IGA near the intersection of the GB with the exposed surface exhibits the typical wedge-shaped penetration, narrows to a relatively thin attack for a few hundred nanometers, and then exhibits significant TG corrosion (~500 nm into the matrix on either side of the GB) closer to the IGA terminus.

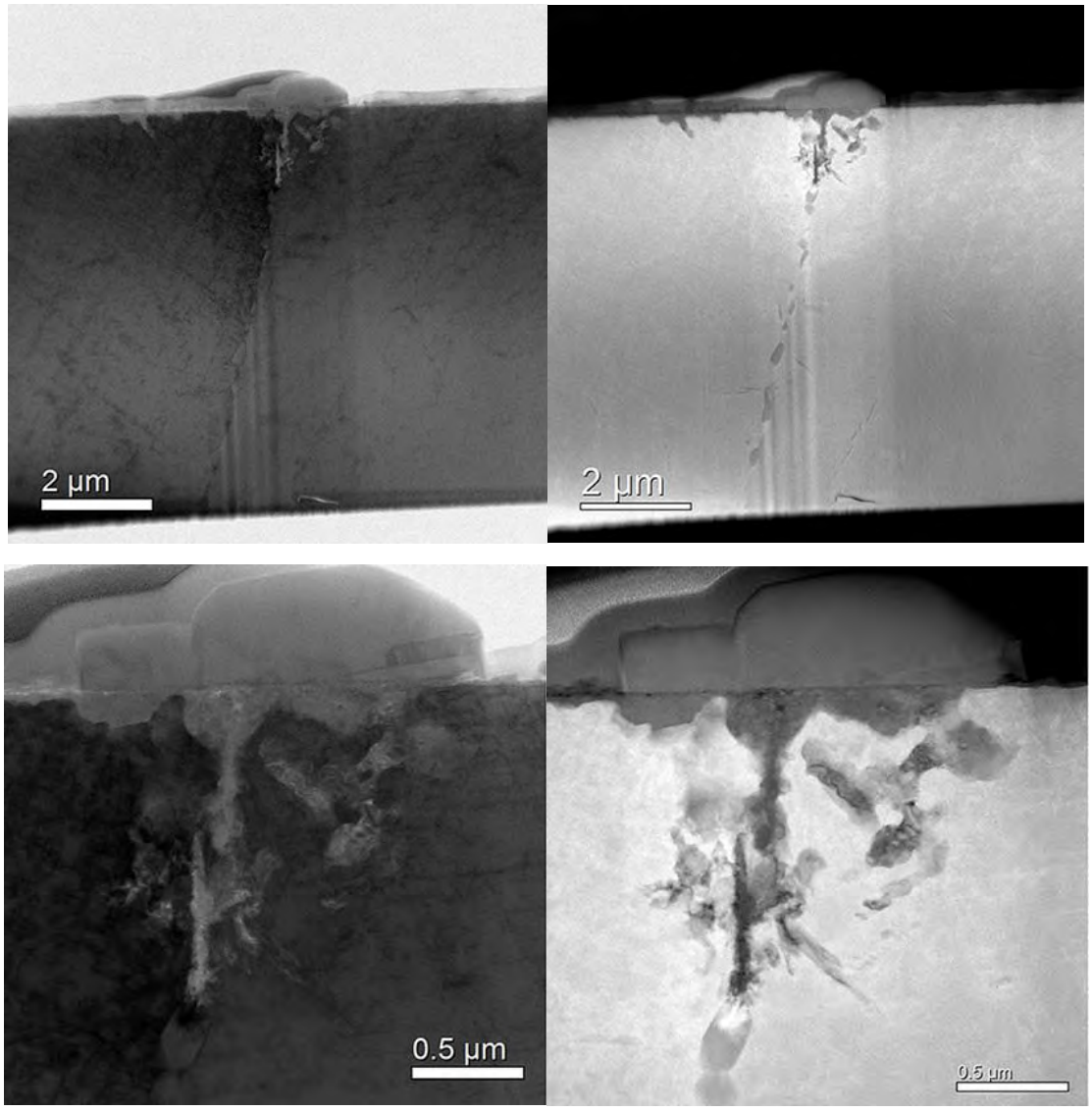

Figure 34. STEM (BF/ADF) low magnification images showing the representative surface attack for the non-CW Alloy 600SA heat NX6106XK-11 unstressed coupon after 4400 hours of exposure in 360ºC simulated PWR primary water.

A BF/ADF tilt series (10˚ steps orthogonally across the GB) was taken to provide insights into the 3D structure of the corroded material (Figures 35 and 36). In brief, the IGA microstructure defies a simple description. The oxide shows varying levels of contrast in both the BF and ADF image series indicating a multiphase oxide. Isolated, round regions of very dark contrast in the ADF series also suggest the presence of porosity within the oxide microstructure. The tilt series gives a general impression that all the observable oxides are interconnected with each other, suggesting internal oxidation is not a prominent degradation mechanism. The IGA also terminates at an IG carbide. The oxide at the terminus exhibits a darker contrast by ADF than the shallower oxides, indicating a lower density or Z number, likely in concordance with a higher Cr concentration. The carbide/oxide interface also exhibits bright contrast by ADF, indicating a higher local density in line with Ni enrichment.

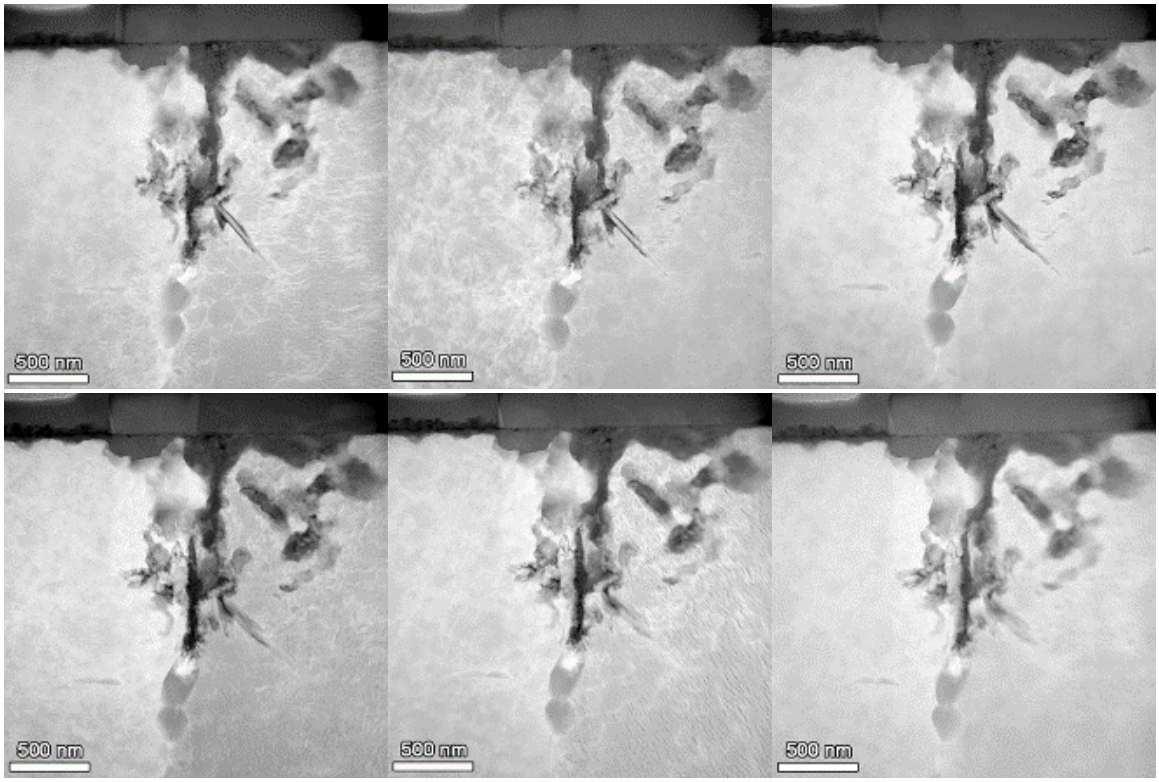

Figure 35. STEM(ADF) tilt series (10˚ steps) across a representative IGA feature in the non-CW Alloy 600SA heat NX6106XK-11 unstressed coupon after 4400 hours of exposure showing the 3D structure of the IGA and GB ahead.

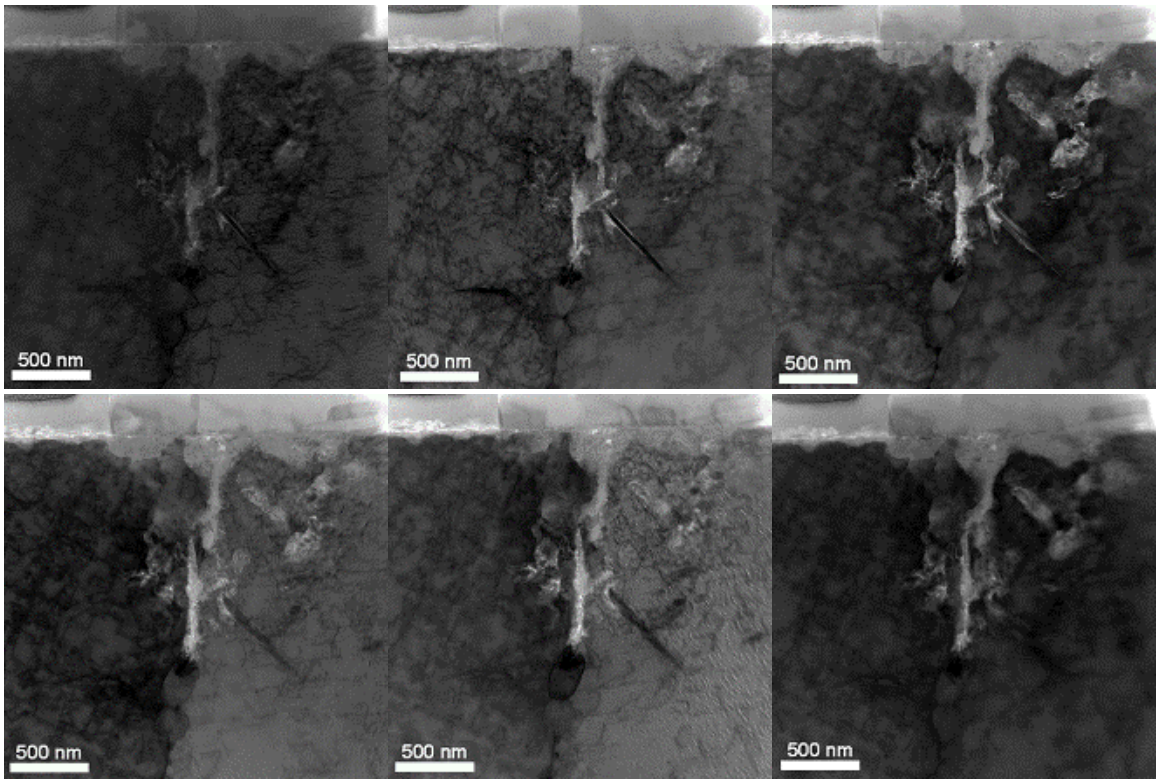

Figure 36. STEM(BF) tilt series (10˚ steps) across a representative IGA feature in the non-CW Alloy 600SA heat NX6106XK-11 unstressed coupon after 4400 hours of exposure showing the 3D structure of the IGA and GB ahead.

EDS elemental mapping of the IGA (Figures 37–39) reveal GB precipitates enriched in Cr and Ti. Subtle Fe enrichment is also apparent towards the flanks of the IGA. Depletion of Cr extends ~400 nm into each adjacent grain with line profiles (Figure 39) showing the gradual increase of Cr back to the alloy composition. This broad depletion profile likely originates from the original thermal treatment producing Cr carbide precipitation rather than the IGA process. The majority of the IGA consists of a Cr-rich oxide, with the noted Fe enrichment at its edges. Localized Ti enrichment in the IGA coincides with the size and morphology of the Ti-rich GB precipitates observed ahead of the oxidation front, suggesting the Ti-rich oxides form from the alteration of these secondary phases. Additionally, a faint S signal accents the metal/oxide interface along the majority of the IG and TG oxidation. Local oxidation adjacent to the IGA appears to have often occurred along the carbide interfaces (Figure 38).

The near-surface IGA exhibits the characteristic wedge-shaped ditch for most attacked GBs in this study. This oxide was observed to be mainly Cr and Fe rich with a composition similar to the more general TG oxide formed on the surface further away from the GB. Immediately ahead of the leading oxide signal (O-K map in Figure 38), a large Cr carbide (determined to be Cr_7C_3, Figure 40) has partially dissolved as a result of exposure to high temperature water and converted into a Ni-rich metallic phase, as shown by both EDS (Figure 38) and EELS (Figure

41) spectrum imaging. In this case, the carbide is being attacked primarily from one direction rather than from all directions around its periphery.

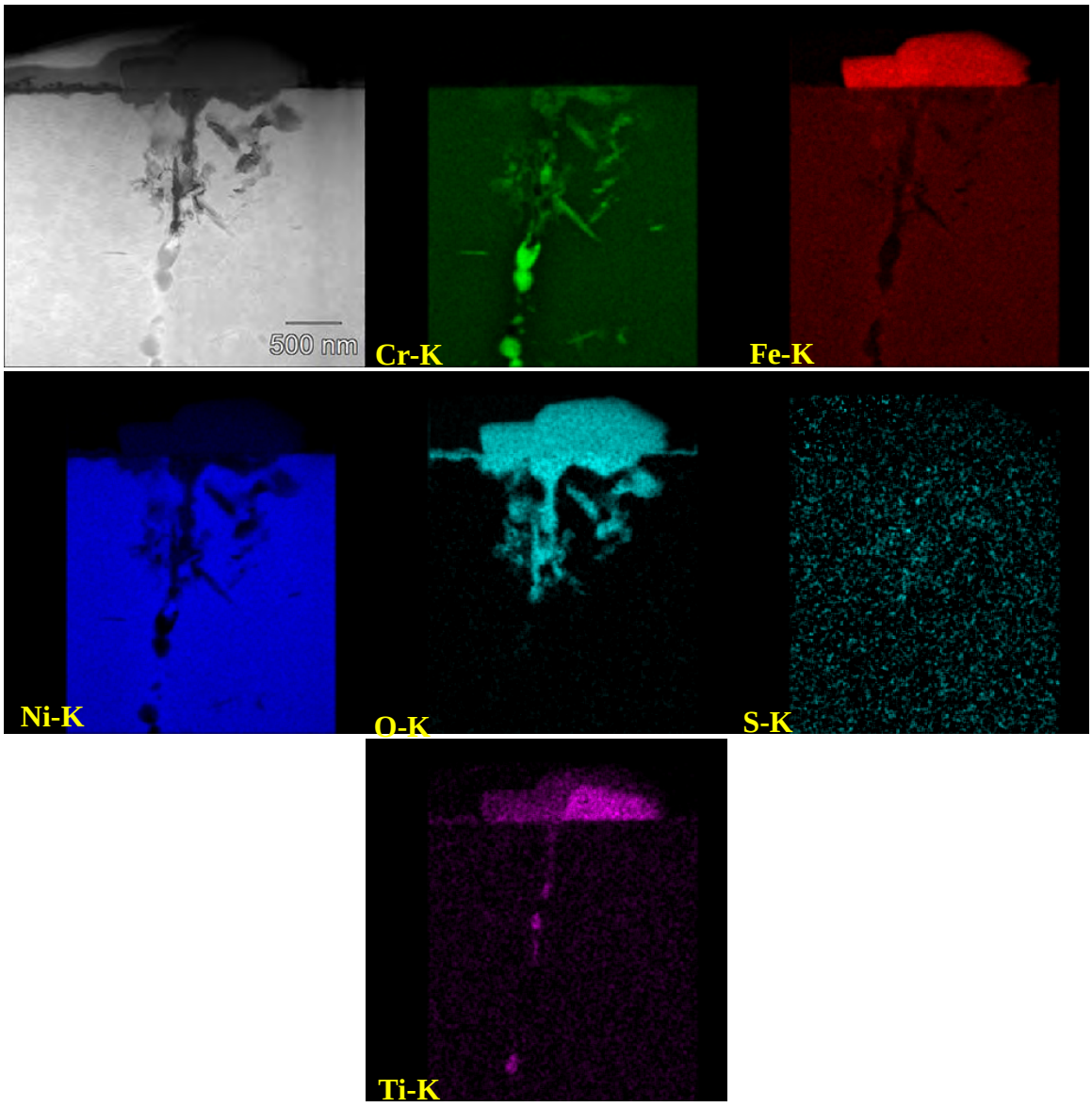

Figure 37. STEM(ADF) and EDS elemental maps showing a representative IGA feature in the non-CW Alloy 600SA heat NX6106XK-11 unstressed coupon after 4400 hours of exposure in simulated PWR primary water at 360°C.

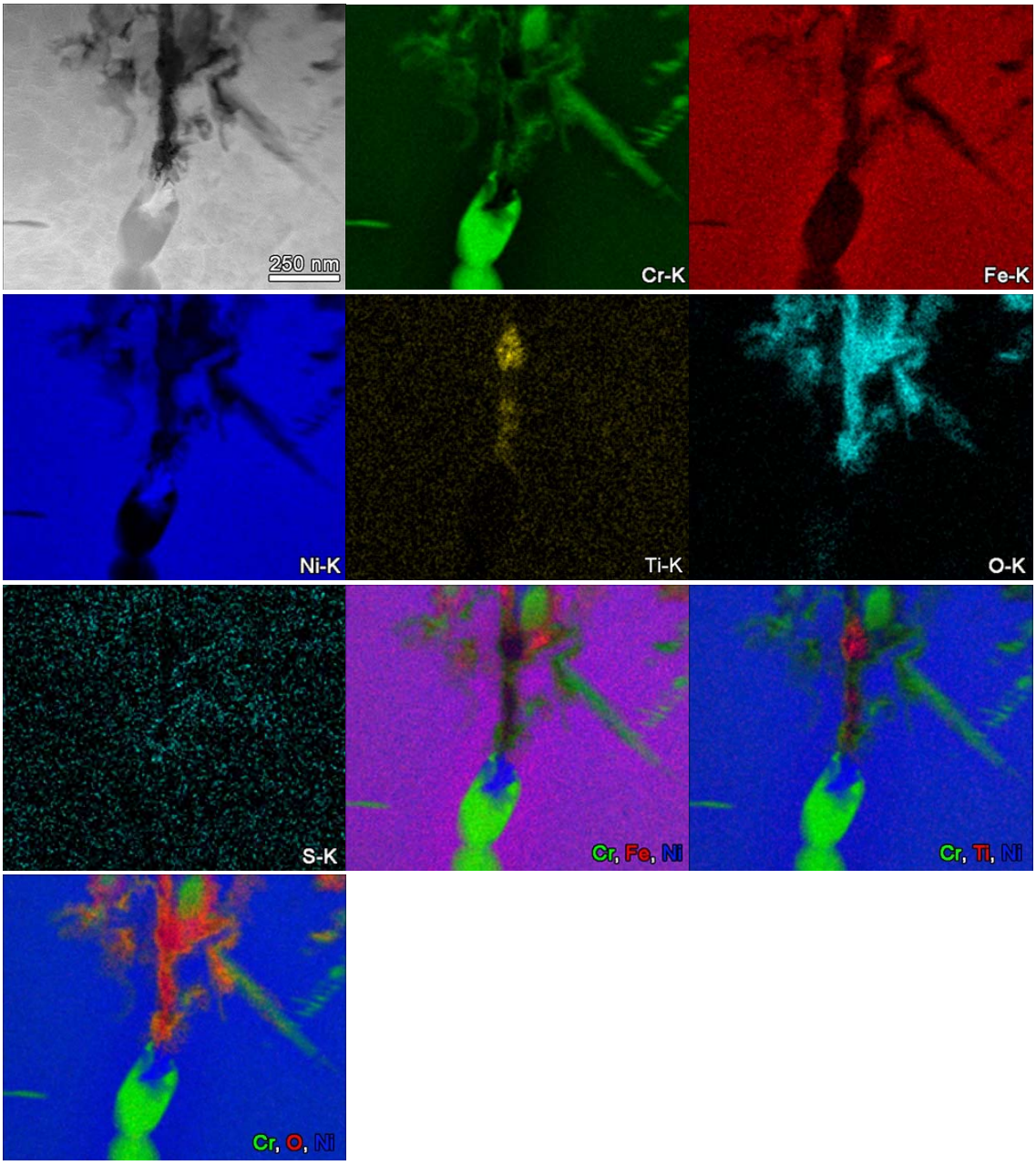

Figure 38. STEM(ADF) and EDS elemental maps showing a representative IGA feature in the non-CW Alloy 600SA heat NX6106XK-11 unstressed coupon after 4400 hours of exposure in simulated PWR primary water at 360°C.

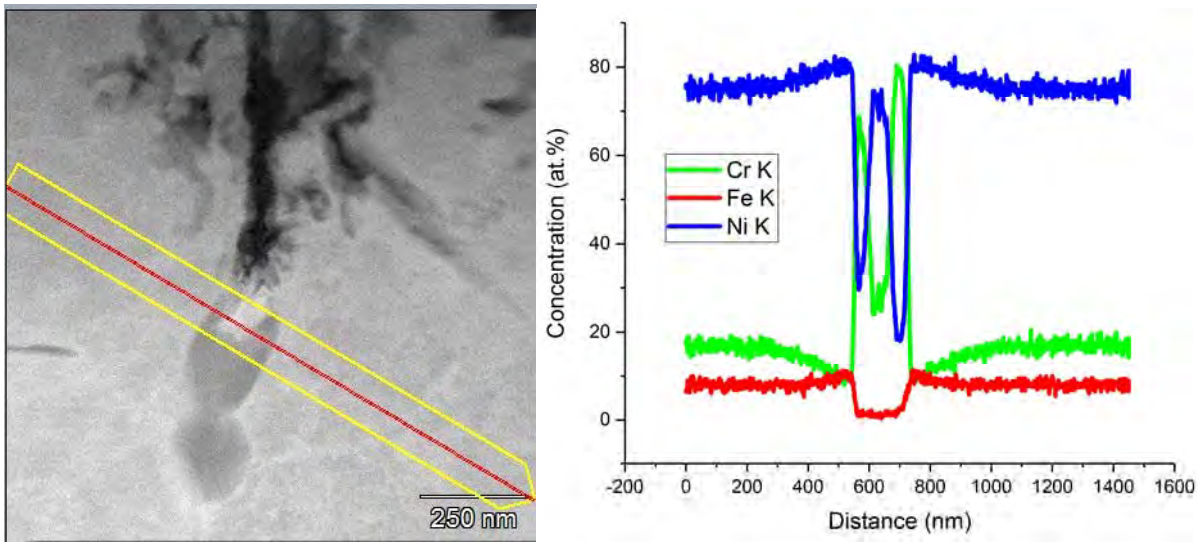

Figure 39. STEM(ADF) and EDS elemental box sum scan across the attacked carbide at the leading IGA front shown in Figures 34-38. Note the Ni enrichment of the attacked carbide and the long-range, shallow Cr depletion into the matrix on either side of the IG carbide from the TT anneal and carbide precipitation.

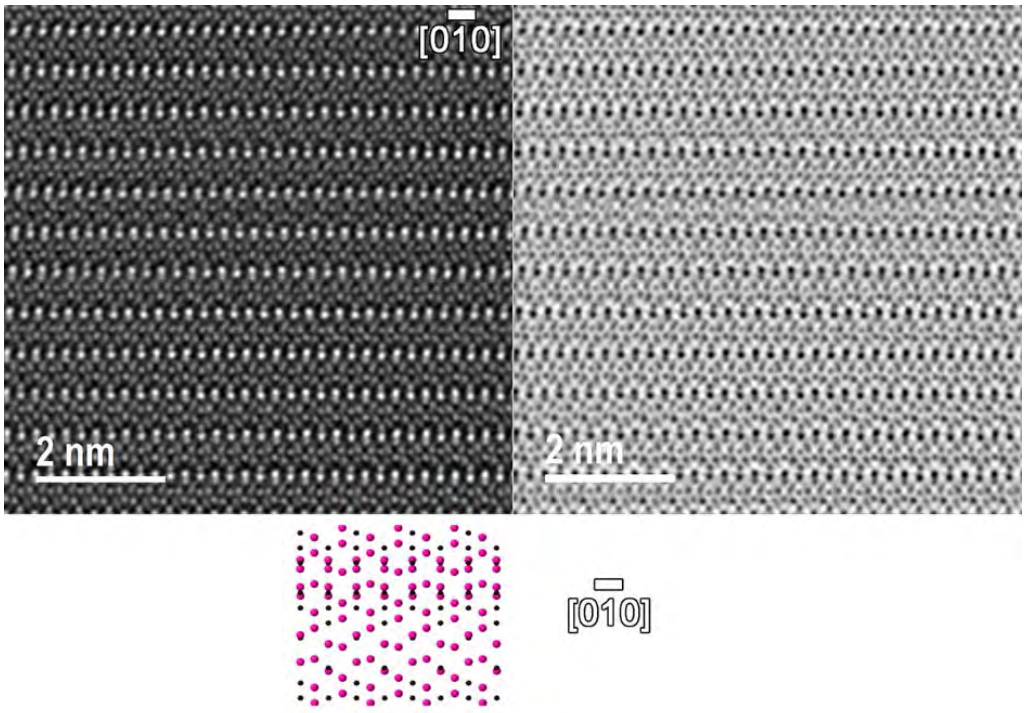

Figure 40. High resolution STEM(ADF and ABF) analysis of the carbide at the leading IGA front shown in Figures 34-38. The carbide structure is consistent with the M_7C_3 structure ([0-10] pole shown).

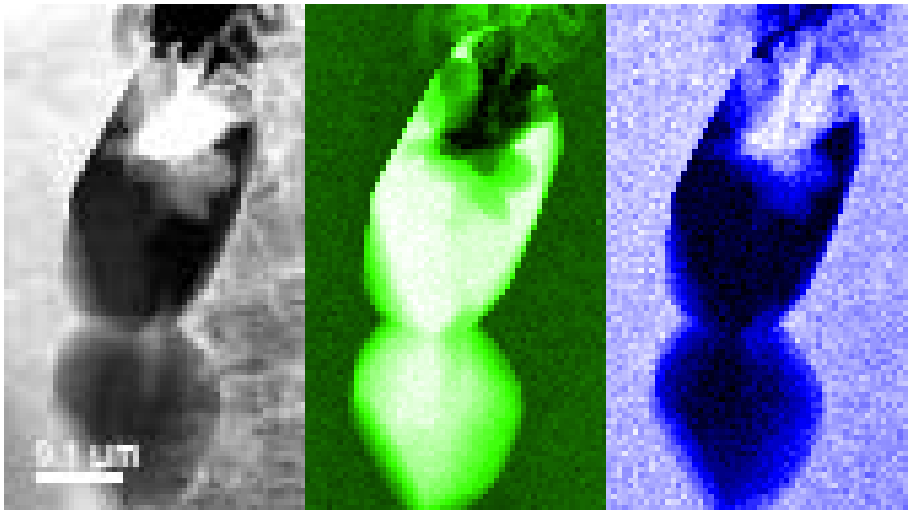

Figure 41. STEM(ADF) and EELS elemental maps (Cr-green, Ni-blue) of the attacked carbide at the leading IGA front shown in Figures 34-38.

APT Characterization of non-CW TT unstressed exposure coupon

An APT reconstruction of the IGA near an IG Cr carbide from heat NX6106XK-11 TT after the 1000 h exposure is presented in Figure 42. The IGA extends from the left toward the right in the atom map with an 85 at.% Cr+O isoconcentration surface (red) delineating regions of Cr_2O_3 within the IGA. The full extent of the oxidation is defined by a 20 at.% O isoconcentration surface (gray) that terminates along the surface of the IG Cr carbide, outlined by a 6 at.% C isoconcentration surface (maroon). From the atom map, it is visually apparent that the surrounding metal matrix is depleted of Cr. A proximity histogram of the oxide/metal interface shown panel (b) quantifies the metal-side depletion of Cr (~2.5 at.%), Fe (~1.3 at.%) and Si (~0.05 at.%). The fact that Fe and Si are depleted along with Cr reveals that the alteration is a result of oxidation and not just Cr carbide precipitation during the thermal treatment. The leading oxide described by this proximity histogram is Cr rich but unlikely to be Cr_2O_3 as strong signals from Ni, Fe and Si are observed. A second APT concentration profile is presented in Figure 42c across the oxide/carbide interface. The oxide in this region is consistent with the preceding proximity histogram, but the interest here is the localized enrichment of Ni at the carbide/oxide interface. This localized Ni enrichment is present across the entire oxide/carbide interface and is consistently observed in APT analyses of oxidized IG carbides in Alloy 600.

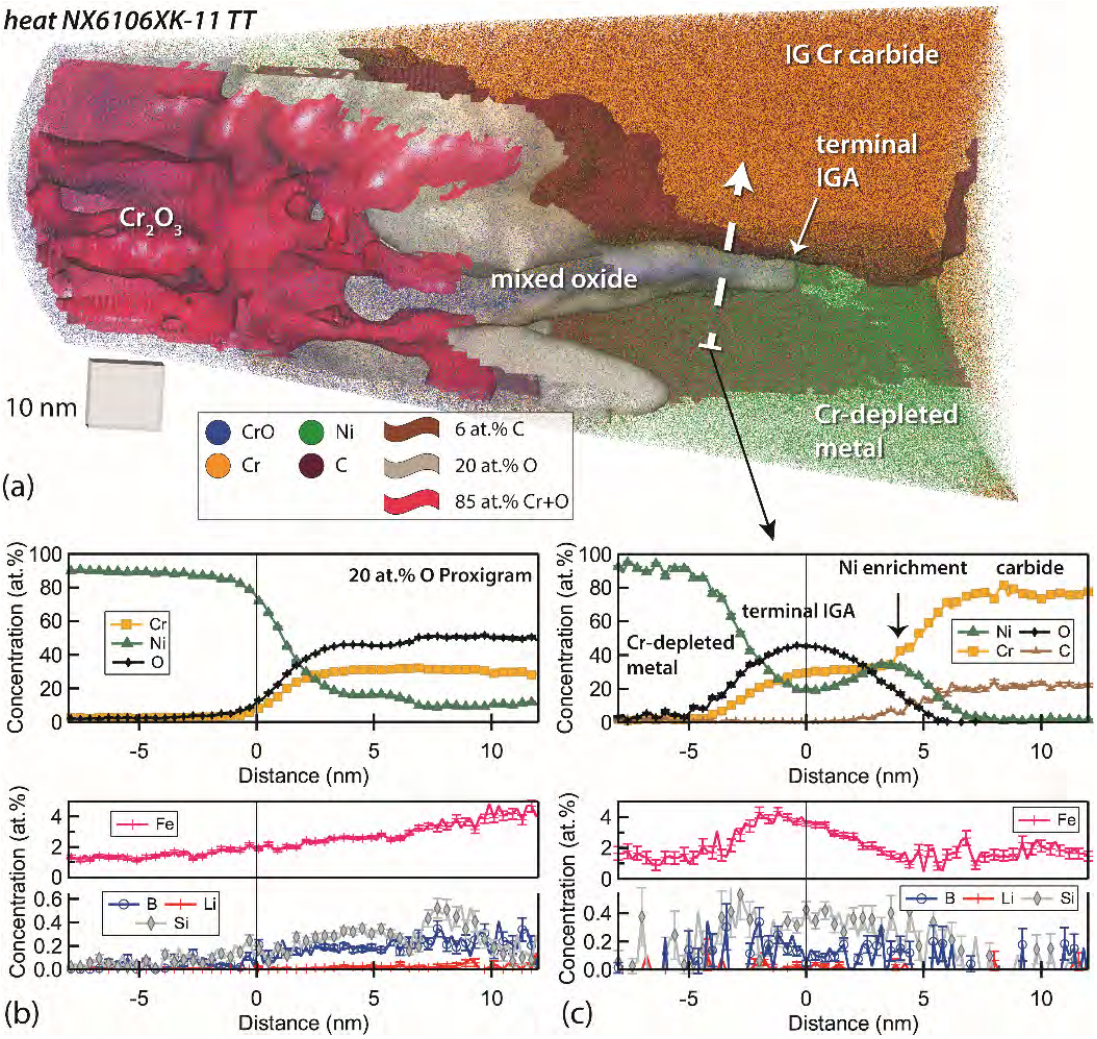

Figure 42. (a) APT reconstruction of the terminal IGA intersecting an IG carbide in the non-CW Alloy 600SA heat NX6106XK-11 unstressed coupon after 1000 hours of exposure to 360°C simulated PWR primary water. (b) Proximity histogram across the metal/oxide interface. (c) 1D concentration profile (dashed arrow) across the terminal IGA/carbide interface. Note the localized Ni enrichment to the interface.

A second example of terminal IGA from APT analysis of the same GB is presented in Figure 43. Isoconcentration surfaces are drawn with 6 at.% O (blue) to outline the location of the terminal IG oxide, 40 at.% Cr+C (maroon) for an IG Cr carbide precipitate, 82 at.% Ni (green) for a Ni-rich / Cr-poor metallic region, and 3 at.% Ti (yellow) for a small region of Ti enrichment along the Cr-poor grain boundary. The general GB plane, determined by SEM imaging during specimen fabrication, extends from the upper right to the lower left. In this case, the IGA again terminated near an IG Cr carbide, but the oxide is not in intimate contact with the carbide itself. The oxide is separated from the carbide by the prominent region of Cr- and Fe-depleted metal. The interface between the IG oxide and the altered metal is presented in panel B, which reports nearly complete depletion of both Fe and Cr. The oxide itself is Cr rich, but again contains a significant amount of Ni (~20 at.% Cr and Ni). Given the approximate O concentration of ~42 at.%, this composition is most consistent with an MO-like oxide phase. Two distinct Ni-rich features are apparent: a very thick region near the tip apex above the IG Cr carbide, and a relatively narrow region adjacent to the carbide extending towards the bottom of the dataset. While the narrow region is typical GB depletion of Cr and Fe from IG oxidation, the upper region could be interpreted as a migrated GB and/or partially consumed Cr carbide that has converted to a Ni-rich metal. In either case, the oxide clearly follows a path separated from the carbide by this Ni-rich metal and is not in direct contact with the carbide itself.

The final feature of this dataset is the Ti-rich region located within the Cr- and Fe-depleted metal near the bottom of the reconstruction. A concentration profile from metal grain 1 into the Ti-rich feature is shown in panel C of Figure 43. It is first noted that grain 1 exhibits a lower Cr concentration (~10 at.% Cr) than the nominal alloy composition due to the material's TT conditioning and Cr carbide precipitation. This dataset also contains a unique Ti-rich region that has not yet been observed in any other Alloy 600 heats at PNNL. No enrichment was found for C or N in this region, suggesting the feature is unlikely associated with the Ti carbonitrides found in this heat. Instead, the region is primarily Ni-rich and Cr/Fe-poor with ~5 at.% Ti and ~0.4 at.% Nb. We speculate this may be a small region of G-phase, but the interpretation is confounded by the coinciding presence of altered alloy composition from both carbide precipitation and IG oxidation. Our TEM analyses of heat NX6106XK-11 TT revealed Ti-rich regions along the GB plane, which were initially thought to be the common Ti carbonitrides observed previously. The density of these IG particles is too low to reliably target by APT characterization. Further analysis of this material without exposure to high-temperature water by TEM would be needed to determine if G-phase is forming during the TT anneal, or if the observed feature in this APT data could result from leaching of C and N from a carbonitride during corrosion.

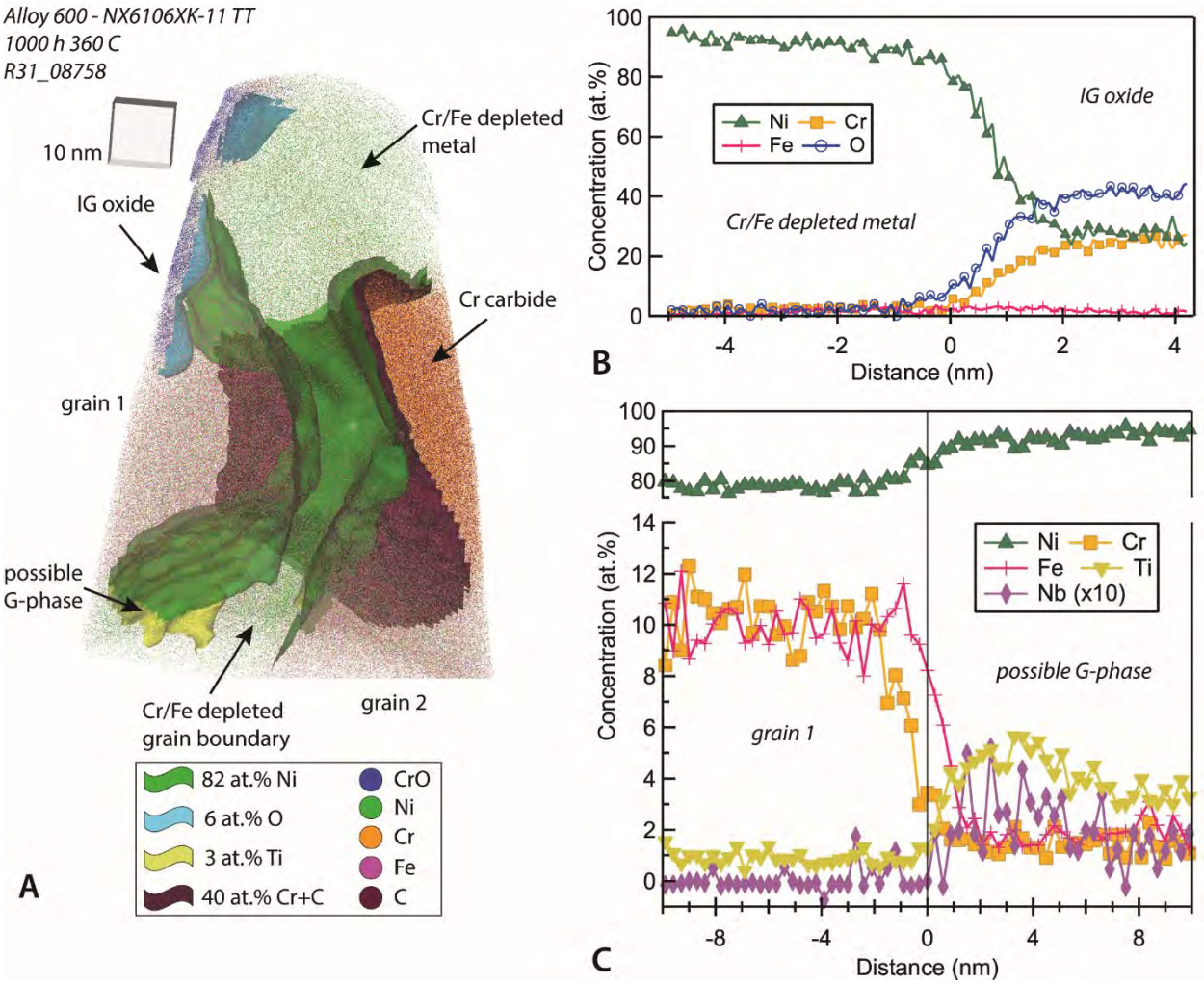

Figure 43. APT characterization of an IGA in the non-CW Alloy 600SA heat NX6106XK-11 unstressed coupon after exposure for 1000 hours to 360°C simulated PWR primary water. (A) 3D elemental atom map and isoconcentration surface depicting regions of IG oxide, IG Cr carbide, and Cr depleted metal. (B) APT concentration profile across the oxide/metal interface showing the presence of a Cr-Ni oxide. Note the extreme level of depletion of Cr and Fe from the adjacent metal. (C) Concentration profile across the interface from the noted grain 1 and a possible IG G-phase region (yellow isosurface in panel A). This identification is speculative and based only on the measured enrichment of Ti and Nb.

Quantification of Precursor Damage Depth Evolution

One key aspect of this study was to evaluate the evolution of the depth of precursor damage in the different material conditions, so that the effect of GB carbide could be evaluated. Therefore, destructive examinations were performed on a cross-section of the unstressed and stressed samples removed after each test interruption. As described earlier, great care was taken during specimen mounting and polishing to preserve the fine IGA features for quantification. To ensure representativeness of the data, IGA depth measurements were performed on more than 100

random high-energy GBs in each specimen. In this section, the results of statistical analyses will be presented in detail.

Summarized first is the cumulative frequency of the depth evolution of precursor damage, which includes IGA and short crack less than 10 um deep, in the SCC initiation specimens for all three material conditions as shown in Figures 44-46. It should be noted that data at each test interruption is acquired from a different specimen, but it is considered the precursor damage development is relatively consistent in all specimens with the same material condition. A gradual increasing trend was observed for the depth of precursor damage with the increase in exposure time. In particular, it is revealed that despite the increase in exposure time, the percentage of GBs that showed a certain degree of cracking remained relatively stable at ~10% for the SA and TT+15%CF conditions, but increased from <5% to >20% in the MA+15%CF condition. To better visualize the contribution of these short cracks to the overall distribution, the depth of short cracks is also plotted for each specimen in the bar diagram in terms of percentage of cracks over all GBs observed. It turns out that with the progression of test time, the formation of new cracks in the SA and TT+15%CF condition appears limited because the specimens underwent longer exposure did not show a higher fraction of very short cracks, but instead, they show a higher distribution gravitating towards deeper cracks. This suggests that in all material conditions, nucleation of new cracks decreases as exposure time increases, although IGA continues to grow. One possible explanation for this phenomenon is that the transition from IGA to short cracks is associated with bulk creep strain rate – with the exhaustion of primary creep at early stage of the tests, it becomes difficult for new cracks to form compared to growth of existing cracks.

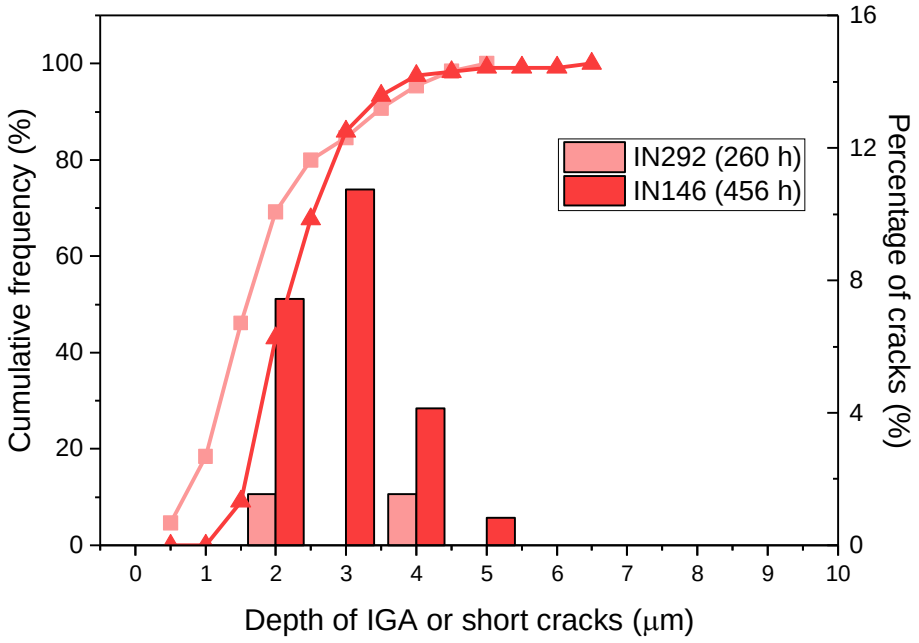

Figure 44. Cumulative frequency of precursor damage depth for the 15%CF Alloy 600MA heat NX6106XK-11 SCC initiation specimens taken out at each test interruption and the conclusion of the tests in 360°C simulated PWR primary water.

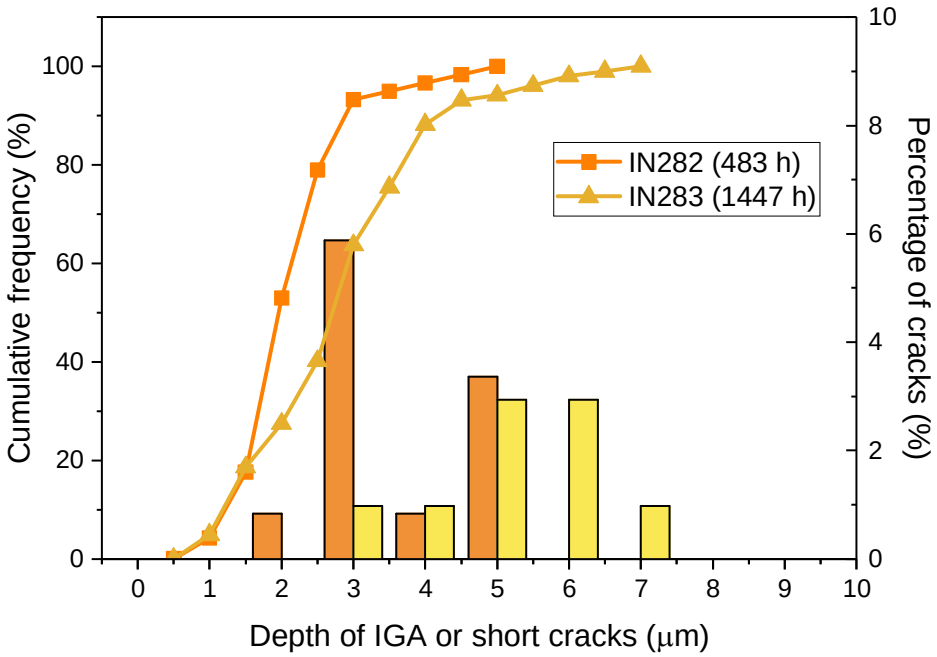

Figure 45. Cumulative frequency of precursor damage depth for the 15%CF Alloy 600SA heat NX6106XK-11 SCC initiation specimens taken out at each test interruption and the conclusion of the tests in 360°C simulated PWR primary water.

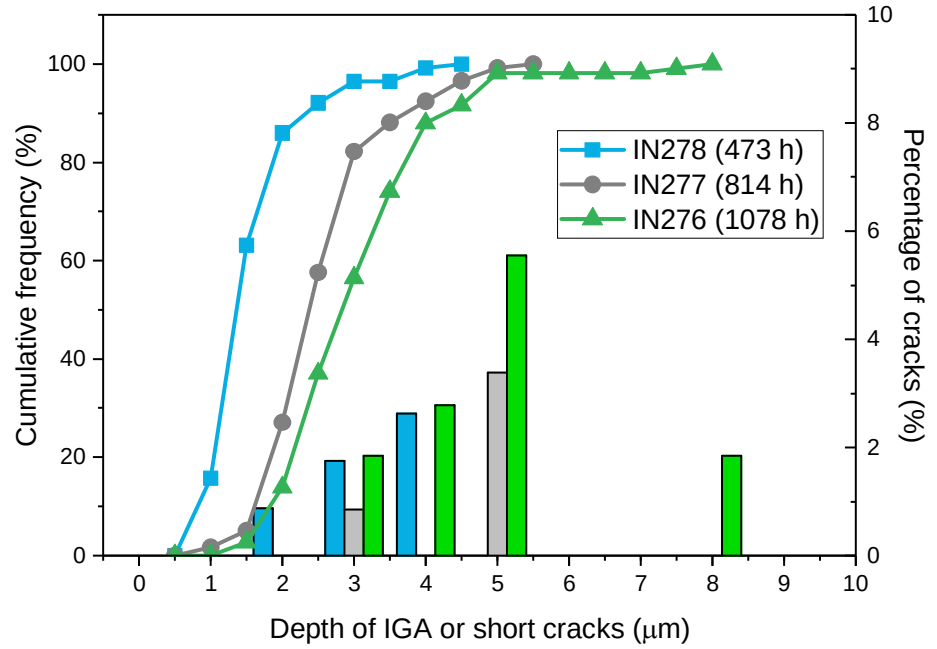

Figure 46. Cumulative frequency of precursor damage depth for the 15%CF Alloy 600TT heat NX6106XK-11 SCC initiation specimens taken out at each test interruption and the conclusion of the tests in 360°C simulated PWR primary water.

A specific examination was also conducted on the evolution of average IGA depth (excluding all IG cracks) in both the unstressed and stressed samples as a function of exposure time in all material conditions. In the unstressed coupons, the MA, SA and TT all exhibit an average IGA depth between 0.8 and 1.5 um with little growth from 1000 hours to 4400 hours. In comparison, the depth of stress-assisted IGA in the 15%CF MA, SA and TT SCC initiation specimens all increased with exposure time albeit the trend appears to be slowing down at longer times. In particular, the MA+15%CF specimens showed slightly deeper stress-assisted IGA than the specimens in the other two material conditions after similar exposure times. This suggests that the MA+15%CF is more susceptible to IGA when a load is applied. Also, the average IGA depth in the 15%CF SA and TT SCC initiation specimens is already twice that in the unstressed coupons after 1000 hours of exposure, suggesting a significant role played by applied stress in IGA development.

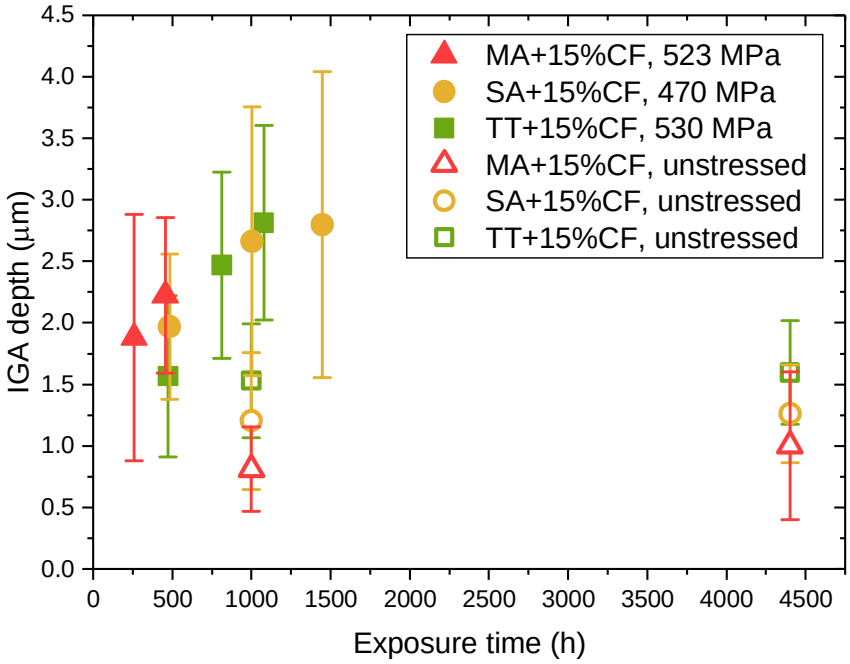

Figure 47. Summary of the time evolution of average IGA depth in the 15%CF Alloy 600MA, SA and TT heat NX6106XK-11 unstressed exposure coupons and SCC initiation specimens loaded at yield stress in 360°C simulated PWR primary water.

SCC Initiation Response

SCC initiation behavior of the 15%CF MA, SA, and SA+TT conditions were each evaluated using six tensile specimens in 360^{o}C simulated PWR primary water. A summary of the status of all the SCC initiation specimens is provided in Table 3. The MA+15%CF material was evaluated three specimens at a time in two separate tests. IN146-148 were tested as part of the round robin initiated by the International Cooperative Group on Environmentally - Assisted Cracking of Water Reactor Materials (ICG-EAC). These three specimens exhibited unexpected low SCC initiation times (~300-400 hours) compared to the same material at 7% and 18-19%CW conditions (~1000-1500 hours). Post-test SEM characterization revealed that this is likely associated with presence of large elongated grains intersecting the gauge surface [21]. To exclude potential effects of microstructural inhomogeneity on SCC initiation, another set of three specimens IN291-293 were tested after prior-test examination confirmed that elongated grains were not present at the surface in any of these three specimens. A single test was performed for the six SA+15%CF specimens IN282-287 and another for the six SA+TT+15%CF specimens IN273-278. In these two tests, one specimen from each material condition was intentionally removed at ~480 hours before SCC initiation for examination of precursor damage, while the remaining five were all removed after SCC initiation was confirmed by DCPD. In the following section, the SCC initiation response and morphology will be summarized in detail for each material condition.

Table 3. Summary of specimens, material conditions and SCC initiation response for the Alloy 600 heat NX6106XK-11.

Spec. ID	Material Condition	Surface Finish	Applied Stress (MPa)	Time to SCC Initiation (h)
IN146	MA + 15%CF	1 µm	548	396
IN147	MA + 15%CF	1 µm	535	385
IN148	MA + 15%CF	1 µm	548	219
IN291	MA + 15%CF	1 µm	516	252
IN292	MA + 15%CF	1 µm	515	247
IN293	MA + 15%CF	1 µm	521	221
IN273	TT + 15%CF	1 µm	533	957
IN274	TT + 15%CF	1 µm	533	820
IN275	TT + 15%CF	1 µm	530	550
IN276	TT + 15%CF	1 µm	532	817
IN277	TT + 15%CF	1 µm	532	530
IN278	TT + 15%CF	1 µm	530	NI (473)*
IN282	SA + 15%CF	1 µm	466	NI (483)*
IN283	SA + 15%CF	1 µm	467	1100
IN284	SA + 15%CF	1 µm	467	842
IN285	SA + 15%CF	1 µm	468	1062
IN286	SA + 15%CF	1 µm	467	912
IN287	SA + 15%CF	1 µm	473	801

* NI = no initiation, specimen was removed before DCPD detection of SCC initiation for precursor damage examination.

SCC Initiation Behavior in Heat NX6106XK-11 MA+15%CF Condition

The DCPD referenced strain response of the first set of the 15%CF A600MA heat NX6106XK-11 specimens IN146-148 is shown in Figure 48. These three specimens exhibit classic behavior of CW Alloy 600 where an obvious upturn in the DCPD referenced strain took place upon practical SCC initiation. Although the three specimens showed consistent SCC initiation times between 220-400 hours, these values are unexpectedly low compared to the SCC initiation times of ~1200-1800 hours previously obtained from the same material with cold work levels of 7% and 18%. Post-test SEM-BSE montage images revealed that the early initiations detected in these three specimens can possibly be associated with microstructural inhomogeneity intrinsic to this material condition where crack nucleation and growth tend to take place at the grain boundary between large elongated grains and smaller grains. The post-test gauge surface morphology is shown for IN148 in Figure 49 on the rotation where most cracks were formed. In Figure 49b, the cracks are highlighted in red while the uncracked GBs are delineated in yellow. This was made possible by the IGA formed along high-energy GBs soon after the start of the test. It is obvious that the primary crack in this specimen nucleated along the GB of a large elongated grain in a banded region. A similar observation was found for IN146 where only

one large crack was observed. The morphology and shear bands associated with this crack indicate that it first nucleated along one side of a large elongated grain and then extended further as the test continued (Figure 50). This was confirmed by comparing the surface morphology along the crack to that recorded at a test interruption after 250 hours of exposure. As shown in Figure 51, IGA was identified along many high energy GBs, but only one small IG crack (~60 μm in length) was found along the boundary of the large elongated grain and indicated that this is the site where crack first nucleated. The last MA+15%CF specimen IN147 in the same series showed DCPD detection of initiation at ~385 hours and propagated to failure before the test was stopped. Therefore, microstructural characterization was conducted on the fractured surface instead of the gauge surface for this specimen. As shown in Figure 52, a large elongated grain protruding into the gauge for ~1 mm in depth was found on the crack plane, again suggesting the important role of microstructural inhomogeneity in SCC initiation.

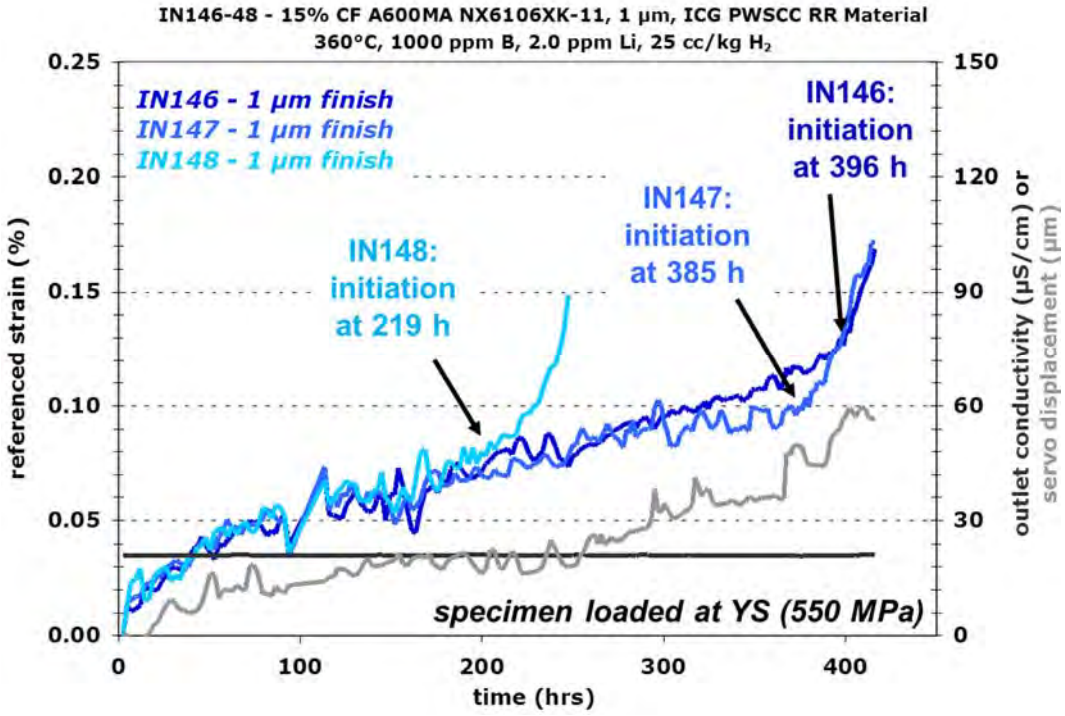

Figure 48. Referenced DCPD strain response showing early initiation for the 15%CF specimens IN146-148 from the MA Alloy 600 plate heat NX6106XK-11 tested in 360°C simulated PWR primary water.

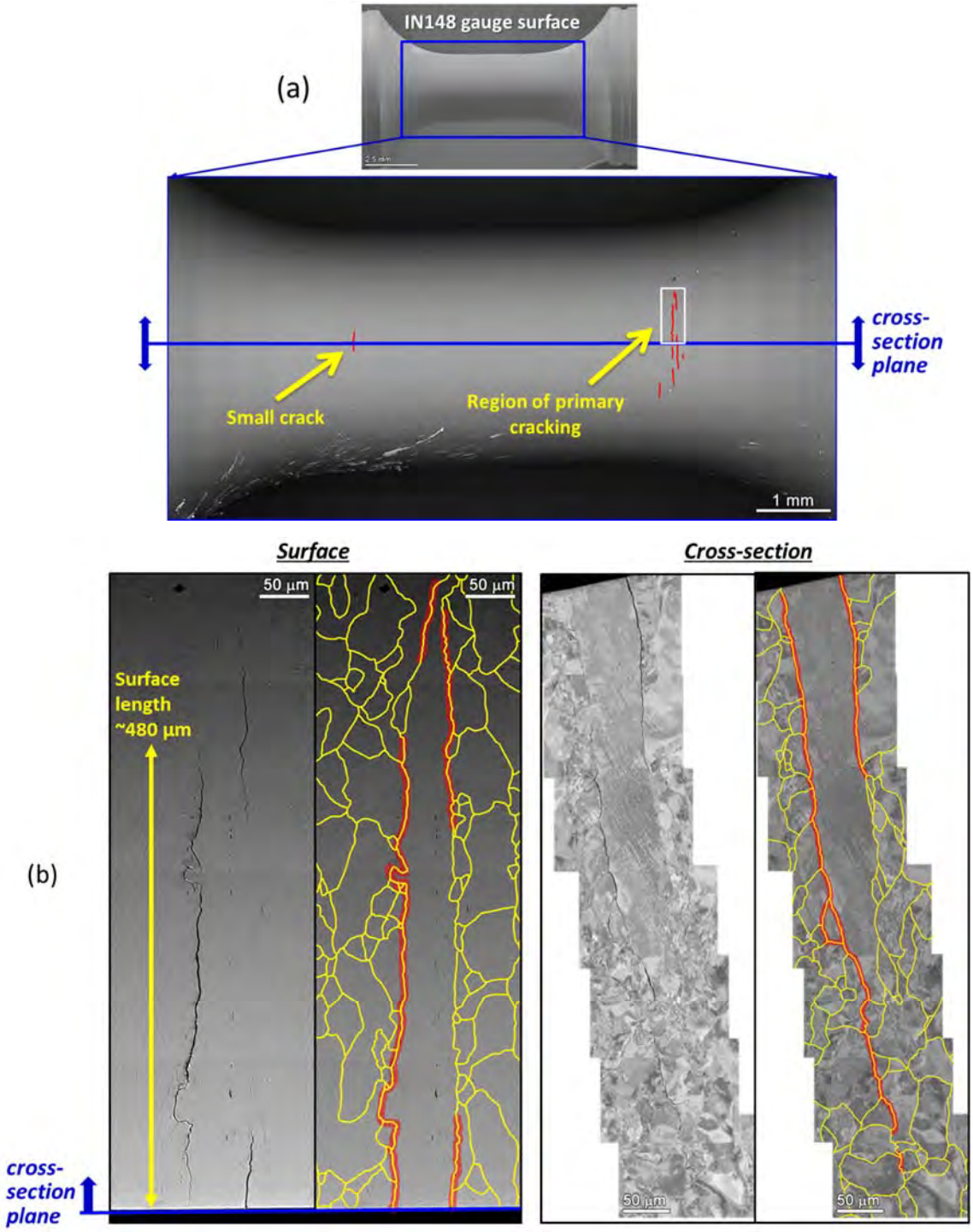

Figure 49. Post-test SEM-BSE imaging of the MA+15%CF Alloy 600 plate heat NX6106XK-11 specimen IN148 with DCPD initiation detection at 219 hours of exposure (total exposure of 250 hours): (a) crack locations on the gauge surface and (b) the surface and cross-section morphology of the primary crack in the highlighted region in (a). The cracks are highlighted in red and the grain boundaries are highlighted in yellow.

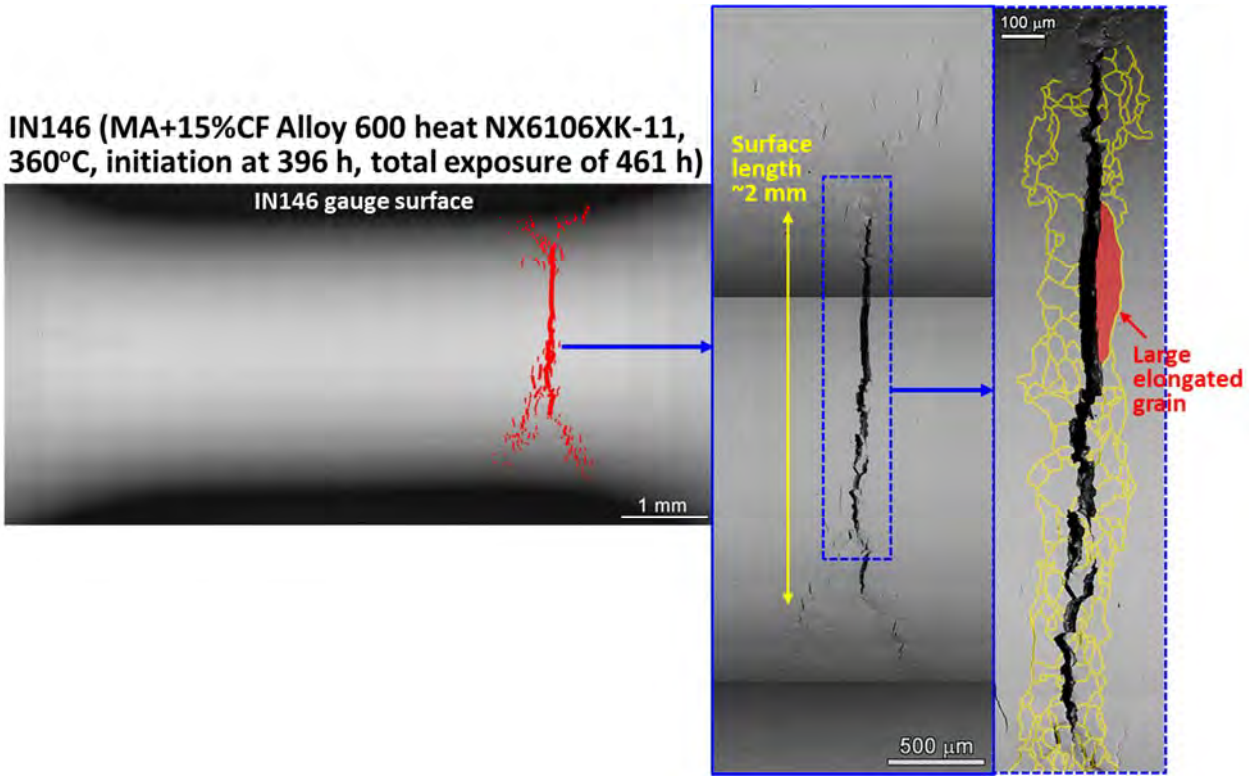

Figure 50. Post-test SEM-BSE imaging on the gauge surface of the MA+15%CF Alloy 600 plate heat NX6106XK-11 specimen IN146 with DCPD initiation detection at 396 hours of exposure (total exposure of 461 hours). The primary crack was found to nucleate along an elongated large grain in a banded region where grain boundaries are highlighted in yellow.

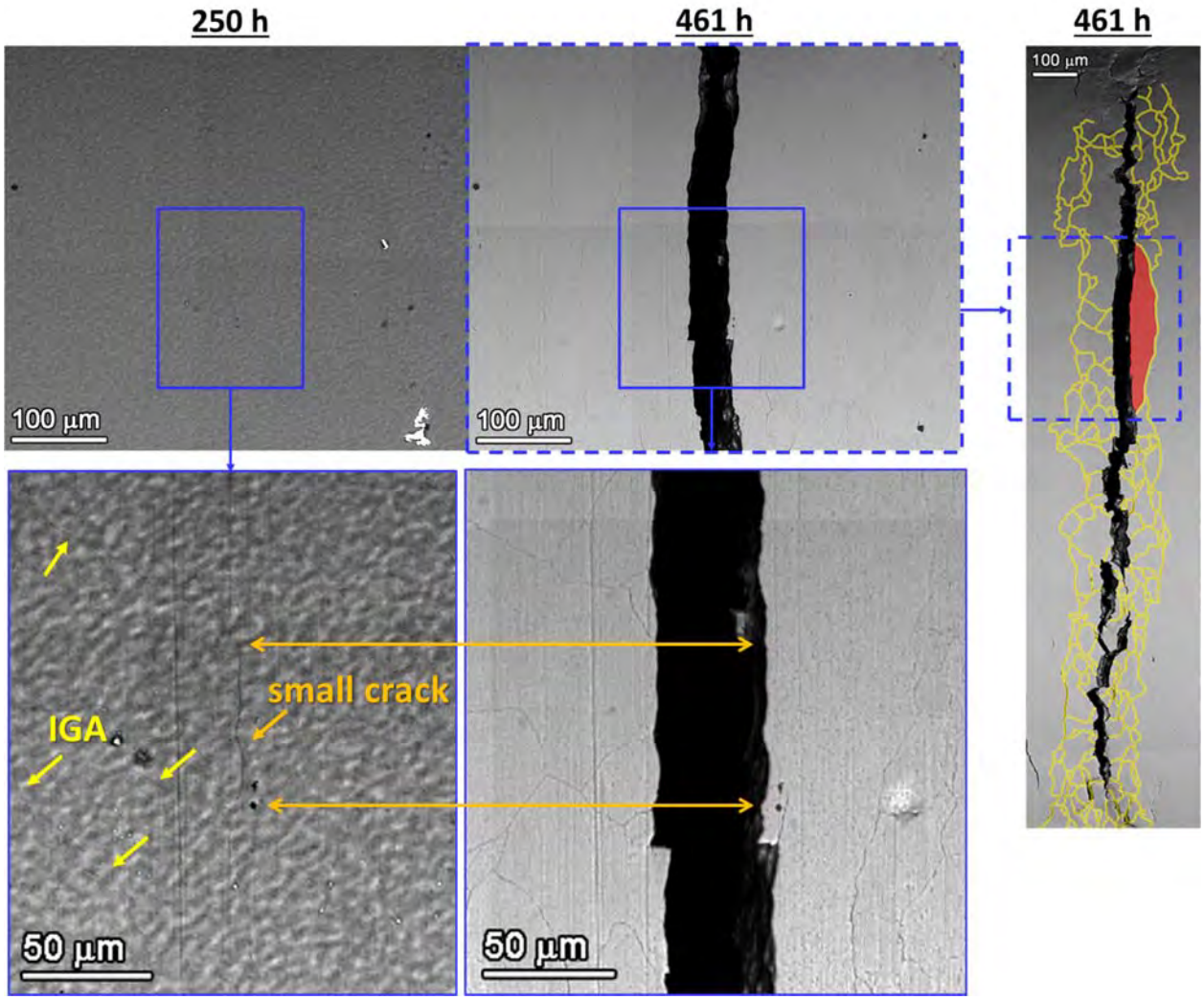

Figure 51. Evolution of the gauge surface in the vicinity of the large elongated grain of the MA+15%CF Alloy 600 plate heat NX6106XK-11 specimen IN146 before (left) and after (right) DCPD initiation detection. IGA were observed on a large number of high energy GBs (highlighted in yellow) despite of the surface oxides obscuring a clear view. However, only a small crack (highlighted in orange) was found along the boundary of the large elongated grain after 250 hours of exposure.

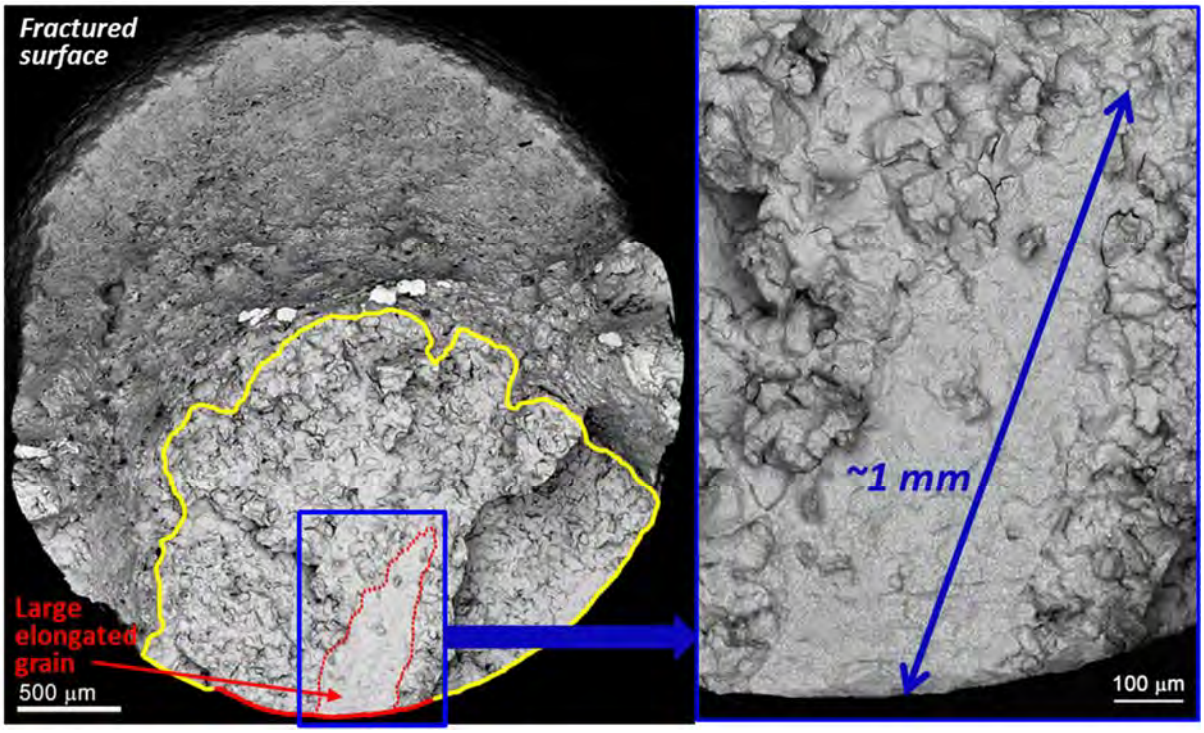

Figure 52. SEM-BSE imaging on the fracture surface of the MA+15%CF alloy 600 plate heat NX6106XK-11 specimen IN147 with DCPD initiation detection at 385 hours of exposure. The region of IG failure is enclosed in yellow with the primary crack on the surface identified in red. The region of the large elongated grain is outlined using dashed red lines to aid visualization and a zoom-in image of the region is provided on the right side.

Based on optical microscope observations, the banded microstructure in the Alloy 600 heat NX6106XK-11 is highly localized. Therefore, to investigate the SCC initiation behavior without possible influence of the microstructural inhomogeneity, a second set of three specimens were machined from a different location in the plate and the grain microstructure on the surface of the specimens was examined prior to the testing to ensure these specimens do not contain large elongated grains. To achieve this, a brief electroetching using 10% oxalic acid at room temperature and ~7V for 30 seconds was performed on these specimens after the gauge surface was polished to a 1 µm finish. This etching method is effective for revealing most of the GBs in the material. The entire gauge surface of each specimen was then mapped in the SEM and confirmed that there were no large elongated grains in any of these specimens. The specimen gauge surfaces were then repolished and SCC initiation testing was conducted in simulated PWR primary water at 360°C with the overall DCPD response shown in Figure 53. Surprisingly, these specimens again exhibited very low SCC initiation times, even lower than IN146-148 which contain large elongated grains. To double check, surface examinations were performed using SEM backscattered imaging on these specimens with results summarized in Figures 54-56 in a decreasing order of SCC initiation times. In these figures, the surface of the entire gauge section and part of the fillet region was mapped and the cracks are highlighted in red. Only a few cracks were found in these specimens, and there is always one crack in each specimen exhibiting longer

surface length and wider opening than the others, suggesting they are the dominant crack that has led to the DCPD detection of SCC initiation. By comparing the location of the cracks to the surrounding grain microstructure revealed by the etching applied prior to the test, it was confirmed that the dominant crack in these specimens were not associated with large elongated grains.

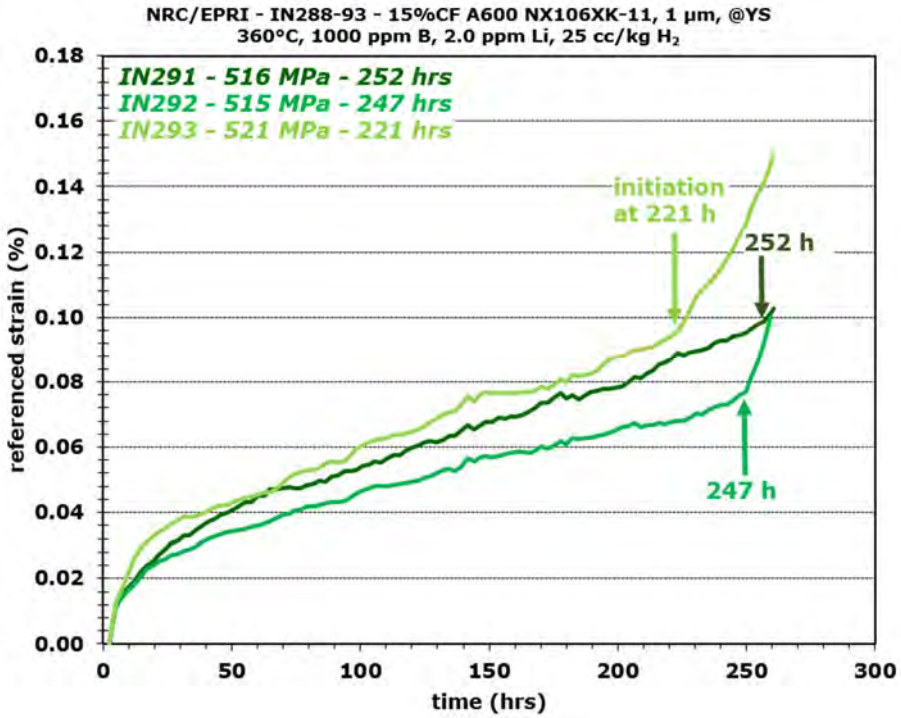

Figure 53. Referenced DCPD strain response showing early initiation for the 15%CF specimens IN291-293 from the MA Alloy 600 plate heat NX6106XK-11 tested at their yield stress at 360ºC.

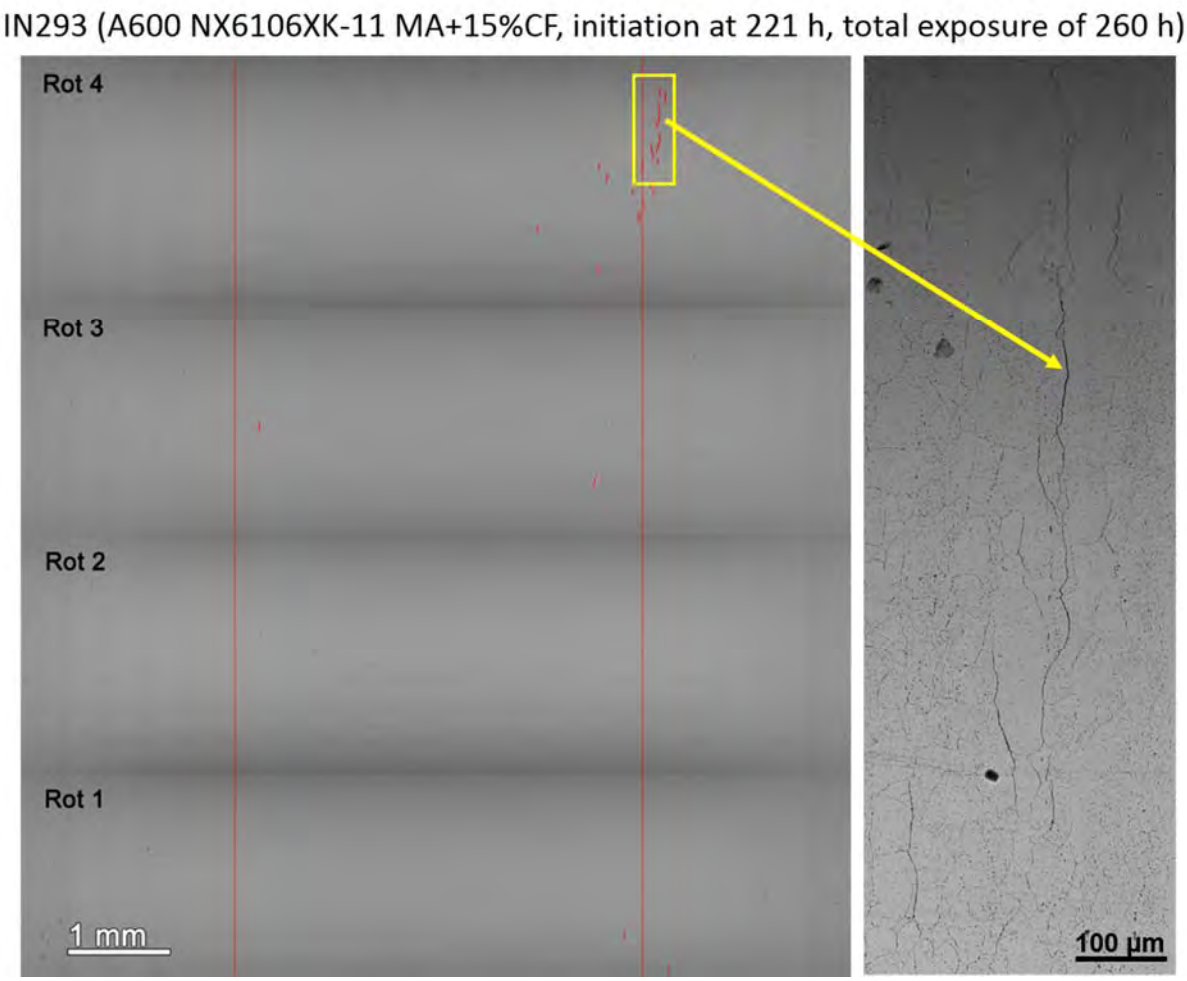

Figure 54. Post-test SEM-BSE montage image of the 15%CF Alloy 600MA heat NX6106XK-11 specimen IN293 after 260 hours of exposure with SCC initiation detected by DPCD at 221 hours. The obvious cracks in the montage image were highlighted in red. A zoom-in image of the largest cracks found on the surface is also shown.

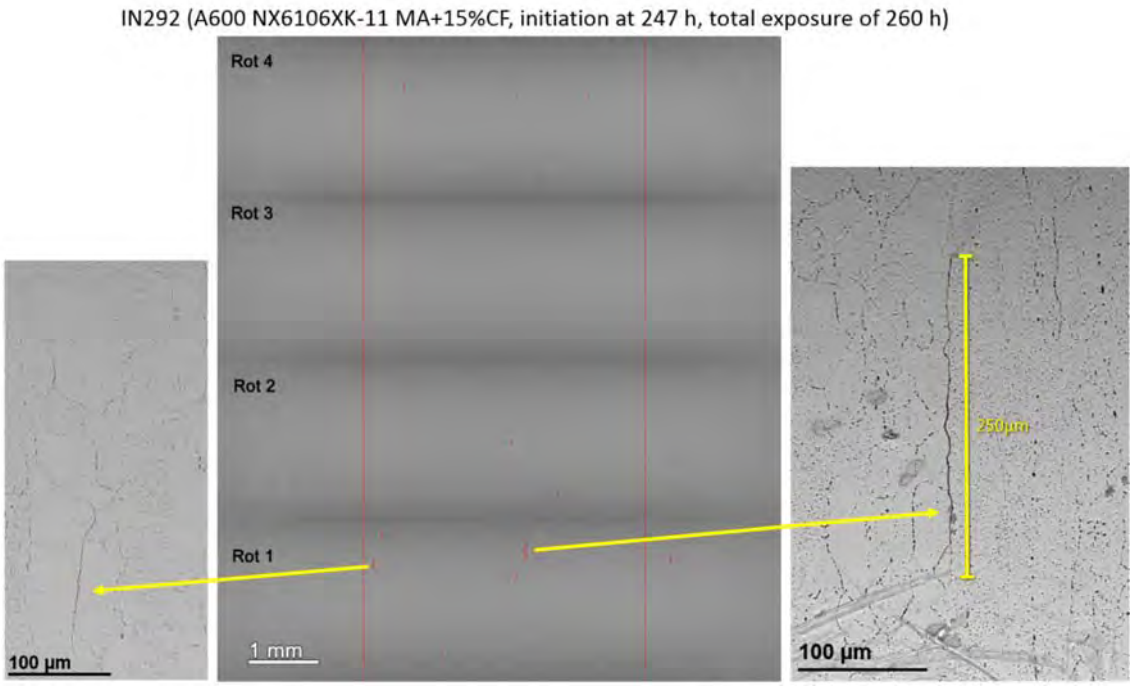

Figure 55. Post-test SEM-BSE montage image of the 15%CF Alloy 600MA heat NX6106XK-11 specimen IN292 after 260 hours of exposure with SCC initiation detected by DPCD at 247 hours. The obvious cracks in the montage image were highlighted in red. Zoom-in images of the two largest cracks found on the surface are also shown.

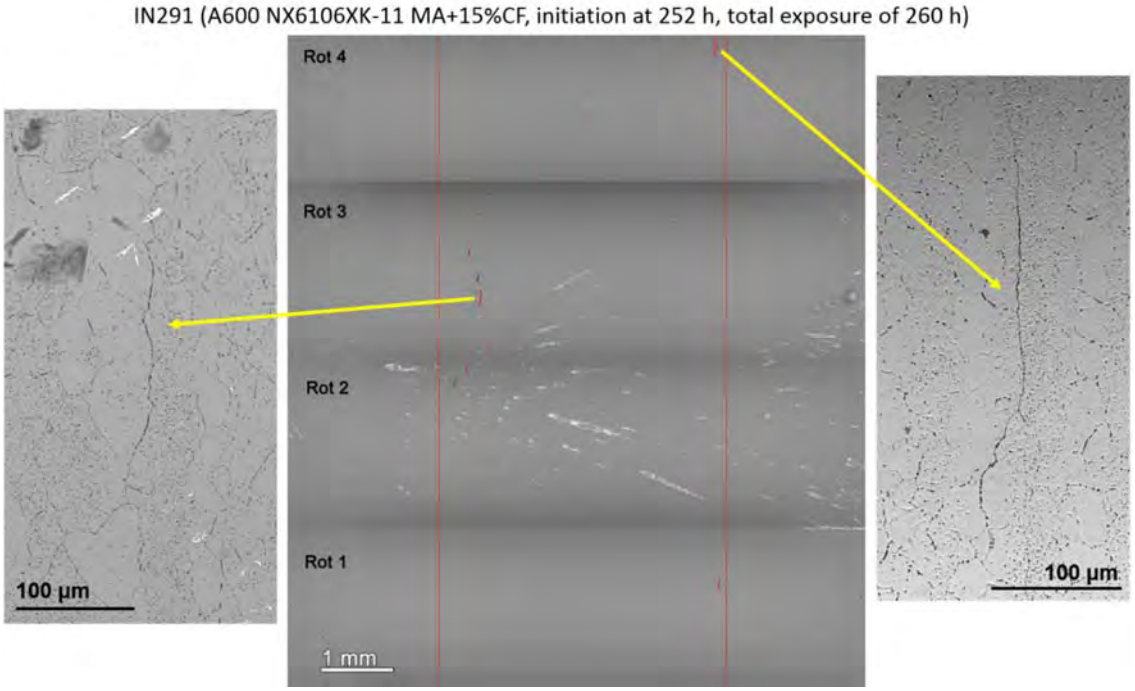

Figure 56. Post-test SEM-BSE montage image of the 15%CF Alloy 600MA heat NX6106XK-11 specimen IN291 after 260 hours of exposure with SCC initiation detected by DPCD at 252 hours. The obvious cracks in the montage image were highlighted in red. Zoom-in images of the two largest cracks found on the surface are also shown.

SCC Initiation Behavior in Heat NX6106XK-11 SA+15%CF Condition

The overall DCPD referenced strain response of the six 15%CF A600SA heat NX6106XK-11 specimens IN282-287 is shown in Figure 57. Unlike the specimens tested in MA+15%CF, the SA+15%CF specimens all exhibit considerably more gradual increase in strain making the determination of SCC initiation challenging at times. Specimen IN282 was removed from the test before detection of SCC initiation for destructive examination of precursor damage and the other five specimens all showed consistent SCC initiation times between 800-1100 hours. SEM surface examinations were performed on these specimens at each test interruption and after test conclusion with results presented in Figures 58-62 in order of their SCC initiation time. The evolution of surface morphology revealed an interesting trend. For the three specimens IN284, IN286 and IN287 which initiated between 800-950 hours, crack formation was already evidenced at the first test interruption at 483 hours, and a high density of cracks were observed on the surface by the time these specimens were removed at 1078 hours. Surface examinations showed that many cracks exhibit similar surface length and openings in these specimens, making it difficult to relate the DCPD detection of SCC initiation to a single dominant crack (Figures 58-60). In fact, it is more likely that the detection of SCC initiation is induced by growth of multiple cracks and not caused by fast growth of a single dominant crack. The reduction in cross-section induced by slower growth of several small cracks may explain the gradual increase in DCPD strain rate leading to practical SCC initiation. In comparison, the two specimens initiated after 1000 hours exhibit much less cracking at the first two test interruptions, and a high density of cracks by the time the test ended (Figures 61-62).

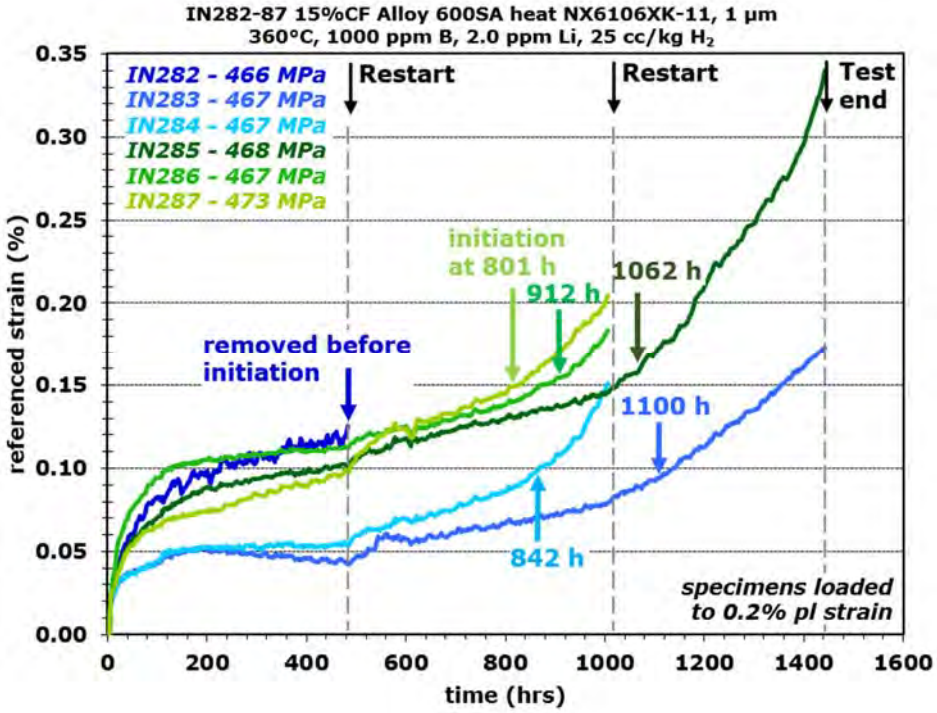

Figure 57. Overall referenced DCPD strain response for the 15%CF Alloy 600SA heat NX6106XK-11 specimens tested at yield stress in 360°C simulated PWR primary water.

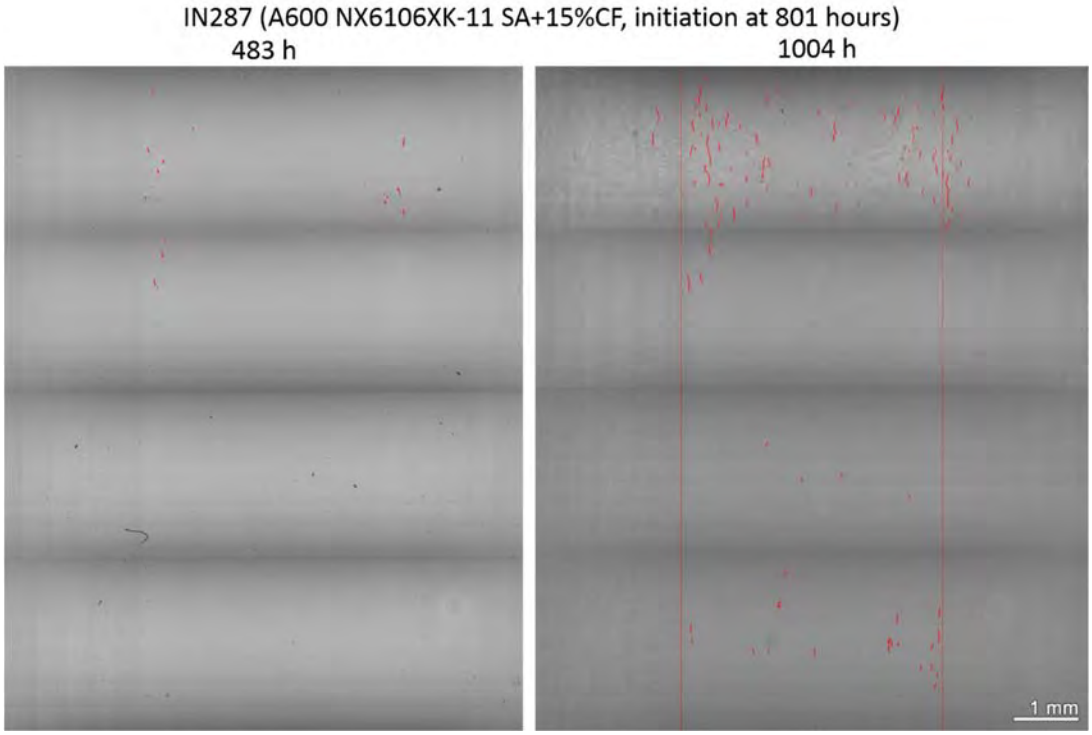

Figure 58. Mid- and post-test SEM-BSE montage image of the surface of the 15%CF Alloy 600SA heat NX6106XK-11 specimen IN287 in which SCC initiation was detected by DPCD at 801 hours of exposure at yield stress. Obvious cracks are highlighted in red.

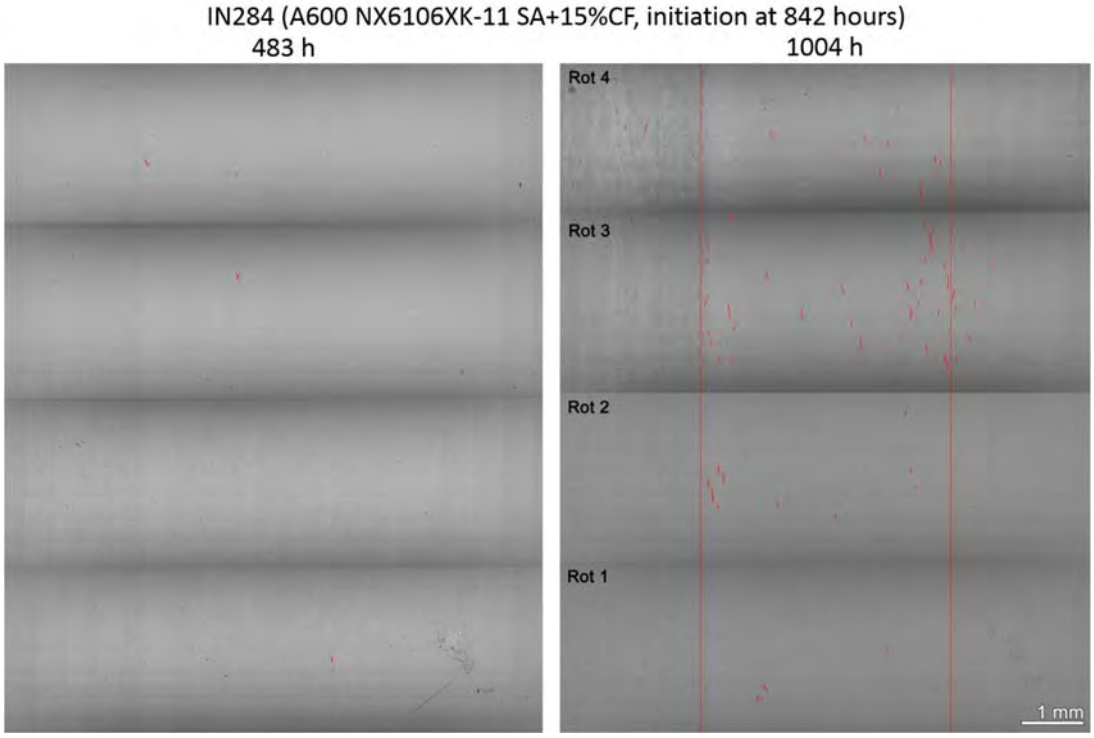

Figure 59. Mid- and post-test SEM-BSE montage image of the surface of the 15%CF Alloy 600SA heat NX6106XK-11 specimen IN284 in which SCC initiation was detected by DPCD at 842 hours of exposure at yield stress. Obvious cracks are highlighted in red.

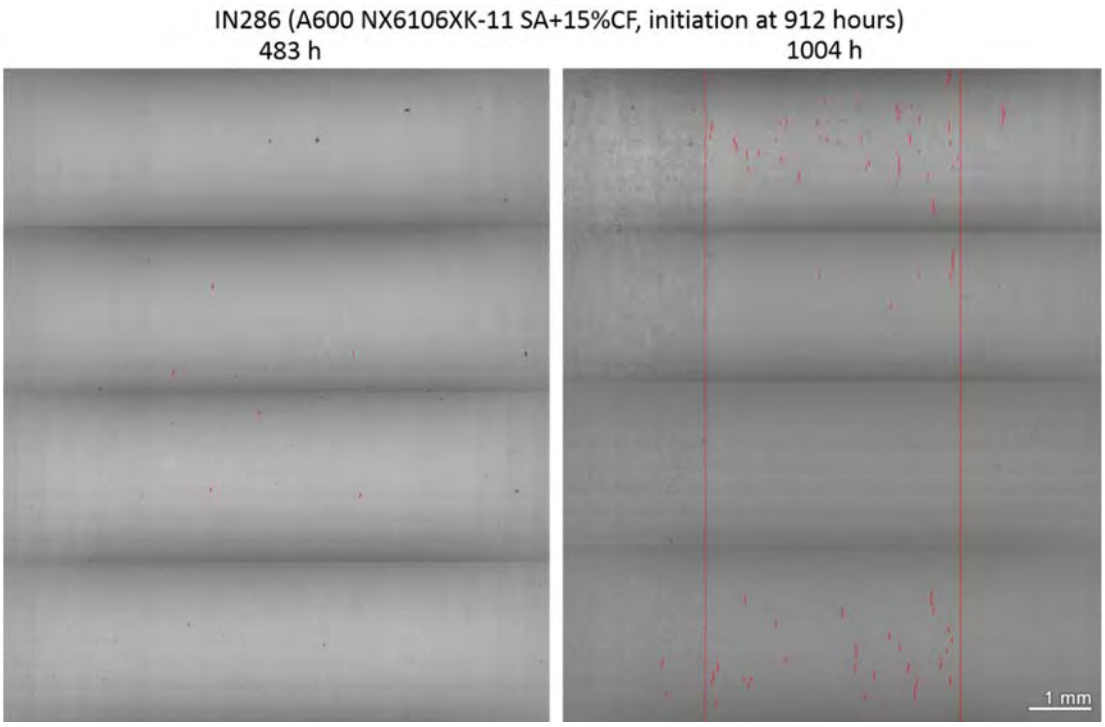

Figure 60. Mid- and post-test SEM-BSE montage image of the surface of the 15%CF Alloy 600SA heat NX6106XK-11 specimen IN286 in which SCC initiation was detected by DPCD at 912 hours of exposure at yield stress. Obvious cracks are highlighted in red.

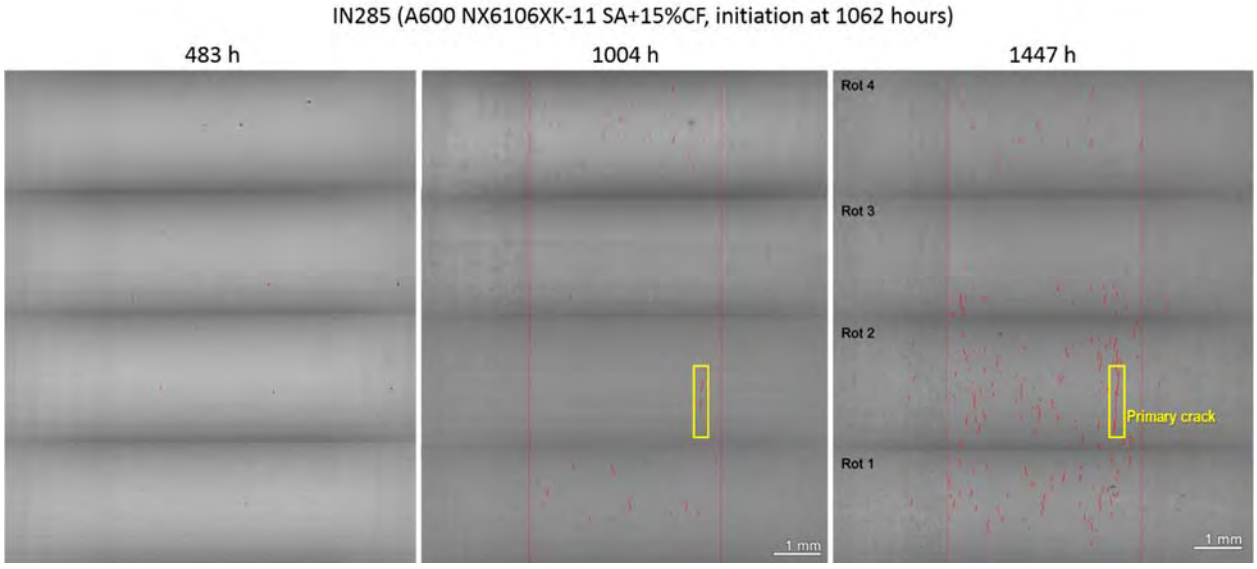

Figure 61. Mid- and post-test SEM-BSE montage image of the surface of the 15%CF Alloy 600SA heat NX6106XK-11 specimen IN285 in which SCC initiation was detected by DPCD at 1062 hours of exposure at yield stress. Obvious cracks are highlighted in red.

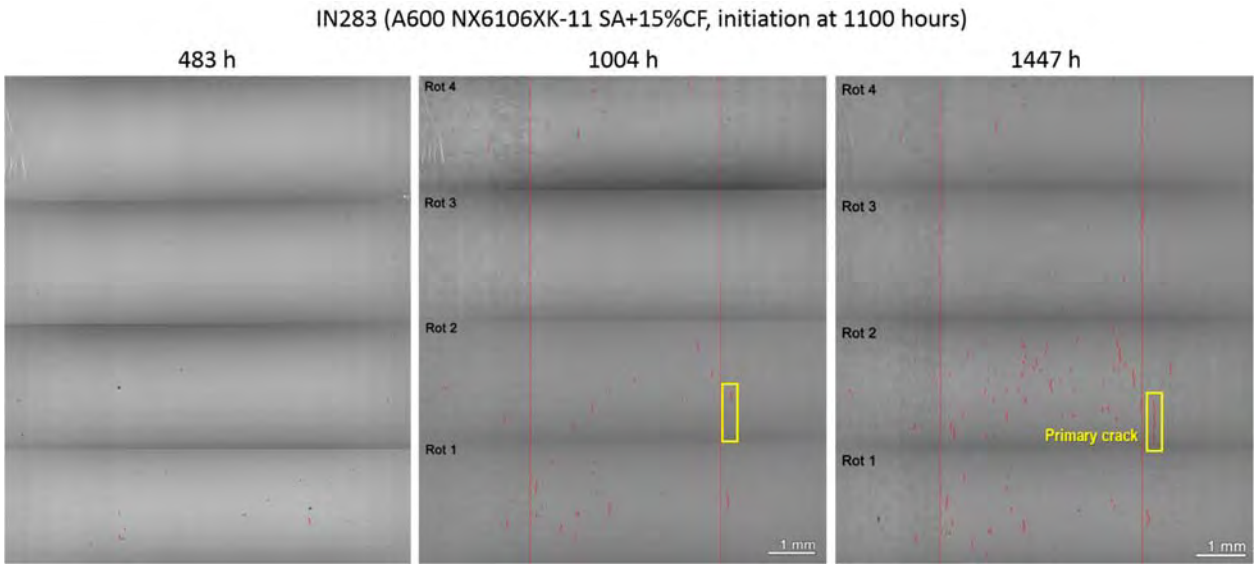

Figure 62. Mid- and post-test SEM-BSE montage image of the surface of the 15%CF Alloy 600SA heat NX6106XK-11 specimen IN283 in which SCC initiation was detected by DPCD at 1100 hours of exposure at yield stress. Obvious cracks are highlighted in red.

SCC Initiation Behavior in Heat NX6106XK-11 TT+15%CF Condition

The overall DCPD referenced strain response of the six 15%CF A600TT heat NX6106XK-11 specimens IN273-278 is shown in Figure 63. The test was continued until SCC initiation was detected by DCPD in all specimens except IN278, which was taken out at 473 hours for destructive examination of precursor damage. Interestingly, the TT+15%CF specimens exhibit very similar SCC initiation behavior as the SA+15%CF specimens in terms of DCPD strain response (a gradual increase in strain rate), SCC initiation time (530-960 hours), and the two types of surface crack morphology evolution. In Figures 64, 66, 68, 70 and 72, the evolution of surface morphology of the five initiated specimens are shown in an increasing order of SCC initiation time. Again, the two specimens IN275 and IN277 that initiated earlier (530-550 hours) showed faster nucleation and higher density of cracks, and the SCC initiation appears to be associated with the growth of multiple cracks. This is evidenced in the close-up images of areas containing relatively large cracks in each specimen as shown in Figure 65 for IN277 and Figure 67 for IN275, where cracks of similar length (200-300 μm) are seen with comparable openings. In specimens IN273, 274 and 276 that initiated after 800 hours, the DCPD detection of SCC initiation is likely associated with the growth of one single predominant crack. An example is shown in Figure 69 for IN276, where close-up images are shown for three different areas containing relatively large cracks at the same scale for direct comparison of crack size. It turns out that the crack at Site B exhibits the longest surface length with the widest opening, suggesting it's the primary crack. Likewise, the primary crack in the other two specimens are easy to identify with details shown in Figures 71 and 73.

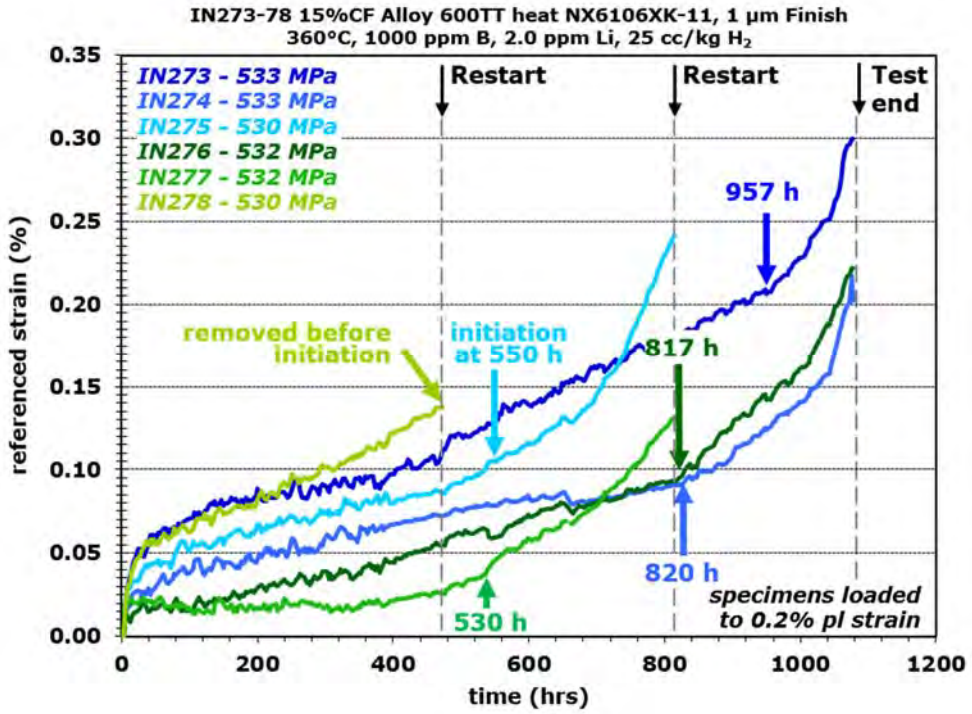

Figure 63. Overall referenced DCPD strain response for the 15%CF Alloy 600TT heat NX6106XK-11 specimens tested in 360°C simulated PWR primary water.

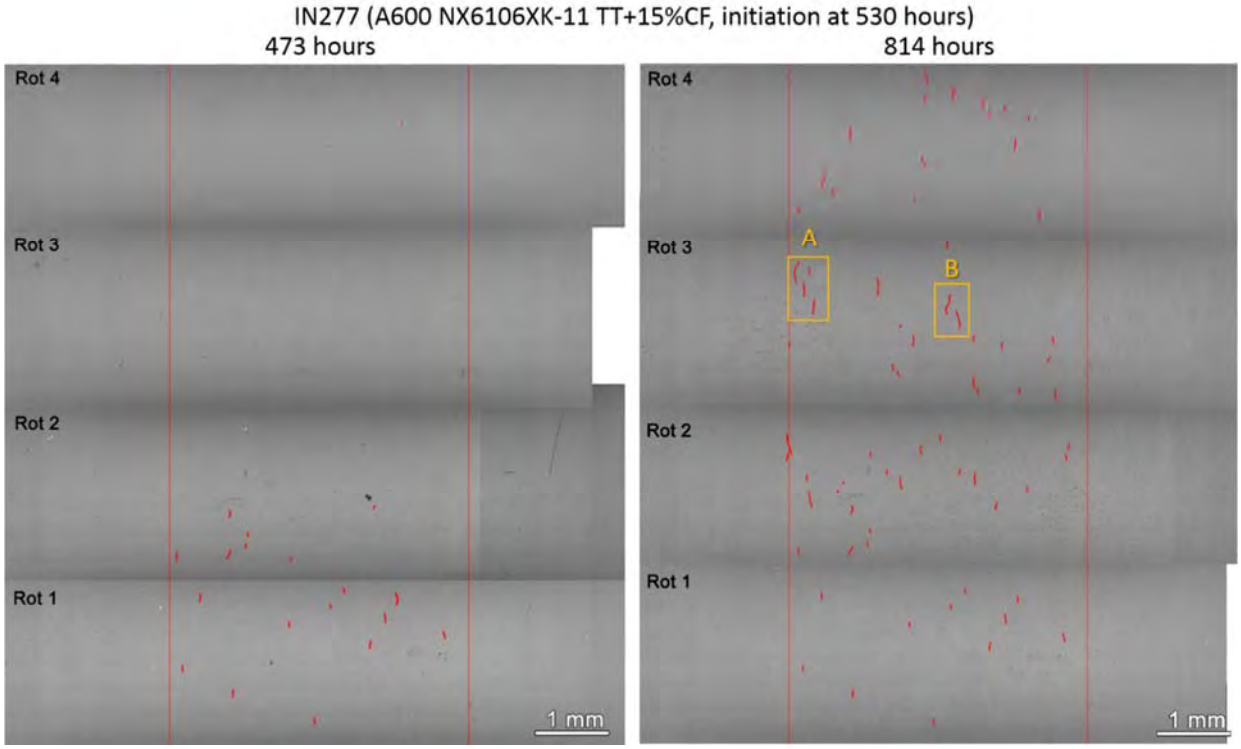

Figure 64. Mid- and post-test SEM-BSE montage image of the surface of the 15%CF Alloy 600TT heat NX6106XK-11 specimen IN277 in which SCC initiation was detected by DPCD at 530 hours of exposure. Obvious cracks are highlighted in red.

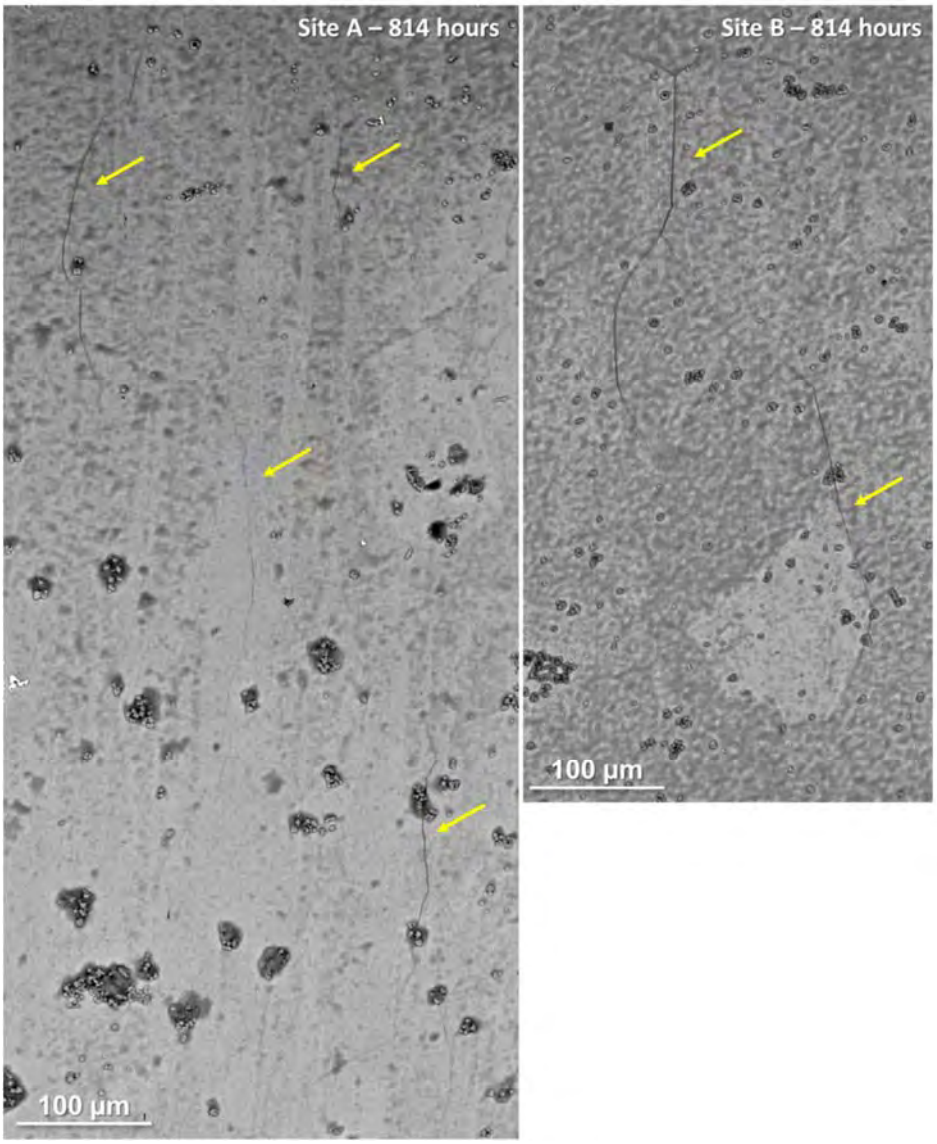

Figure 65. Zoom-in SEM-BSE images of post-test crack morphology on the surface of IN277 at Sites A and B as highlighted in Figure 64.

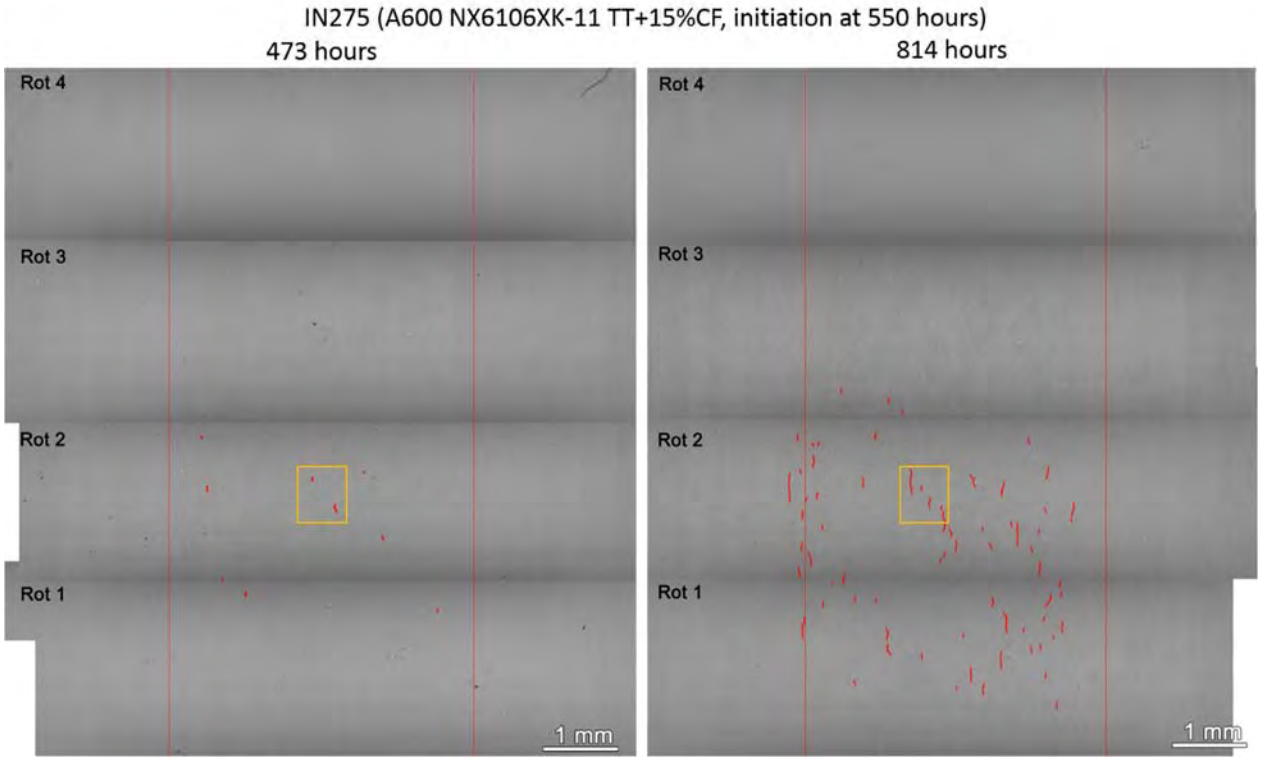

Figure 66. Mid- and post-test SEM-BSE montage image of the surface of the 15%CF Alloy 600TT heat NX6106XK-11 specimen IN277 in which SCC initiation was detected by DPCD at 550 hours of exposure at yield stress. Obvious cracks are highlighted in red.

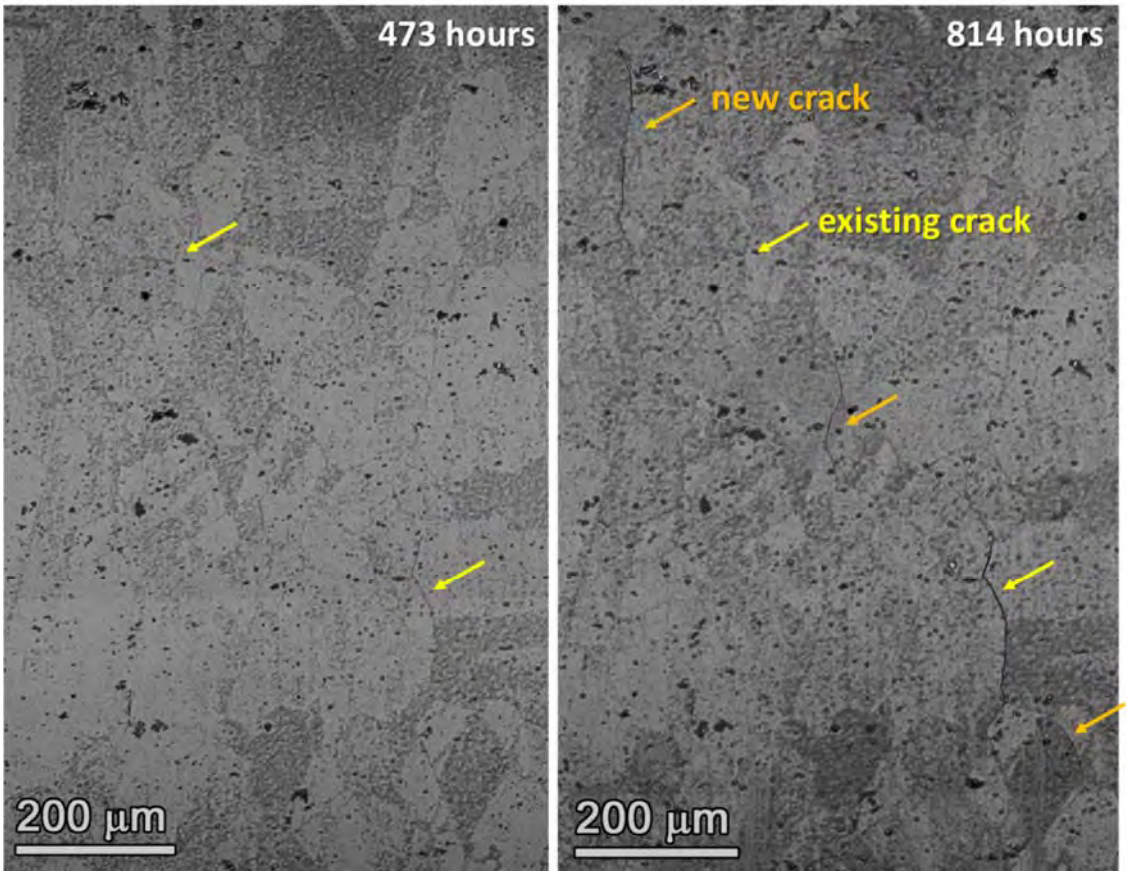

Figure 67. Zoom-in SEM-BSE images on the mid- and post-test crack morphology of IN275 in the area highlighted in Figure 66.

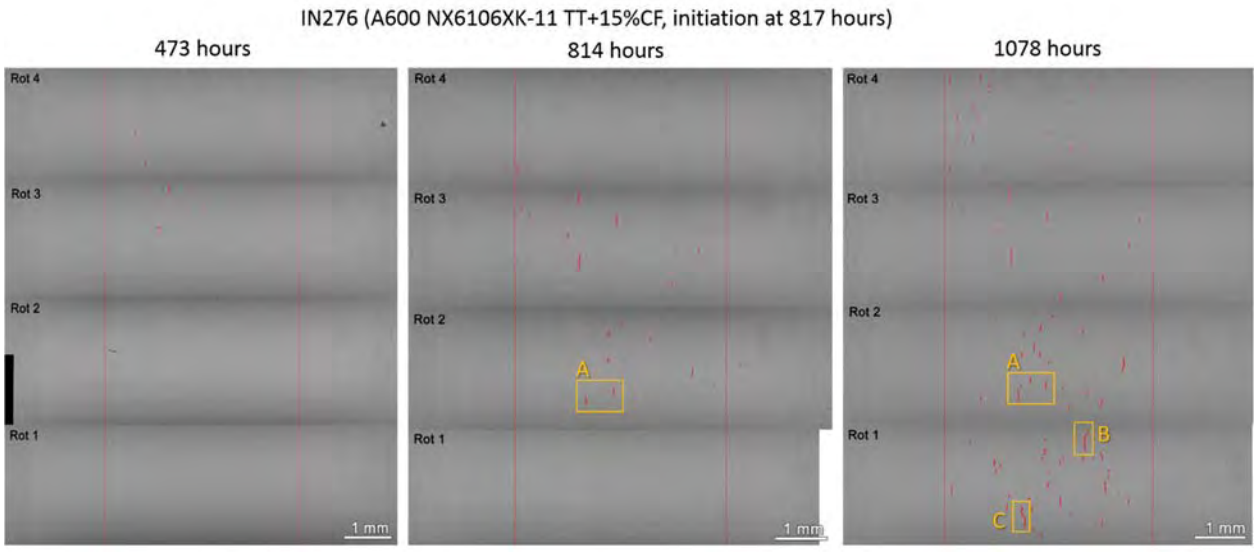

Figure 68. Mid- and post-test SEM-BSE montage image of the surface of the 15%CF Alloy 600TT heat NX6106XK-11 specimen IN276 in which SCC initiation was detected by DPCD at 817 hours of exposure. Obvious cracks are highlighted in red.

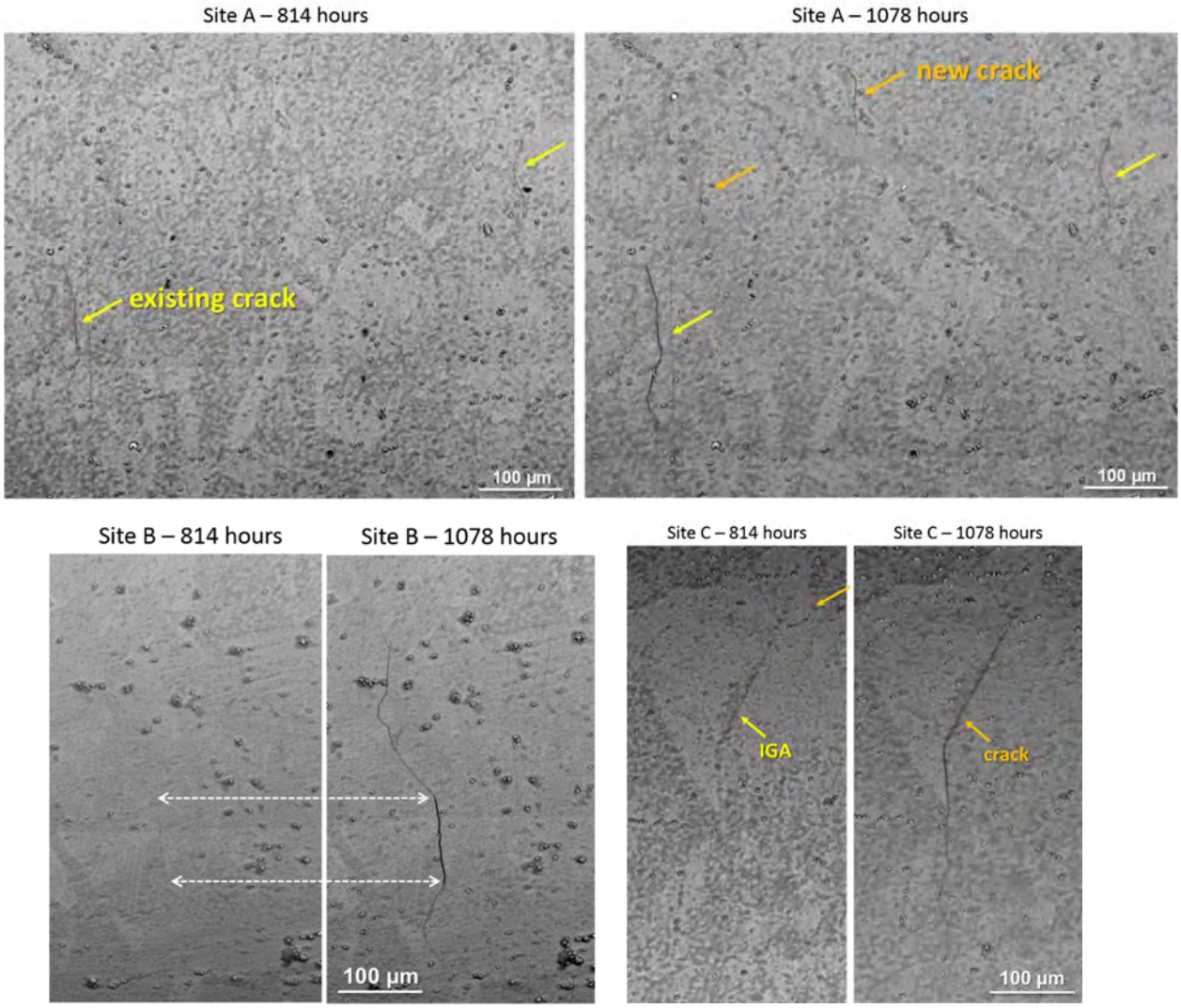

Figure 69. Zoom-in SEM-BSE images on the mid- and post-test crack morphology of IN276 at Sites A, B and C as highlighted in Figure 68. The images at the three sites are shown at the same scale for direct comparison of crack surface length and opening.

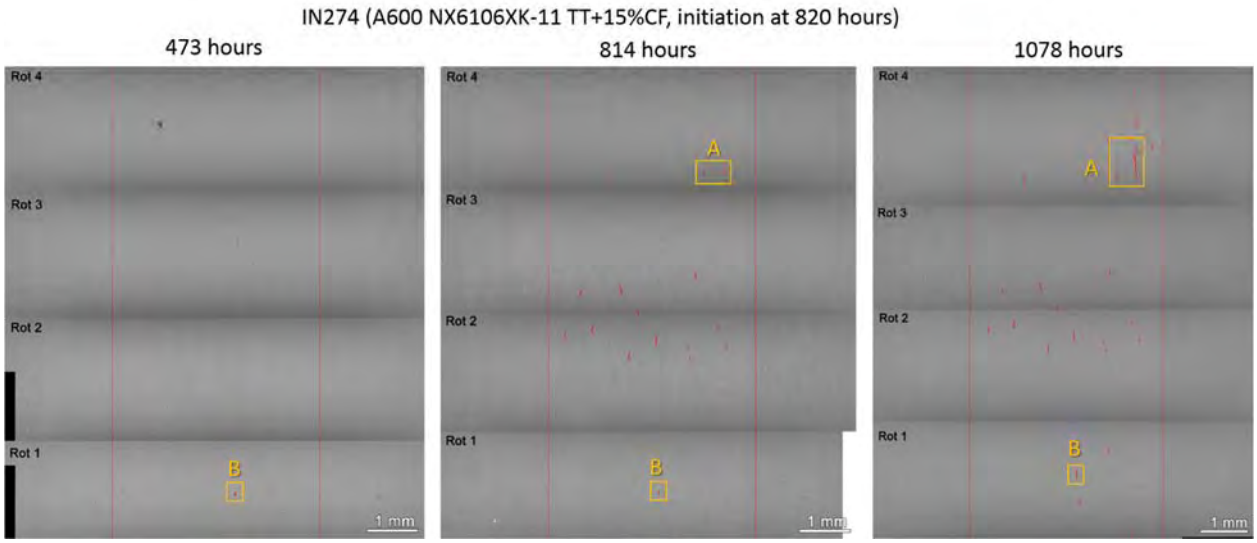

Figure 70. Mid- and post-test SEM-BSE montage image of the surface of the 15%CF Alloy 600TT heat NX6106XK-11 specimen IN274 in which SCC initiation was detected by DPCD at 820 hours of exposure at yield stress. Obvious cracks are highlighted in red.

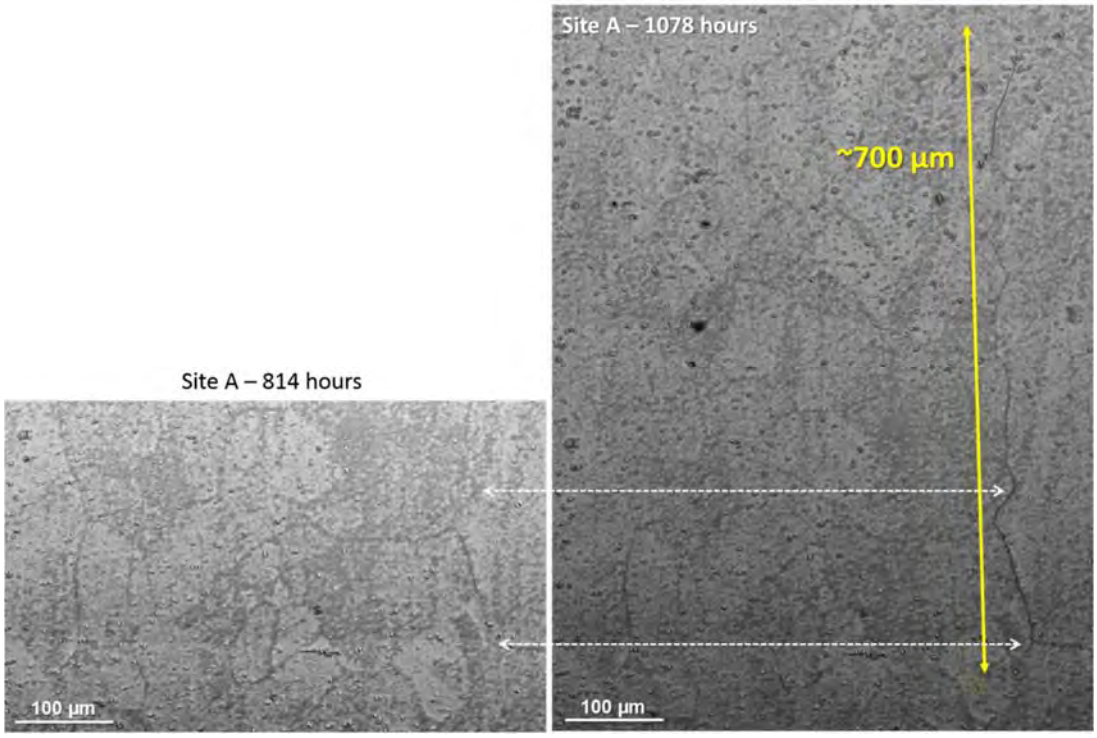

Figure 71. Zoom-in SEM-BSE images on the mid- and post-test crack morphology of IN274 at Site A as highlighted in Figure 70.

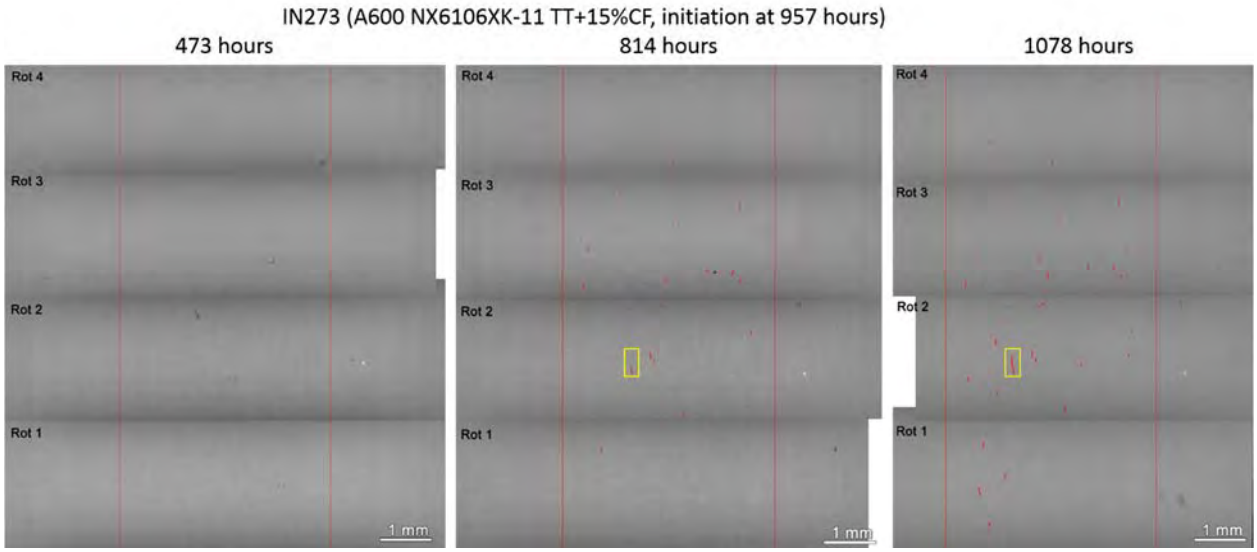

Figure 72. Mid- and post-test SEM-BSE montage image of the surface of the 15%CF Alloy 600TT heat NX6106XK-11 specimen IN273 in which SCC initiation was detected by DPCD at 957 hours of exposure. Obvious cracks are highlighted in red.

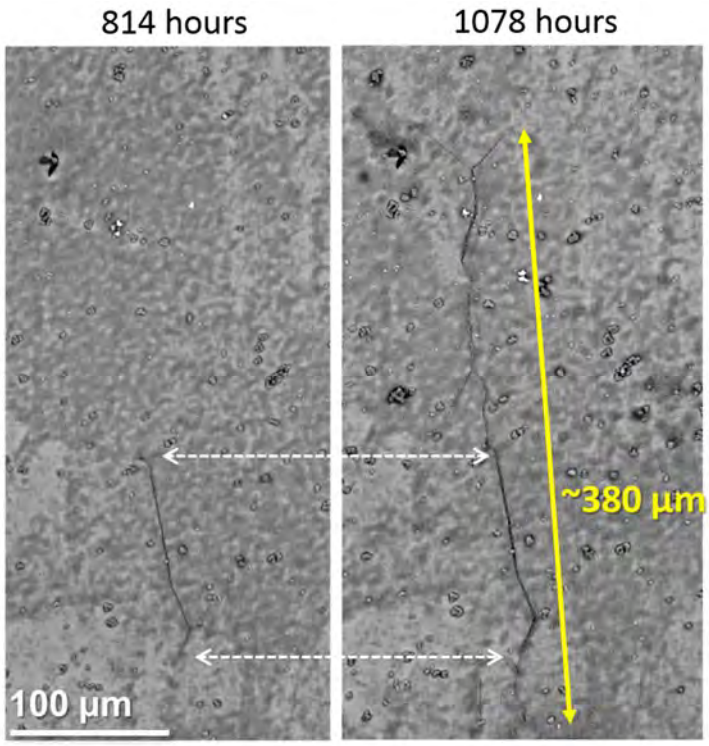

Figure 73. Zoom-in SEM-BSE images on the mid- and post-test crack morphology of IN273 in the area highlighted in Figure 72.

Discussion

The difference in the morphology of IGA in the absence/presence of GB carbides have been clearly captured by SEM/TEM examinations. Upon encountering a GB carbide, IGA always bifurcates and circumvents along the carbide/metal interface before the two ends rejoin and continue to move forward down the GB. Interestingly, the carbides that are reached by IGA usually could not preserve their original ellipsoidal shape but appear to be eaten away by exhibiting a thin Ni-rich/Cr-depleted layer between the IGA and the Cr-rich core with rough, serrated edges. These characteristics are indicators of enhanced local corrosion/oxidation around carbides, but they do not seem to have slowed down IGA penetration into the material. As shown in Figure 47, the IGA depth and its evolution over time does not reveal any statistically significant difference between the MA, SA, and SA+TT 15%CF Alloy 600 materials in both stressed and unstressed conditions. Instead, applied stress appears to exert a predominant role over GB microstructure in IGA growth. This is also illustrated in Figure 47, where the stress-assisted IGA in SCC initiation specimens loaded at yield stress exhibit an average depth twice as deep as the IGA in the unstressed exposure coupons after 1000 hours of exposure, which kept increasing with the increase in exposure time whereas little growth was observed in the IGA without stress. In addition, quantification on the short IG cracks in the SA and SA+TT 15%CF specimens revealed a much slower increase in the percentage of cracked GBs over the total amount of observed GBs after the first test interruption at ~480 hours (Figures 45 and 46), which coincides with the exhaustion of primary stage creep as indicated in the DCPD referenced strain evolution in Figures 57 and 63. This finding seems to agree with a study by Parkins et al. [22], where they demonstrated in constant load tests that a sufficiently fast creep strain rate is necessary for cracking to take place given favorable electrochemical conditions.

The comparison on practical SCC initiation behavior between MA, SA, and SA+TT 15%CF Alloy 600 materials suggest that GB microstructure may have modified SCC initiation behavior as a result of thermal history. The much longer SCC initiation times and the more gradual increase in the DCPD referenced strain in the SA and SA+TT 15%CF specimens indicate an improved resistance to short crack growth in these two conditions over the MA condition. However, little difference in the SCC initiation behavior was observed between the SA+ and SA+TT 15%CF materials in terms of SCC initiation time and SCC initiation morphology. In fact, the TT+15%CF specimens even exhibited slightly shorter SCC initiation times (500-960 hours) in comparison to the SA+15%CF specimens (800-1100 hours), but the trend is likely to be convoluted by different magnitudes of stress applied during test on these two types of specimens. As shown in Figure 74, the TT+15%CF specimens were loaded at a yield stress ~12% higher than that of the SA+15%CF specimens. Since cracking and short crack growth under constant load should require a competition between the destabilization of the protective film by creep and its recovery by a repassivation process, an attempt was made to correlate steady state creep stain rate to SCC initiation time with result presented in Figure 75. The steady state creep strain rate for each specimen was preliminary obtained from the relatively flat portion in the DCPD referenced strain before indication of SCC initiation occurred. While existing IGA

and short cracks may lead to variation in evolution of DCPD referenced strain, their impact was considered negligible based on similar IGA depth and crack evolution revealed by statistical analysis and SEM observations. Nevertheless, it should be recognized that the strain rate shown in this plot is more qualitative than quantitative, but the trend revealed between different material conditions should be appropriate. The results showed a good inverse-linear correlation between bulk steady state creep strain and SCC initiation times across different GB microstructures, where longer SCC initiation times were observed in specimens exhibiting slower macroscopic creep strain rate. This again indicates an important role of creep in the events leading to SCC initiation, but more detailed investigation is needed to evaluate the relationship between macroscopic creep and GB creep, as well as local chemistry at GBs to provide a more comprehensive understanding on the synergistic effects of mechanical factors and GB microstructure on SCC initiation in CW Alloy 600.

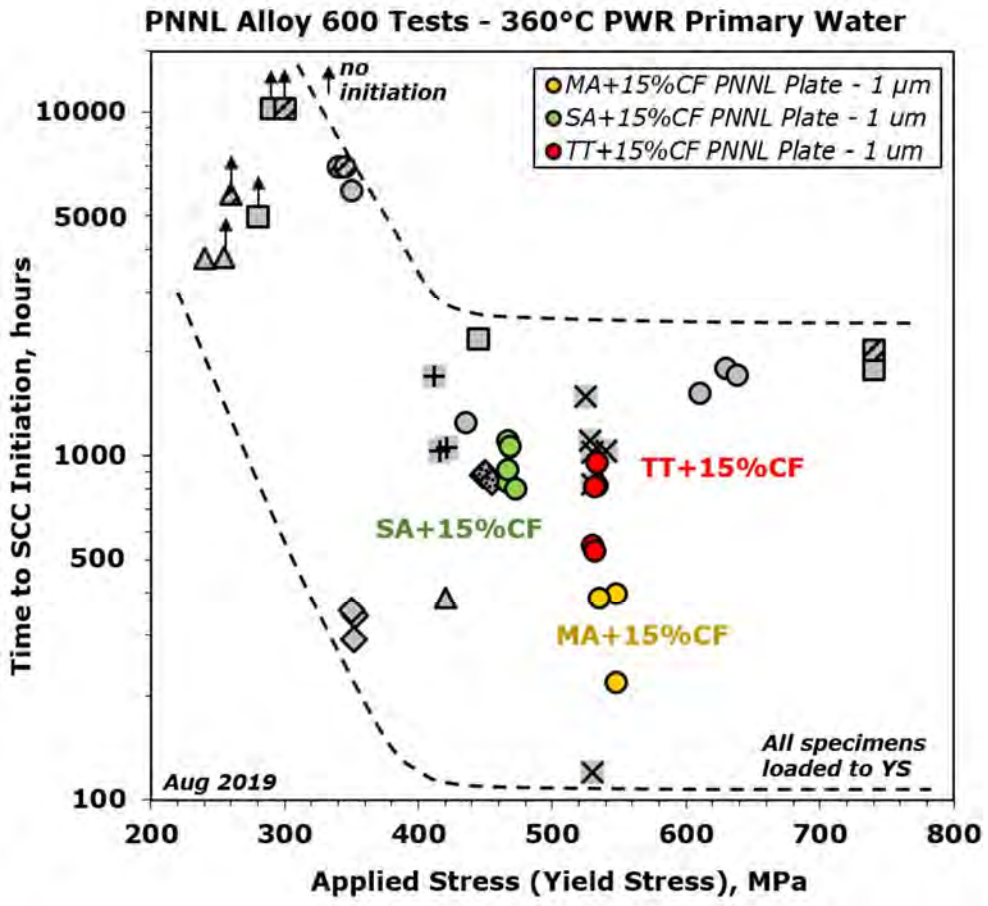

Figure 74. SCC initiation time as a function of applied stress for CW Alloy 600 materials tested at yield stress in 360ºC simulated PWR primary water highlighted with the three material conditions investigated in this study.

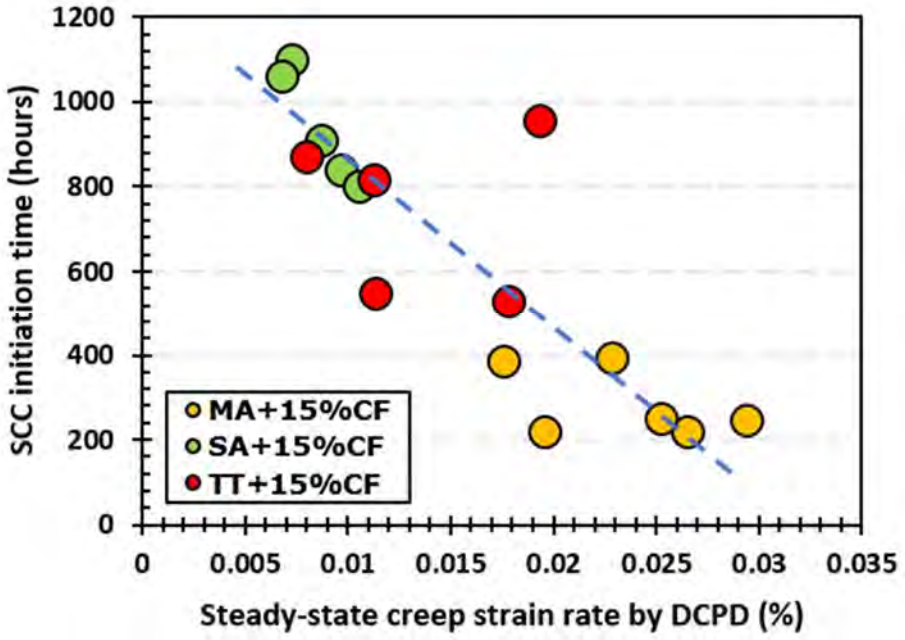

Figure 75. Correlation between SCC initiation time and steady state creep strain rate indicated by DCPD referenced strain rates for the MA, SA, and SA+TT 15%CF Alloy 600 heat NX6106XK-11 materials.

Evaluation of Grain Boundary Microstructure Effects on SCC Initiation in Alloy 690

While the SCC initiation research on Alloy 600 in simulated PWR primary water has demonstrated that IGA is the precursor to SCC initiation in this material [5, 7, 18], an equivalent degradation and cracking process does not occur in Alloy 690. Due to a much higher Cr content in alloy composition, a compact chromia layer readily forms above GBs intersecting the surface when exposed to high-temperature water and remains protective after long term exposure at high stresses. As a result, CW Alloy 690 is more resistant to IGA and SCC initiation. However, recent experimental studies at the Institute of Nuclear System Safety in Japan and PNNL have revealed an alternate mechanism of crack initiation in this material through formation and growth of GB creep cavities [16, 23-27]. To better understand the evolution of GB cavities and predict degradation of Alloy 690 in realistic PWR operating conditions, systematic long-term SCC initiation testing is being performed at PNNL to evaluate factors influencing GB cavity formation and growth in seven commercial Alloy 690 heats. To date, the test consists of three phases with each lasted for about 1.1 year. The research first started with three Alloy 690TT CRDM heats and three TT/MA plate/bar heats that exhibited moderate-to-high SCC crack growth rates in the highly CW condition. These materials are being tested for SCC initiation response in 360°C simulated PWR primary water at various cold work levels from 12 to 32%. The test matrix was expanded during Phases II and III to include more variations in GB carbide distribution (TT vs. SA), applied stress (100% YS versus 90% YS), heat IGSCC susceptibility in the highly CW condition and one high-purity Ni-30Cr heat. Figure 76 shows the SCC CGR obtained by our NRC crack growth rate project [28, 29] highlighting the materials chosen for SCC initiation testing. A summary of the materials that have been tested at the three phases is provided in Figure 77 with their corresponding exposure time at each phase.

SEM characterizations of surface damage were carried out at every test interruption. Qualitative results on cavity distribution in all tested material conditions after Phase I and II exposures have been reported in several previous LWRS milestone reports [19, 30], which revealed that GB cavity formation and growth is directly controlled by starting microstructure, degree of cold work, and applied stress. This report narrows down the scope to four Alloy 690TT heats for a more detailed study on the GB microstructure effects. It will review the key findings from previous exposures with additional analytical high-resolution microscopy and quantitative analyses. An update will also be given on the ongoing characterization after Phase III exposure on these heats highlighting the GB microstructure effects on cavity evolution and crack initiation in CW Alloy 690.

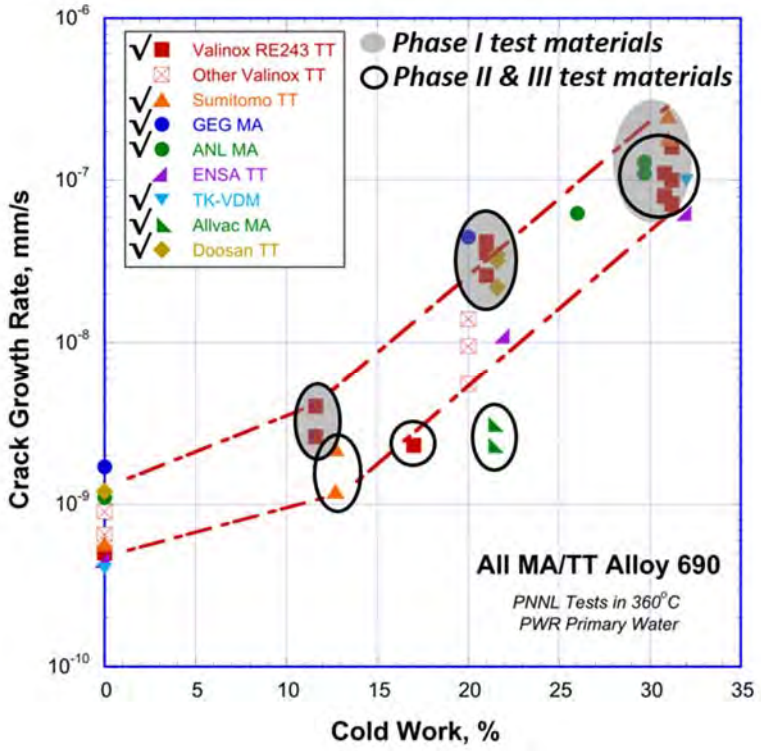

Figure 76. SCC CGR response of TT/MA Alloy 690 materials obtained at PNNL through a Nuclear Regulatory Commission (NRC) project [28, 29]. The heats and cold work levels selected for SCC initiation evaluation at each stage were checked in the label box and circled in the plots, respectively.

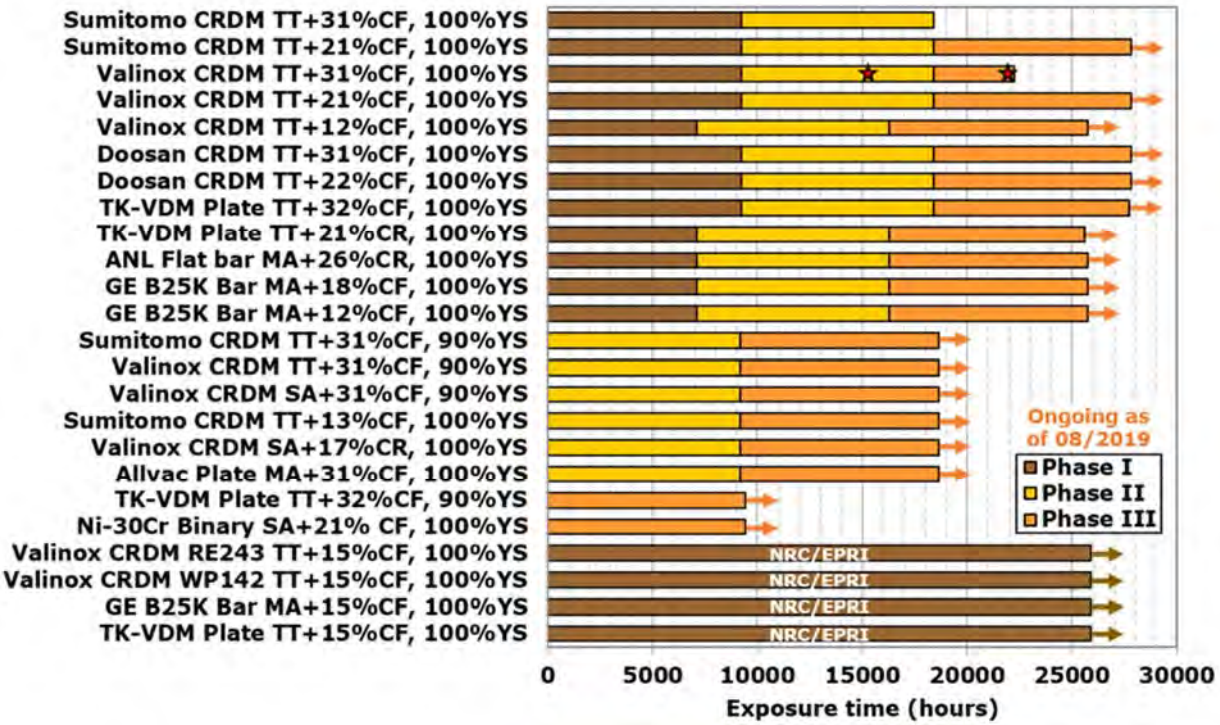

Figure 77. Exposure time of the CW Alloy 690 materials evaluated at Phases I, II, and III of the SCC initiation testing.

For each combination of heat and cold work condition, three SCC initiation specimens were prepared with one polished to a 1 μm surface condition and the other two a ground finish on the gauge emulating surface damage condition of in-service LWR components [20]. Due to a limited number of holes in the feed through connector for wire passage, originally only the highly polished specimen from each combination of heat and cold work condition was instrumented by DCPD, and resistivity drift was not monitored as we normally do for specimens tested in smaller autoclaves. If the highly polished specimen was removed from the test later on, then a specimen with a ground surface finish from the same material and cold work condition would be monitored instead. Information of the specimens reported in this study is summarized in Table 4.

Table 4. Summary of material condition and test status of the Alloy 690 initiation specimens reported in this paper.

Specimen	Material Condition	Surface Condition	Applied Stress*, MPa	Exposure time, hours		
				Phase I	Phase II	Phase III
IN024□	Sumitomo CRDM TT + 21%CF	1 μm	585	9,220	9,180	9,440
IN025■		Ground	590	9,220	9,180	N/A
IN027□	Valinox CRDM TT + 21%CF	1 μm	525	9,220	9,180	9,440
IN028■		Ground	525	9,220	9,180	N/A
IN030□	Doosan CRDM TT + 21.6%CF	1 μm	545	9,220	9,180	9,440
IN031■		Ground	555	9,220	9,180	N/A
IN059□	TK-VDM Plate TT + 21%CR	1 μm	655	7,110	9,180	9,440
IN060		1 μm	675	7,110	9,180	9,440
IN035□■	Sumitomo CRDM TT + 31%CF	Ground	675	9,220	9,180	N/A
IN036□	Valinox CRDM TT + 31%CF	1 μm	700	9,220	9,180	9,440
IN037□■		Ground	690	9,220	9,180	N/A
IN039□	Doosan CRDM TT + 31%CF	1 μm	665	9,220	9,180	9,440
IN040□■		Ground	655	9,220	9,180	N/A
IN042□	TK-VDM Plate TT + 31.9%CF	1 μm	665	9,220	9,180	9,440
IN043□■		Ground	675	9,220	9,180	N/A

* The applied stress is the yield stress of the specimens at test temperature (360°C).
□ Specimens instrumented using DCPD during Phase II and Phase III.
■ Specimens removed after Phase II for destructive cross-section examination.

Materials and Pre-Test Microstructure

This report focuses on three Alloy 690 CRDM heats and one plate heat all in the TT condition. The chemical composition and thermal treatment history for each heat are listed in Table 5. Prior to testing, the materials were either cold-forged (CF) or cold-rolled (CR) to produce a cold work level ranging from 12 to 32%. Most combinations of these material and cold work condition had already been evaluated for SCC crack growth behavior as noted earlier, where these four heats in the 20-32%CW condition all exhibited moderate-to-high SCC crack growth rates. Pre-testing microstructures were

characterized for these materials in both the as-received and CW conditions. While all exhibit a semi-continuous GB carbide coverage, significant heat-to-heat variability was observed in the size and spacing between carbides. As summarized in Table 6, the TT CRDM tubing heats Sumitomo E67074C and Valinox RE243 feature the most uniform and closely spaced small carbides, while the TT plate heat TK-VDM 114092 exhibits small carbides at similar size but with a slightly larger spacing. The TT CRDM bar heat Doosan 133454 has much larger IG carbides that are more widely spaced.

Table 5. Composition and heat treatment for the Alloy 690 CRDM/plate heats studied in this report.

Heat	Composition (wt%)	Heat treatments
Valinox RE243 CRDM Tube 2360	Ni-28.9Cr-10.4Fe-0.02C-0.3Mn-0.35Si-0.14Al-0.23Ti-0.024N-0.008P-0.0005S	1122°C/~1 min/ water quench (WQ) + 716-725°C/10.5h /air cool (AC)
Sumitomo E67074C CRDM Tube	Ni-29.8Cr-9.8Fe-0.02C-0.29Mn-0.23Si-0.03Cu-0.0002S	Anneal + 725°C/10h/AC
TK-VDM (Doosan) 133454 CRDM Bar	Ni-29.1Cr-8.9Fe-0.020C-0.26Mn-0.29Si-0.26Al-0.32Ti-0.01Cu-0.02N-0.005P-<0.002S-0.002B	1045°C/4 hr/WQ +720°C/10h/AC
TK-VDM 114092 Plate	Ni-29.5Cr-9.5Fe-0.020C-0.25Mn-0.26Si-0.32Al-0.36Ti-<0.01Cu-0.003P-<0.002S	1030°C/1 hr/WQ +715°C/10hr/AC

Table 6. Summary of grain size and carbide distributions for the four Alloy 690TT heats.

Material	Grain size (μm)	IG carbide size	GB carbide spacing
Valinox RE243 TT	~90	50–200 nm	~0.1 μm
Doosan 133454 TT	~90	1–5 μm	~0.5–2 μm
Sumitomo E67074C TT	~35-40	50–300 nm	~0.1 μm
TK-VDM 114092 TT	~35-40	50-200 nm	~0.1–0.5 μm

It is important to note that permanent damage was identified in all CW materials. This damage was present at GBs as nano-to-micrometer size cavities and small, cracked precipitates, both of which increased in density as cold work level increased. An example is provided in Figure 78, where the two different types of damage are highlighted in the Doosan CRDM material in the TT+31%CF condition. Smaller voids (on the order of 10s of nanometers) are also observed at the carbide/matrix interface. The distinction of cracked carbides as compared to cavity formation between two adjacent IG carbides can at times be difficult to discern, but often the shape and size of the carbide is utilized to determine whether the carbide has cracked. In most cases where carbide cracking occurs, cavity formation into the matrix is also present. The appearance of cavity formation into the adjacent matrix is important because a second type of cavity formation is often observed, denoted by the appearance of the adjacent matrix grains puckering into the cavity. The appearance of cavity formation into the grain as compared to matrix moving into the cavity has yet to be assigned strictly to cracked carbides versus adjacent carbides sliding to cause voids, but it is important to delineate the two types. Again, if low kV imaging is not utilized it can become difficult to discern between these types because the interaction volume can

convolute imaging. The adjacent matrix strain in proximity to GB damage is also an important microstructural feature to be noted using low kV imaging. The appearance of matrix shear bands is almost always associated with cracked carbides and cavities, providing insights into how GB damage occurs in these materials. At higher levels of damage, these bands are most often present.

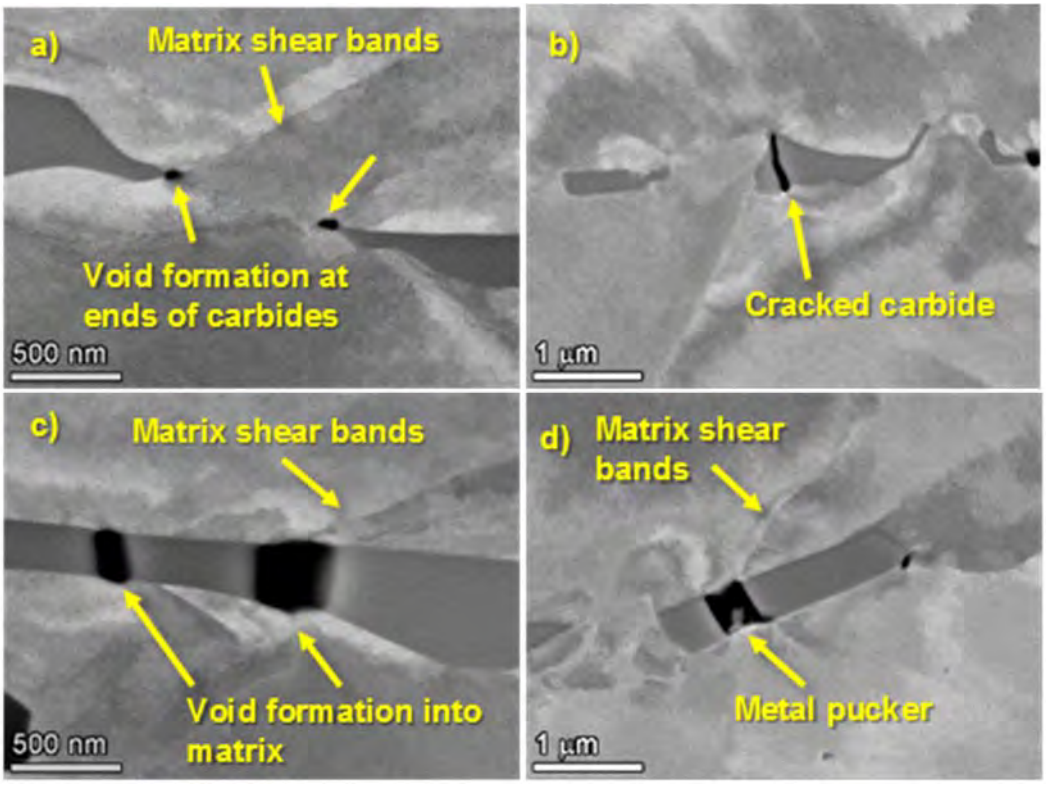

Figure 78. High resolution SEM-BSE images of various types of grain boundary damage (voids/cracks) in the TT+31%CF Alloy 690 Doosan CRDM heat which can serve as fingerprints in initiation tests.

As shown in Figure 12, there is possibility of cracked carbide fallout during sample preparation, but the observation in pre-test CW materials is extremely low. In order to demonstrate the minimal effects of high quality metallographic polishing on cracked carbides, a larger IG carbide on the order of a micrometer was observed (Figure 79) containing a partial crack through the middle of the carbide. The extent of the cracking was not only noted by the dark crack, but as well the bright contrast ahead of the crack. This contrast is most likely a change in orientation due to strain ahead of the open crack. Additionally, matrix shear bands are observed emanating from the crack. If this level of observable damage within a large carbide did not result in carbide fallout, it is unlikely that smaller carbides and other damaged microstructures would exhibit fallout during sample preparation.

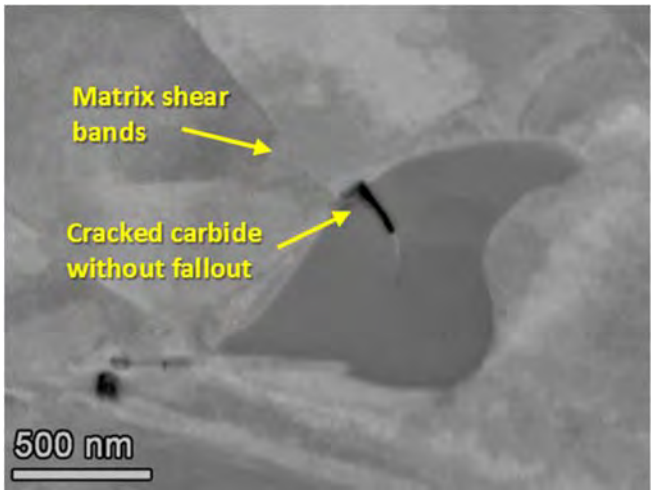

Figure 79. SEM-BSE image illustrating the type of damage that can be observed in larger carbides without grain fallout during sample preparation.

It is also revealed that the size and density of permanent damage induced by cold work has a strong dependence on GB microstructure. An example is shown in Figure 80, where the permanent damage induced by cold work in the 31%CF Alloy 690TT Valinox and Doosan CRDM materials are highlighted. The images are shown at the same scale providing a direct comparison of the size and distribution of cavities and cracks. Apparently, the materials exhibiting fine carbides at GBs often feature small voids at a higher density on certain boundaries, whereas the damage in the materials having larger and more widely spaced carbides are also larger and more spaced out.

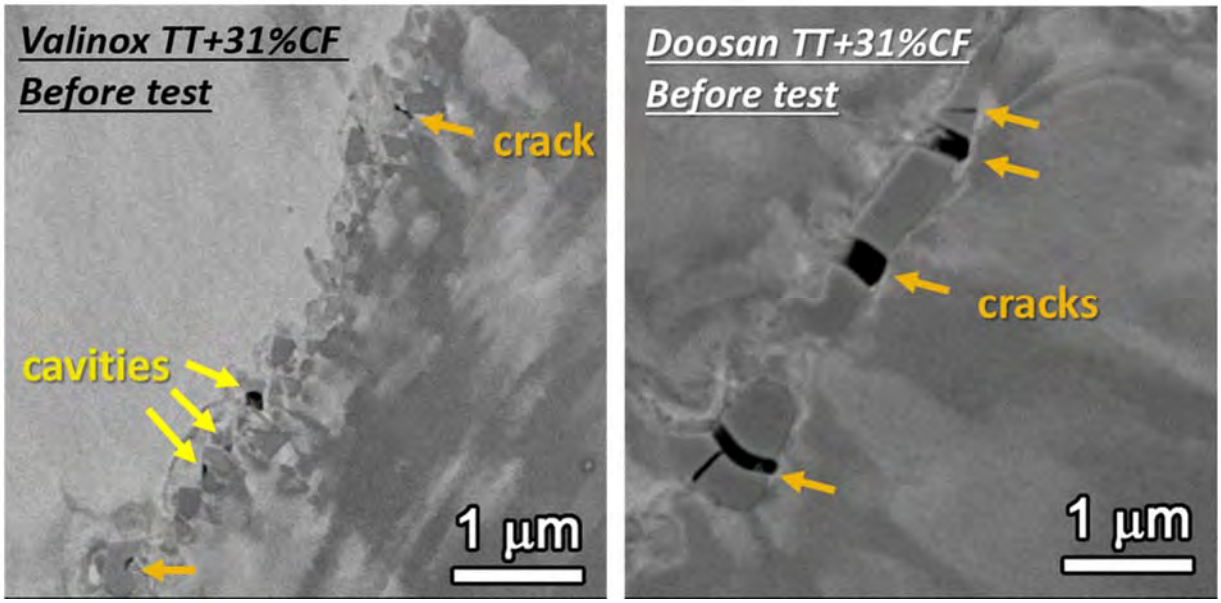

Figure 80. SEM-BSE image shown in the scale illustrating the permanent damage (highlighted by arrows) induced by cold work in the 31%CF Alloy 690TT Valinox and Doosan CRDM materials.

DCPD Response

The DCPD signal is sensitive not only to cracking but also to changes in length and diameter due to creep or tensile straining, as well as to resistivity changes that occur in Alloy 690 when exposed at PWR relevant temperatures [7]. In this test, DCPD values are presented as strain measurements because up to the point of significant crack formation, creep deformation is believed to more strongly affect the DCPD signal than cracking. It also should be noted that resistivity changes affect the DPCD signal (particularly early in the test) and create a higher strain rate than due to creep alone. During Phase I exposure, all instrumented specimens exhibited a decreasing trend over time in the non-referenced DCPD strain rate response that is likely due to an exhaustion of primary stage creep and a slowing resistivity evolution since material changes saturate after long exposures at 360°C. This trend continued in Phase II for all specimens except IN037, a TT+31%CF Valinox CRDM specimen, which exhibited an obvious upturn at ~15,400 hours of exposure that kept increasing during the remainder of the test, suggesting practical crack initiation has taken place in this specimen (Figure 81). The test was stopped after the specimens continued from Phase I testing reached a total exposure time of ~18,400 hours and the replacement specimens reached a total exposure of 9,180 hours at target load, similar to the exposure time reached during the Phase I testing for most specimens (9,220 hours). In addition, another TT+31%CF specimen IN036 from the same Valinox CRDM heat tested in a small autoclave system showed a strain jump at 22,180 hours of exposure followed by increased strain rate (Figure 82), again suggesting crack initiation. In order to confirm this behavior, the test was interrupted at ~22,250 hours and IN036 was removed for SEM examination.

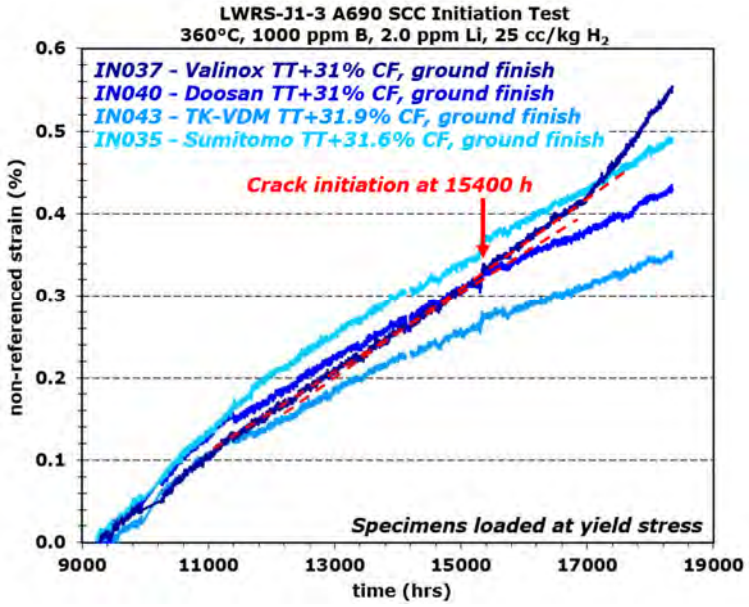

Figure 81. DCPD non-referenced strain response for the instrumented specimens from the four TT+31% CF Alloy 690 during the entire Phase II testing period. Crack initiation is indicated for the Valinox CRDM specimen IN037.

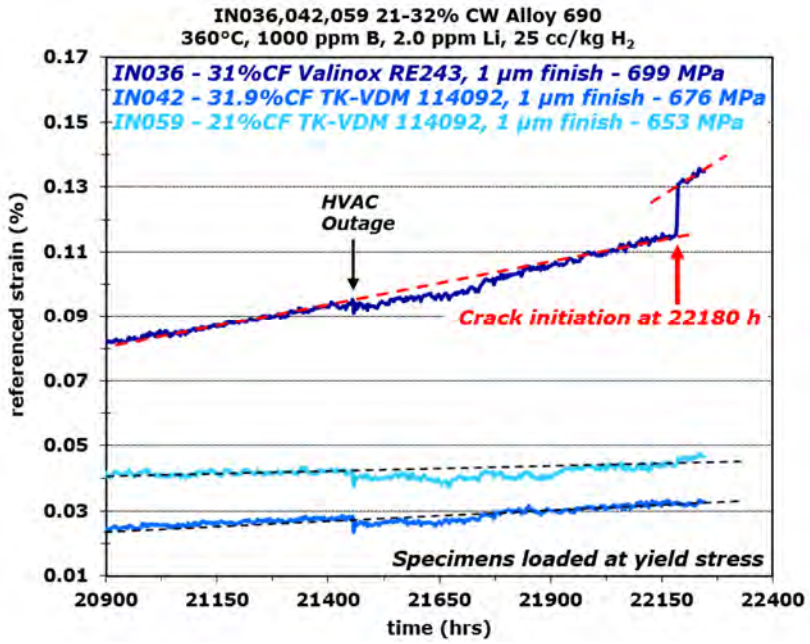

Figure 82. DCPD non-referenced strain response for the instrumented TT+31% CF Alloy 690 specimens during the end of the Phase II testing period. Crack initiation is indicated for the Valinox CRDM specimen IN036.

GB Damage Evolution on the Surface

Evolution of gauge surface morphology of highly polished specimens IN036 (TT+31%CF Valinox CRDM), IN039 (TT+31%CF Doosan CRDM) and IN042 (TT+31%CF TK-VDM Plate) after Phase I and Phase II exposure are presented in Figures 83-85, respectively. As reported previously, IG damage was identified in all highly polished TT+31%CF specimens after Phase I, which include obvious cracks with identifiable openings on the surface (highlighted in red) and possible cracks with continuous darker contrast along GBs (highlighted in green) [16]. After the additional ~9,180 hours of exposure during Phase II, most cracks in these specimens exhibited little growth on the surface. No apparent extension in length nor widening of crack opening were observed for existing obvious cracks. Instead, new short cracks had either grown from previously identified possible cracks or were formed along different GBs, resulting in a slight increase in overall crack density.

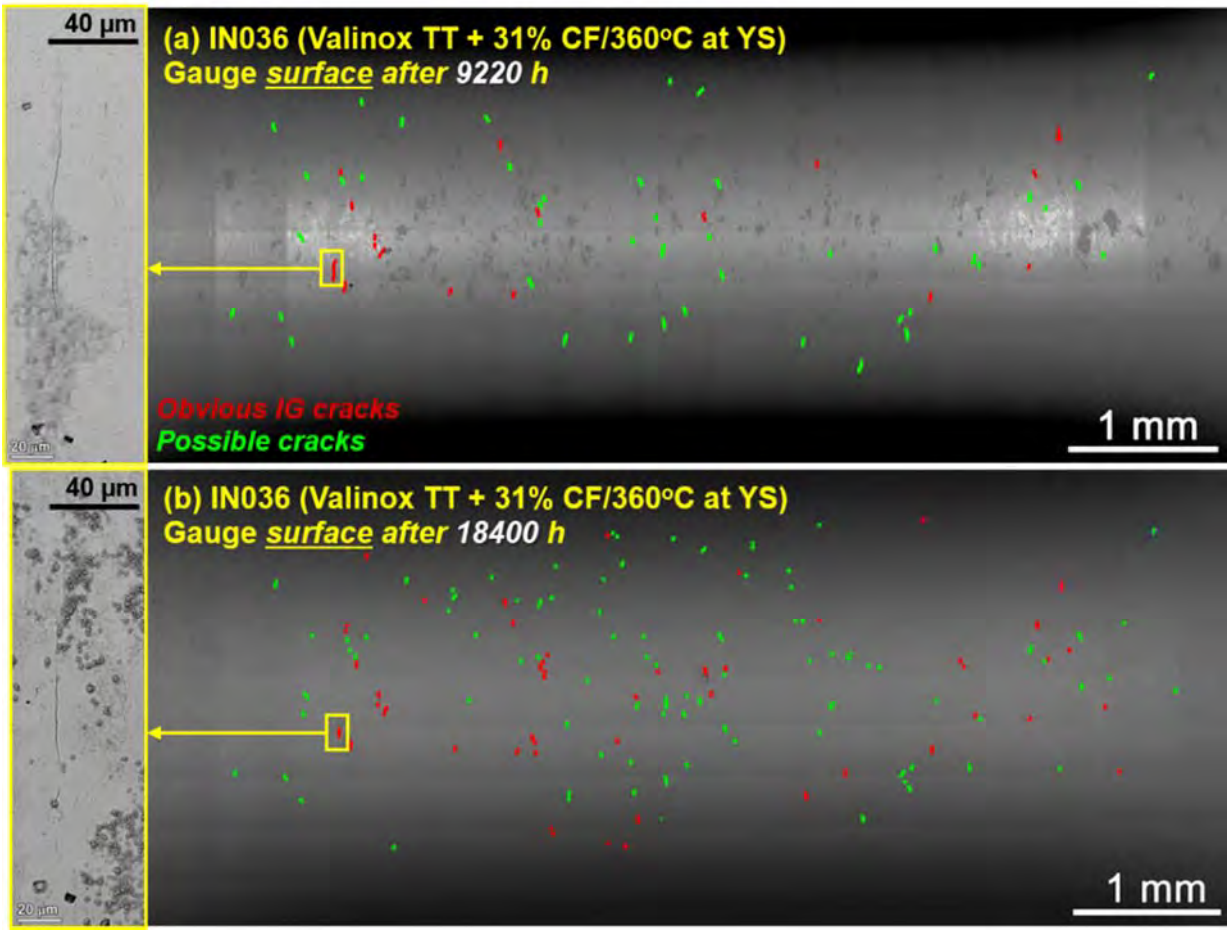

Figure 83. SEM-BSE montage images of the gauge surface in one rotation of the 1 µm finish, TT+31%CF Alloy 690 Valinox CRDM specimen IN036 after (a) Phase I and (b) Phase II exposure.

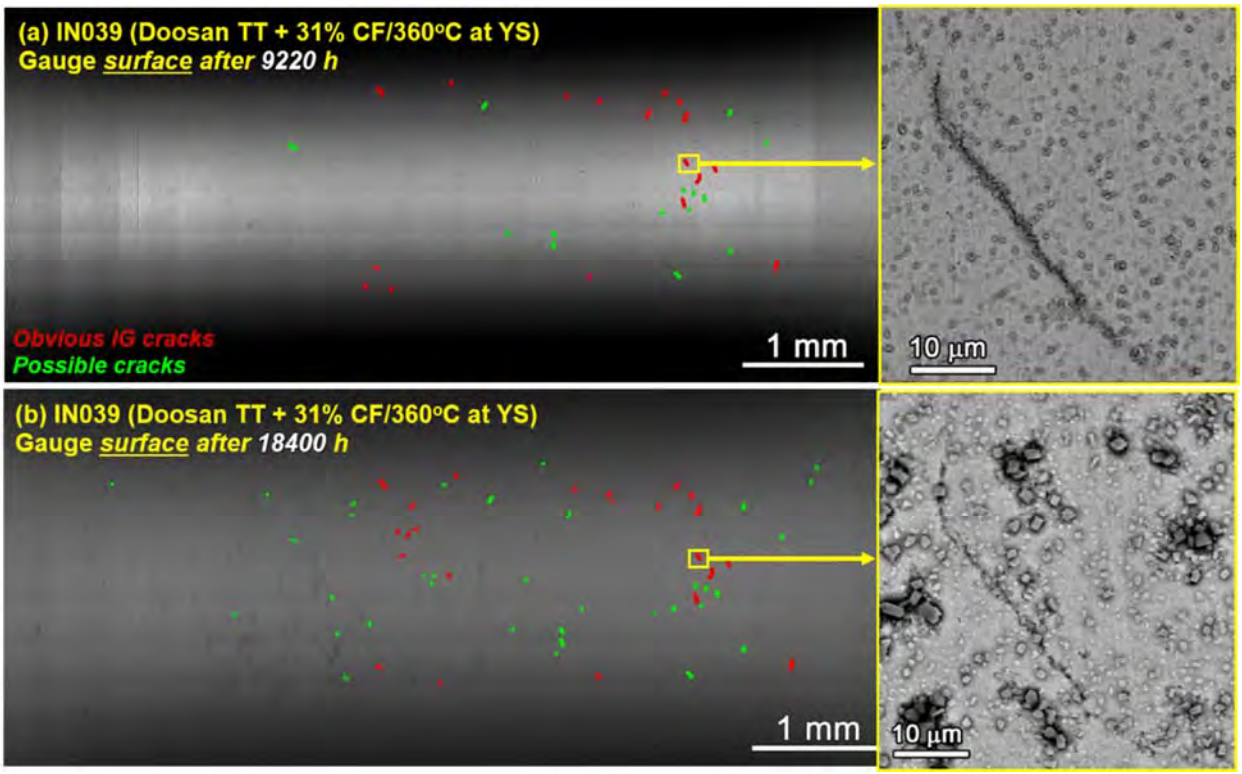

Figure 84. SEM-BSE montage images of the gauge surface in one rotation of the 1 µm finish, TT+31%CF Alloy 690 Doosan CRDM specimen IN039 after (a) Phase I and (b) Phase II exposure.

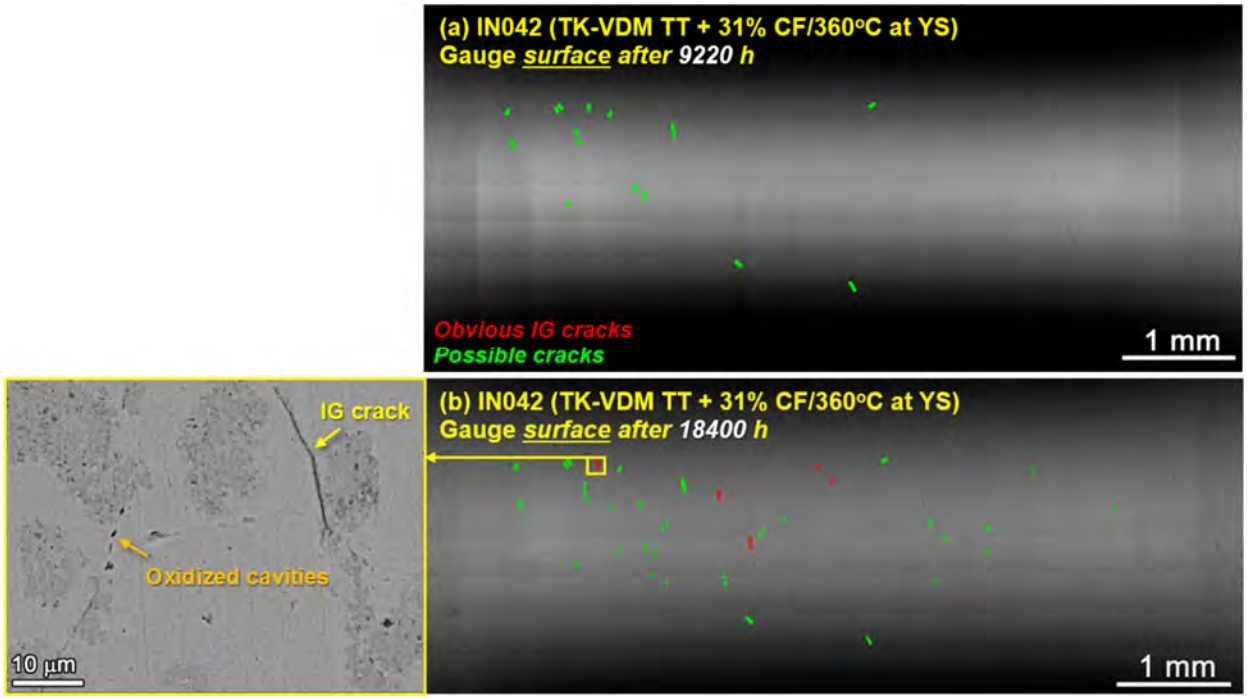

Figure 85. SEM-BSE montage images of the gauge surface in one rotation of the 1 µm finish, TT+31%CF Alloy 690 TK-VDM plate specimen IN042 after (a) Phase I and (b) Phase II exposure.

GB Damage Evolution in the Cross-Section

The damage evolution in highly CW specimens from each material assessed in this section by comparing the overall GB cavity aggregation distribution in the entire gauge section and the morphology of the highlighted GB cavity aggregations at higher magnifications. Three colors were used to highlight the different types of GB cavity aggregations in the SEM-BSE montage images: yellow represents aggregations of closely spaced but disconnected GB cavities, orange represents aggregations with partially connected (<50%) GB cavities, and red represents fully connected GB cavity aggregations forming longer IG cracks. Sporadically distributed, more discrete cavities are not marked in these montage images.

Presented first is the TT+31% CF Doosan CRDM material featuring well-spaced, large carbides at high-energy GBs (Figure 86). Only a slight increase in the cavity aggregations were observed after extended exposure, which is due primarily to growth in size of pre-existing damage produced by cold work rather than formation of new cavities. This is confirmed by higher magnification images, where little change in cavity density and spacing was observed. In previous sections detailing the potential artifacts such as carbide fallout and types of observable grain boundary damage, the Doosan CRDM samples were highlighted having a higher potential for fallout owning to the carbide cracking (Figures 12 and 79). Therefore, it was expected that if carbide fallout were to be an issue in SCC initiation specimens, it would be most apparent in the Doosan material. Figure 87highlights the TT+31%CF Doosan CRDM specimen IN040 in representative regions of very low stress (specimen ends) and high stress (gauge) at low (left) and high (right) magnifications. Grain boundary damage in the low-stress region was observed as typical cracked carbides, cavities in the middle of carbides as well as at the ends of carbides. Strain contrast in the matrix adjacent to the carbides was minimal and, if present, was plumed around the carbides. Two regions in the high-stress gauge region are presented to illustrate the various types of damage induced during creep. In Figure 87c and d, the carbide cracking and cavity formation are similar to that for the low-stress region (Figure 87a and b) with only the appearance of matrix shear bands being present emanating from the carbides. Figure 87f is unique because it shows much larger cavity formation between carbides that could be mischaracterized as carbide fallout if not for the presence of matrix shear bands and metal pucker into the cavities. Compared to the carbide fallout in Figure 12, this appearance is markedly different and suggests these isolated cavities grew due to creep processes during testing at 360°C.

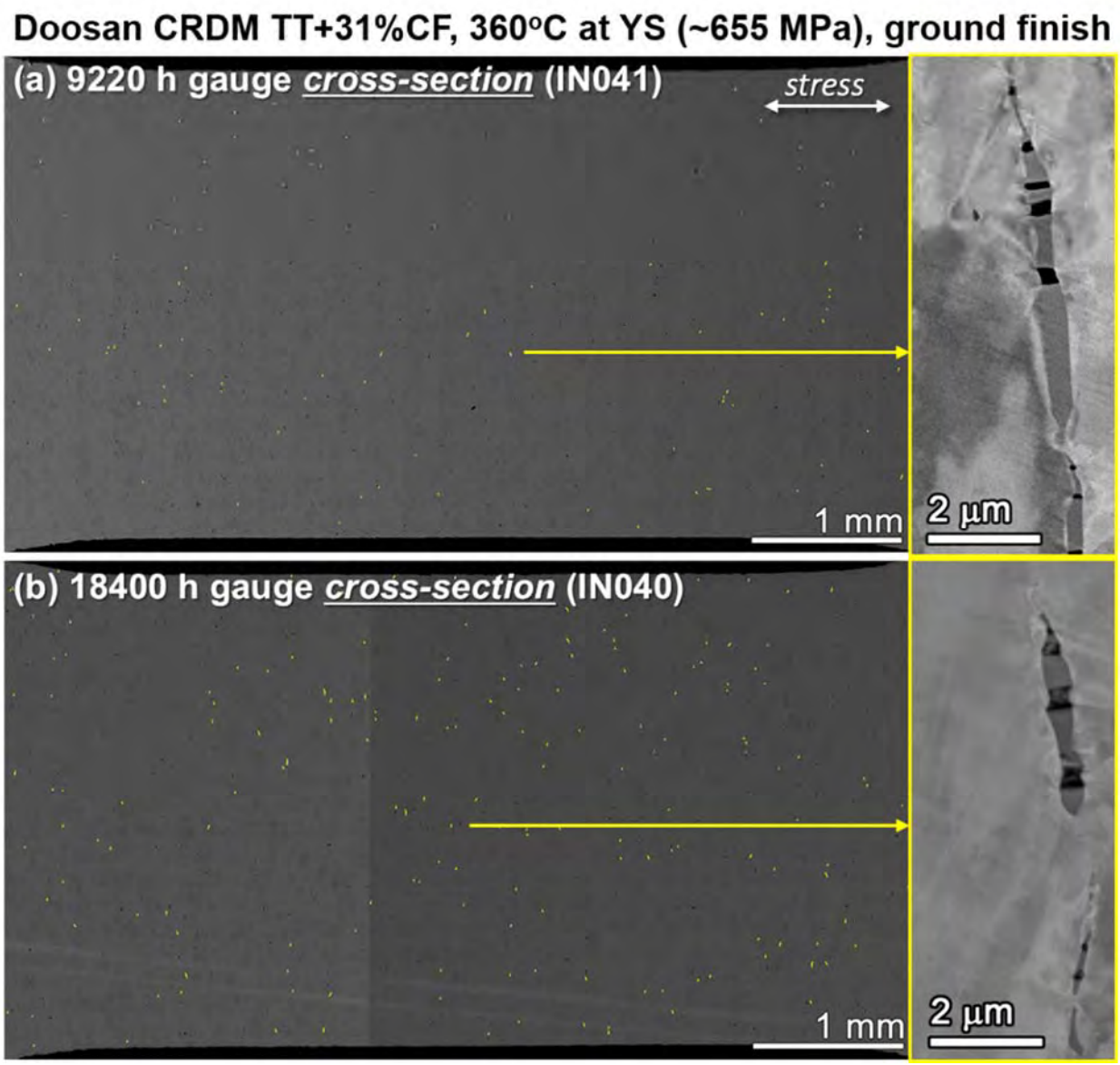

Figure 86. SEM-BSE montage images of the gauge cross-section of the ground finish, TT+31%CF Alloy 690 Doosan CRDM specimens (a) IN041 after Phase I exposure and (b) IN040 after Phase II exposure. Aggregations of closely spaced, disconnected GB cavities are marked in yellow.

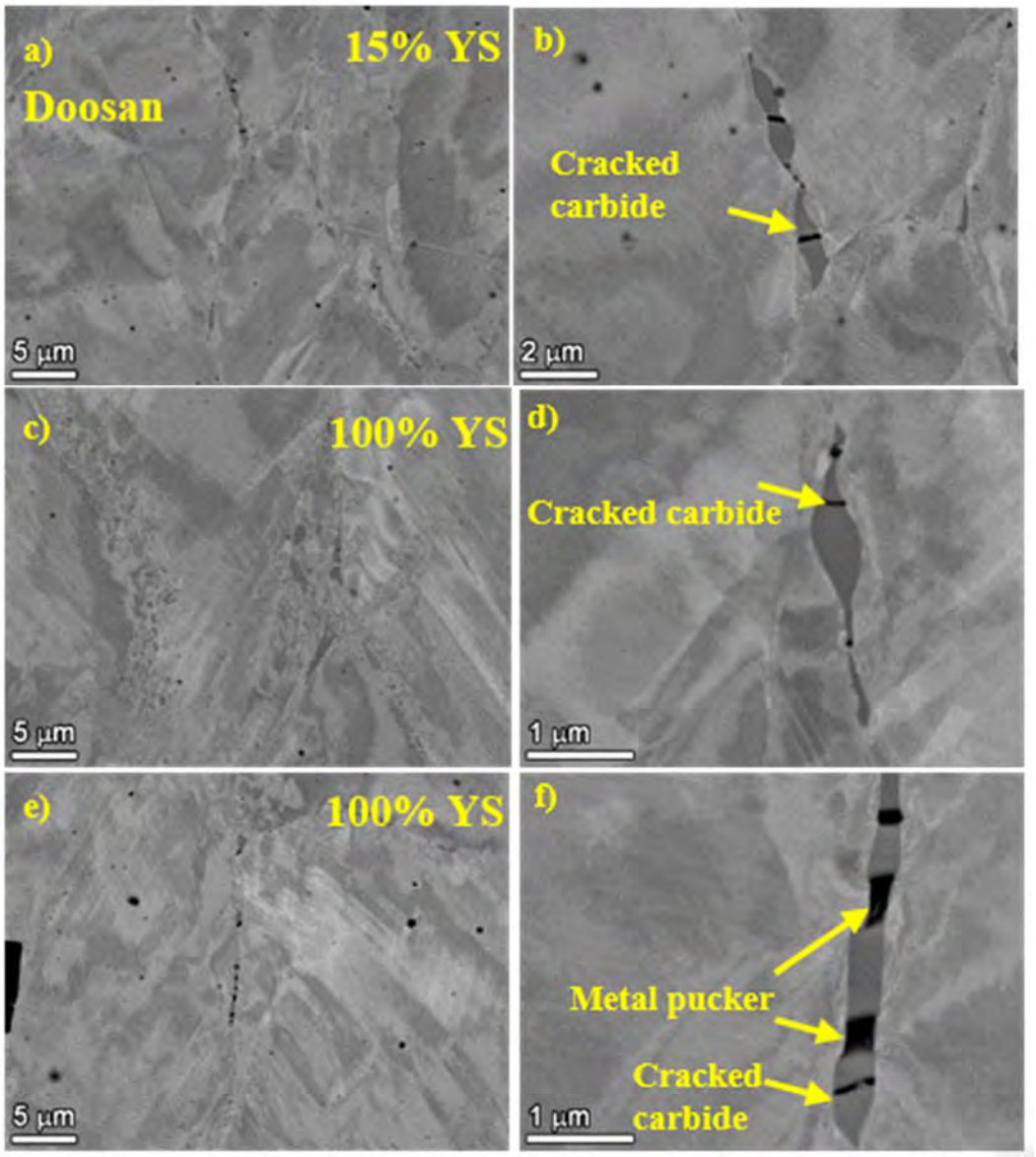

Figure 87. SEM-BSE images of low-stress (a, b) and high-stress (c-f) regions from the TT+31%CF Doosan CRDM SCC initiation specimen IN040 after exposure of 18400 hours in 360°C simulated PWR primary water. Only a slight increase in cavity size was observed with no connected IG cracks.

In the other three Alloy 690 CRDM materials, GB carbides are considerably smaller and follow a semi-continuous distribution, but their spacing varies (Table 6). The TK-VDM plate material features the largest spacing between carbides (200-500 nm) among the three. As shown in Figure 88, a higher density of GB cavity aggregations was evidenced after extended exposure with a noticeable increase in size and density, indicating that new GB cavity formation and growth of existing GB cavities took place during Phase II exposure.

The Sumitomo CRDM material, shown in Figure 26, has a semi-continuous distribution of smaller carbides at high-energy GBs with ~100 nm spacing. The TT+31% CF specimens from

this heat exhibited the highest density of GB cavity aggregations after both Phase I exposure among all highly CW heats and an even higher density of such GB damage after Phase II. A closer examination reveals that although very closely spaced, most GB cavities in the aggregations after Phase I exposure were still discrete (highlighted in yellow). The additional 9,180 hours of exposure during Phase II has led to link-up of some GB cavities, resulting in partially connected segments (usually <10 μm long) along GBs as highlighted in orange in Figure 89b.

The TT+31%CF Valinox CRDM material (Figure 27) exhibits similar GB carbide distribution as the TT+31%CF Sumitomo CRDM material, but has a grain size two to three times larger than that in the latter (Table 6). Compared to the gauge cross-section after Phase I, the GB cavities in some aggregations have fully linked up, resulting in IG cracks of a few hundreds of micrometers in length (Figure 90b). The higher magnification image on the right side of Figure 90b reveals the early stage of creep crack formation where neighboring GB cavities become connected to each other through cracked ligaments along GBs. This is consistent with the DCPD response indicating crack initiation in IN037 at ~15,400 hours (Figure 81). In addition, after careful examination along the entire near surface region of the gauge in this specimen, all GB cavity aggregations remained below the nano-crystalline damage layer induced by grinding during surface preparation. No preexisting surface damage such as gouges have reached the bulk microstructure (Figure 90b). These observations suggest that the upturn in the DCPD strain rate observed in the TT+31%CF Vallinox CRDM specimen IN037 is not due to growth of SCC crack from the gauge surface, but reduction in cross-sectional area induced by formation and growth of multiple internal IG creep cracks.

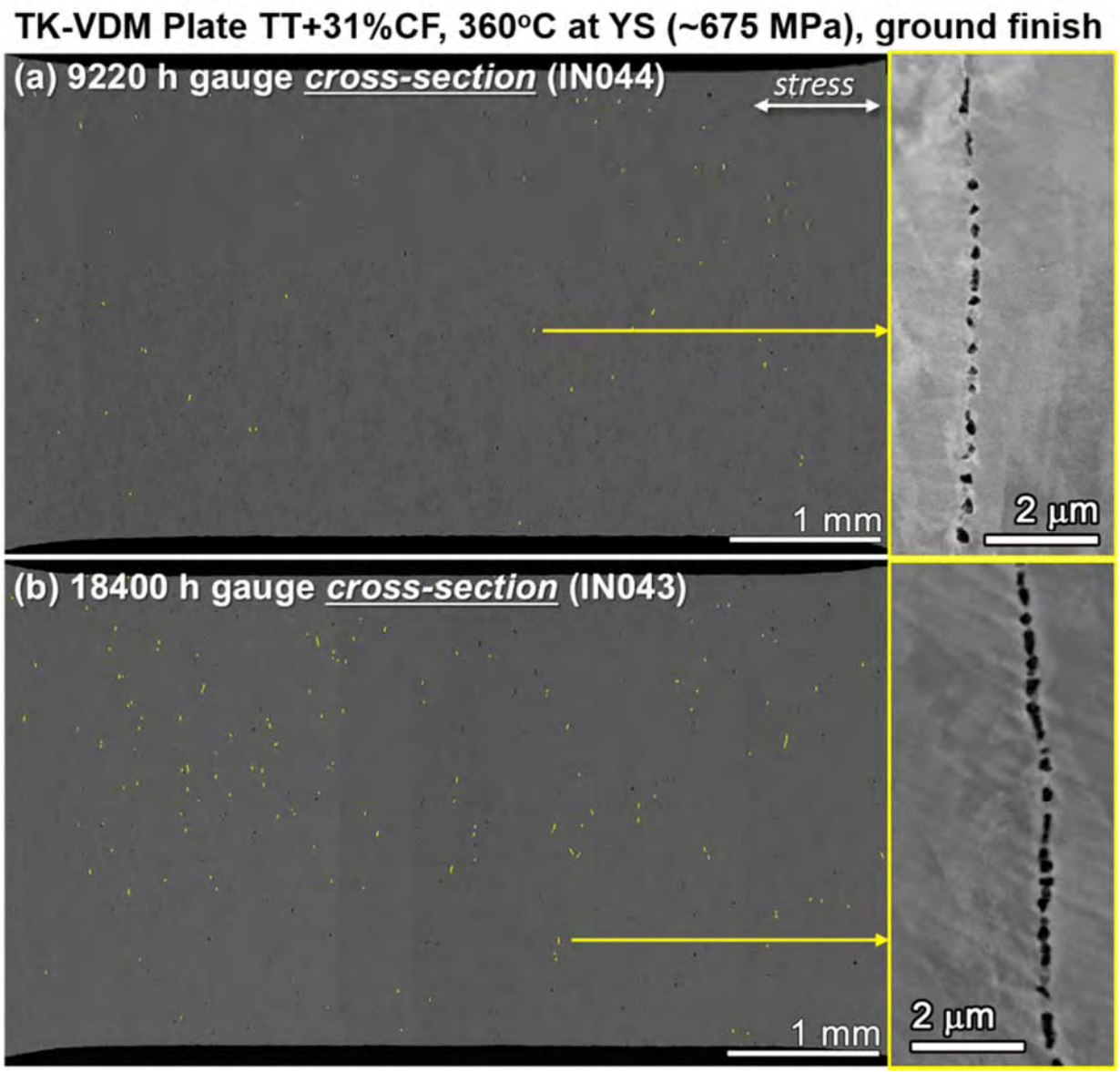

Figure 88. SEM-BSE montage images of the gauge cross-section of the ground finish, TT+31%CF Alloy 690 TK-VDM plate specimens (a) IN044 after Phase I exposure and (b) IN043 after Phase II exposure.

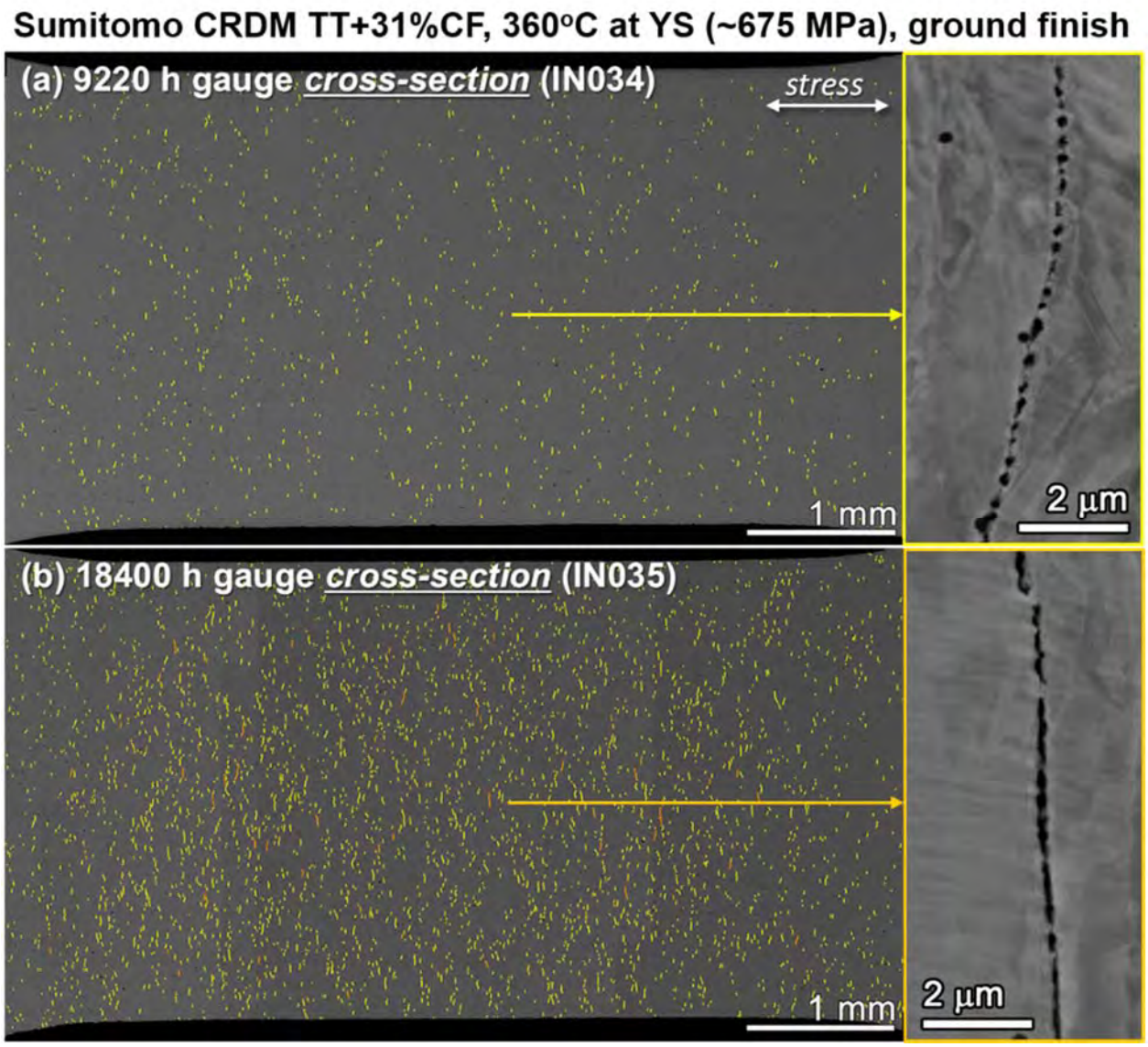

Figure 89. SEM-BSE montage images of the gauge cross-section of the ground finish, TT+31%CF Alloy 690 Sumitomo CRDM specimens (a) IN034 after Phase I exposure and (b) IN035 after Phase II exposure. Aggregations of semi-continuous GB cavities are marked in orange.

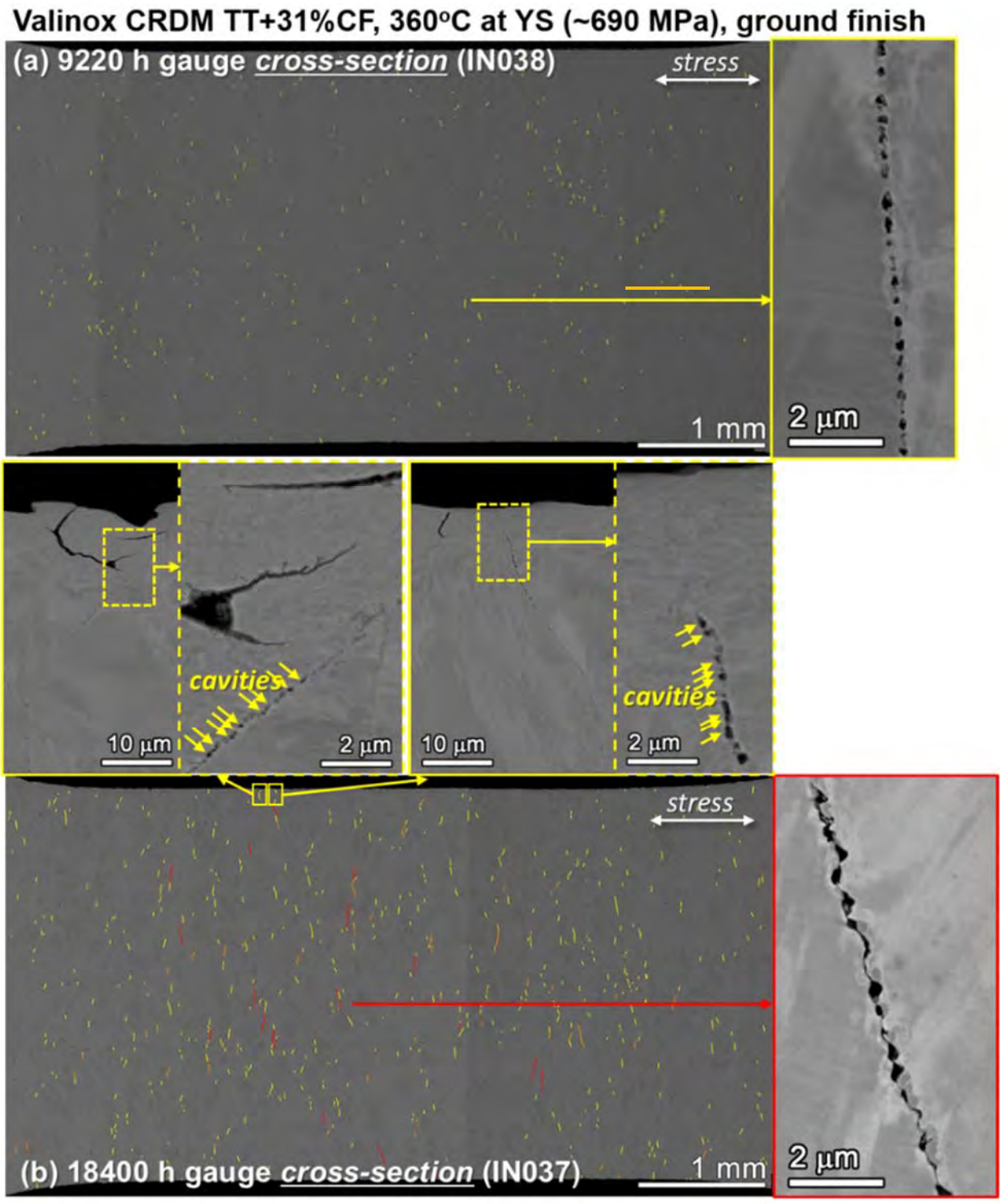

Figure 90. SEM-BSE montage images of the gauge cross-section of the ground finish, TT+31%CF Alloy 690 Valinox CRDM specimens (a) IN038 after Phase I exposure and (b) IN037 after Phase II exposure. IG cracks formed by fully connected GB cavities are highlighted in red.

Figure 91 shows the GB damage in the TT+31%CW Valinox RE243 CRDM specimen IN037 from low stress regions after 18,400 hours of exposure in 360°C simulated PWR primary water. High and low magnifications of two GBs illustrate cavity formation. The density of damage was extremely low in all GB regions, and the strain contrast in the adjacent grains was confined to plumes surrounding the carbides. Cracked carbides were rare in this material and no carbide fallout was observed. A remarkably different damage microstructure was discovered in the high stress gauge section of the same SCC initiation specimen as illustrated in Figure 27b. Examination of the cross-section from the center of specimen (far from the gauge surface) exhibited a nearly continuous distribution of cavities with cracks as long as 100 µm. Two such cracks are presented in Figure 92 not only show open cracks, but more importantly demonstrate an evolution of damage from one end of the crack to the other. Creep crack #1 shows a very low density of GB damage at the bottom of the image (commensurate with the low-stress region in Figure 91) to an open crack at the top of the image. In between, there is a transition in GB damage an increasing density of cavities leading to the IG crack. Large strain plumes around the cracked GB are observed as well. A montage of creep crack #2 demonstrates a symmetry by which the center of the crack is wide open and the damage gradually returns to that representing the as-CW microstructure over 10s of micrometers in each direction. Higher magnification images of the various regions in Figure 92 are shown in Figure 93 and show definitively how the evolution of small cavities can connect to form a larger crack. To demonstrate that this has nothing to do with carbide fallout, two regions of the crack that intersect grain boundaries of minimal damage (Figure 94) are presented. As can be observed, especially in Figure 94b, where the nearly undamaged GB is noted adjacent to an open crack. If the appearance of high amounts of damage were from carbide fallout, it might be expected that the adjacent grain boundaries would also be affected. The observed difference is due to the orientation of the grain boundaries to the applied stress.

EDS elemental mapping (Figure 95) of a region of the open crack representing the highest amount of damage (location noted in Figure 92) and shows that 1) there is a weak oxygen signal (resulting from colloidal silica and Cr-K overlap) suggesting there is no corrosion-product oxide and this is not an SCC crack exposed to water, 2) individual, discontinuous, Cr-K signals in the main crack show that carbides are still present, and 3) the crack is filled with a strong Si signal that suggests it contains colloidal silica. Characterization results on these isolated, internal cracks near the center of the specimen are consistent with them being internal creep cracks formed by linking the high density of closely spaced cavities.

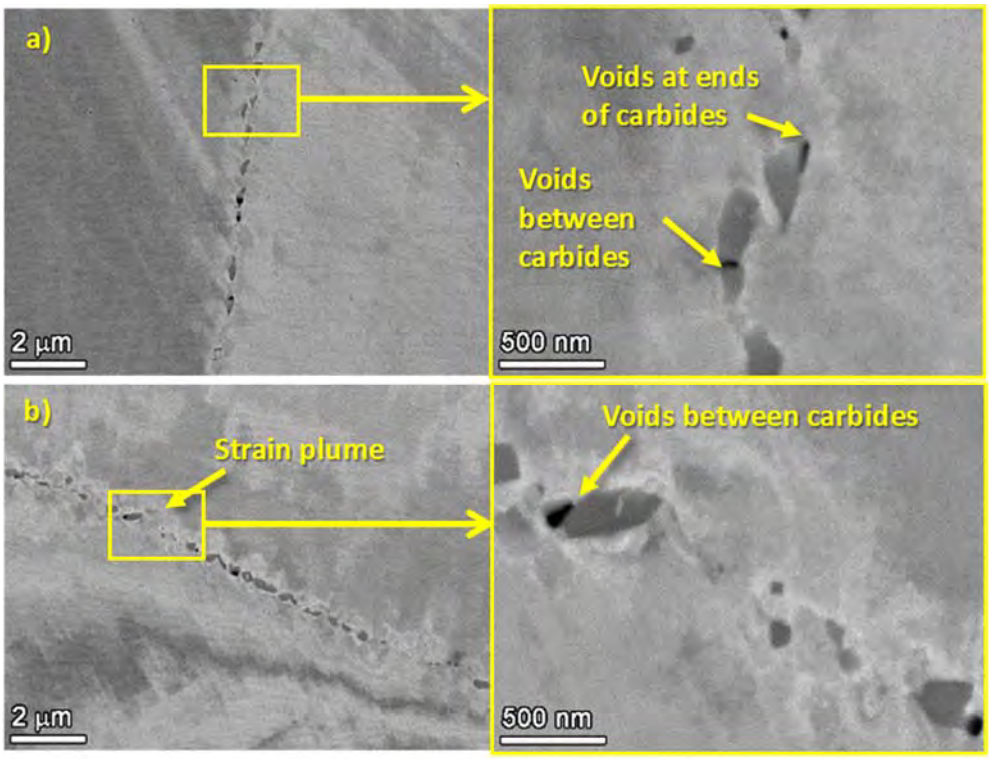

Figure 91. SEM-BSE images of representative cold work-induced GB damage in the lower stress region in the TT+31%CF Valinox CRDM SCC specimen IN037 after 18,400 hours of exposure in 360ºC simulated PWR primary water.

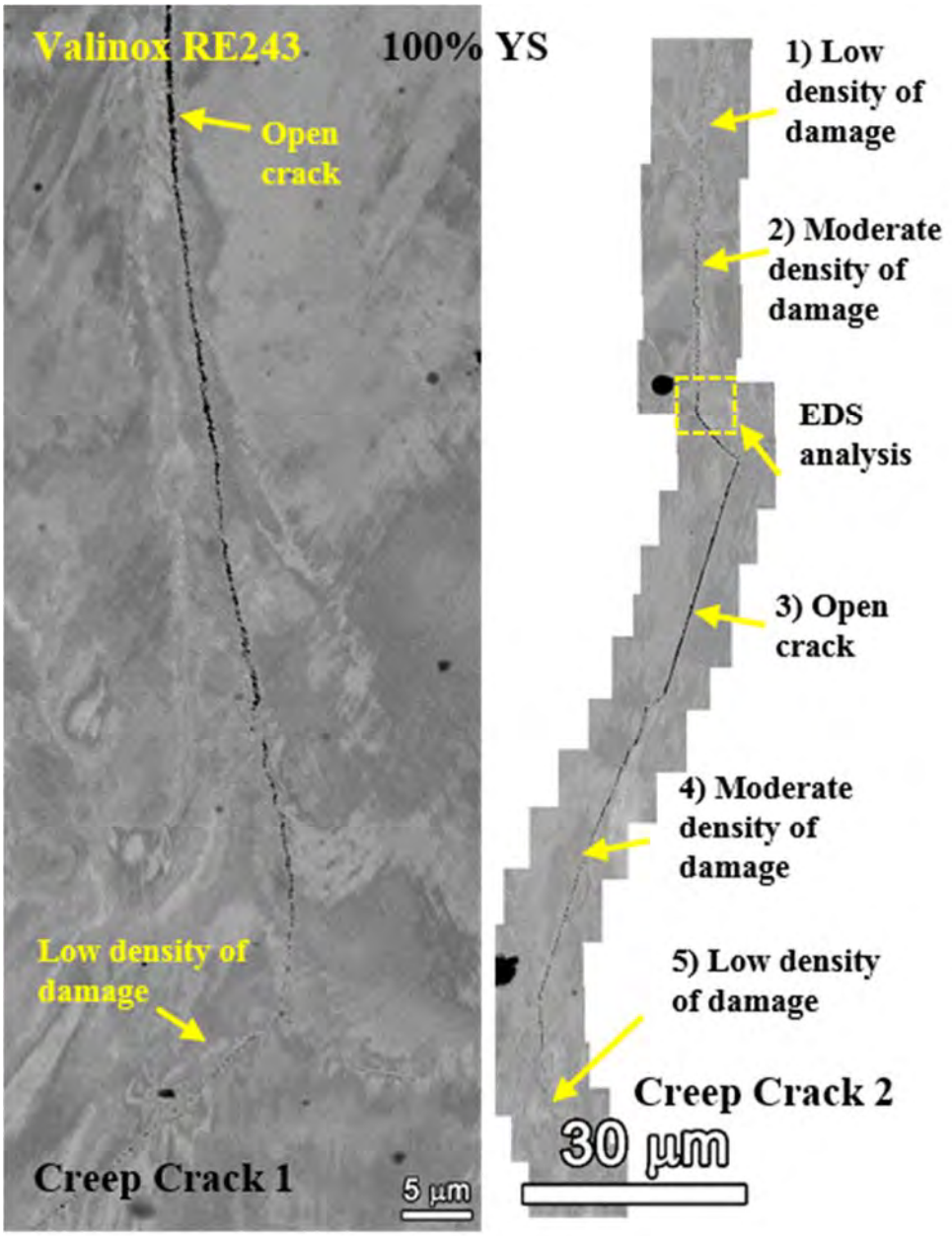

Figure 92. SEM-BSE montages of two creep cracks located in the middle of the initiation sample, both of which illustrate a gradients of no damage to fully open cracks. Higher magnification images of creep crack 2 are shown in Figure 93.

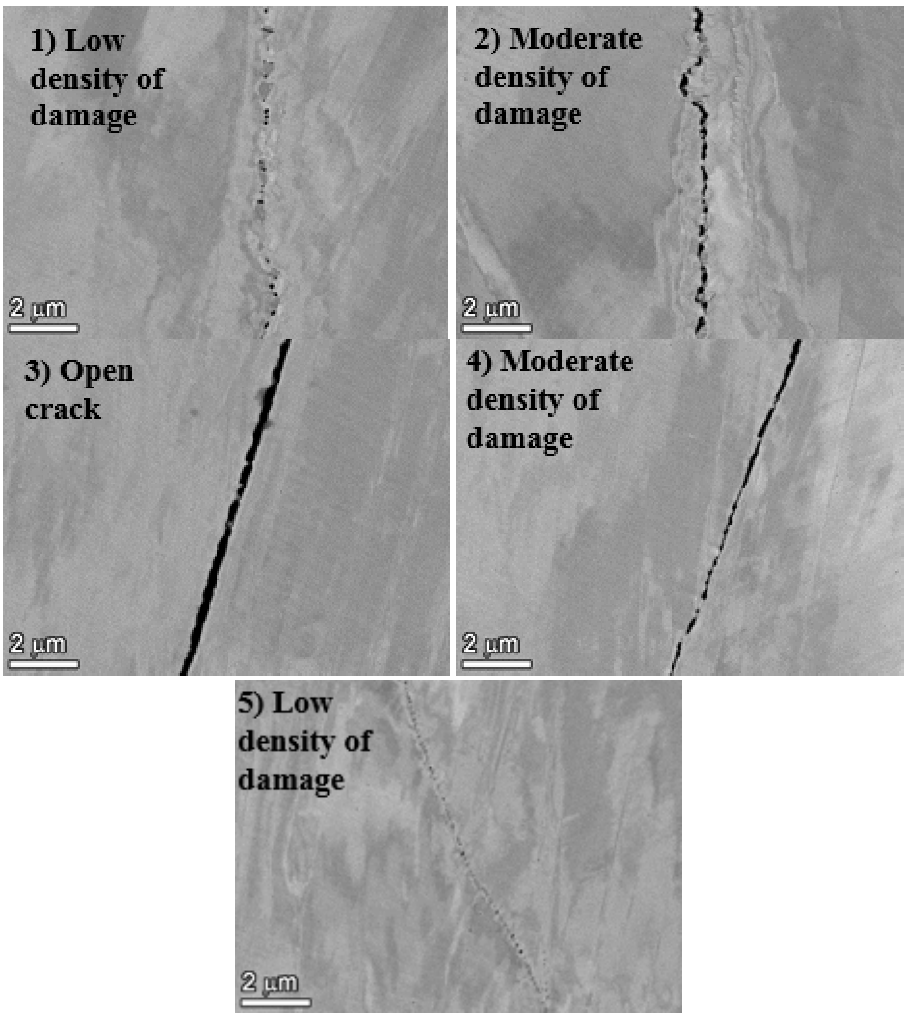

Figure 93. SEM-BSE high magnification images of selected regions in creep crack 2 in Figure 92 exhibiting the gradient of damage from a very low density to a completely open crack.

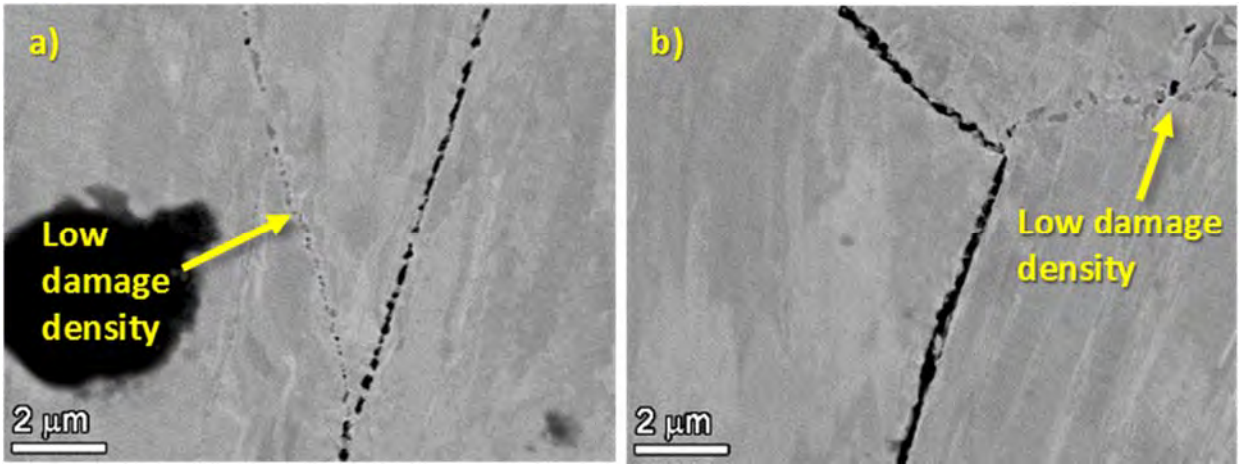

Figure 94. SEM(BSE) of two regions along creep crack 2 in Figure 92 illustrating adjacent grain boundaries that did not exhibit large amounts of damage. The large, circular, blotch on the left of a) is surface debris and not part of the sample.

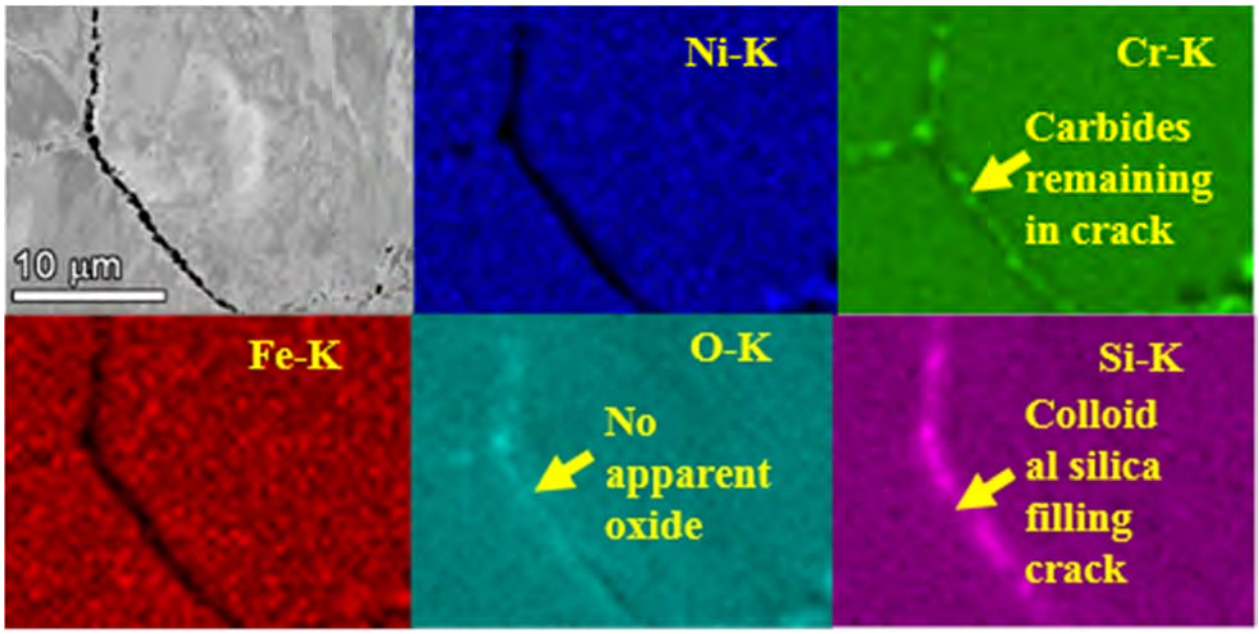

Figure 95. SEM(BSE) and EDS elemental maps from a region of high damage in creep crack 2 in Figure 92 showing no oxide in the crack wall and the crack contain strong Cr and Si signals. The O-K signal is a result of the SiO_2 deposited in the crack wall.

To further demonstrate that the cracks observed in these studies are indeed creep cracks and are not a result of sample preparation artifact, site specific plan-view TEM preparation of crack and damaged boundary regions from the high-stress gauge section was performed. Once again, the TT+31%CF Valinox material was examined after SCC initiation testing for ~9220 hours in simulated PWR primary water at 360˚C. The sample was cross-sectioned by the aforementioned metallographic polishing techniques and characterized using low kV imaging (Figure 96). An open crack within the gauge section was selected for analysis and no evidence of crack wall oxidation was discovered. Remnant carbides could still be identified along the crack walls, indicating that the crack was not a result of carbide fallout. The open crack ended on both sides in a high density of GB cavities. Observations support that this internal crack near the center of the specimen formed by linking a nearly continuous distribution of creep cavities.

STEM annular darkfield (ADF) and EDS elemental mapping of the crack tip and the damaged GB ahead of the crack show a similar appearance, confirming the carbides are still present along the crack walls (Figure 97). There is very little crack wall oxide (if any) and no apparent penetrative oxidation in the matrix. This lack of oxidation indicates that this is a creep crack that has not been exposed to high temperature water. There was no distinguishable oxide ahead of the crack and the oxygen signal is a function of the O-K signal overlapping the Cr-L. The size and morphology of the carbides along the boundary can be observed, and the damage is confined to cavity formation between carbides. Higher magnification examination of the dashed box in

Figure 97 is shown as a tilt series in Figure 98 where cavities in between carbides as well as cavities forming at the ends of carbides are shown. The tilt series of the cavities between the three carbides shows how faceted cavity growth occurs into the matrix and gives a clearer understanding of what is being exhibited in the low kV BSE images. These cavities are typically observed as rounded features in the SEM, the higher resolution STEM images exhibit their true nature as cavities growing into the matrix.

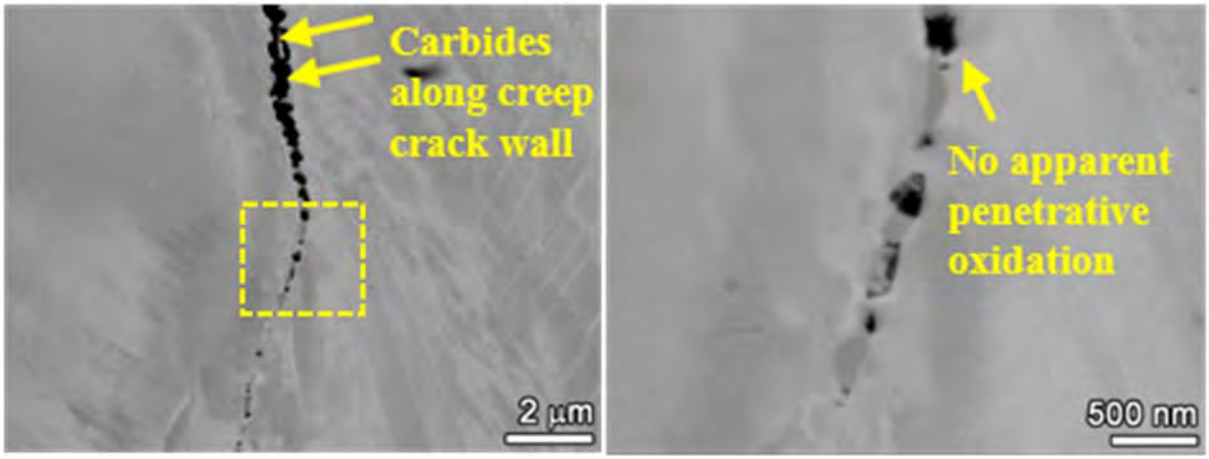

Figure 96. SEM-BSE images of a creep crack observed in the TT+31%CF Valinox RE243 CRDM SCC initiation specimen IN037 after 18,400 hours of exposure in 360°C simulated PWR primary water. A site specific, plan view TEM sample was prepared from this IG crack tip and the boundary ahead.

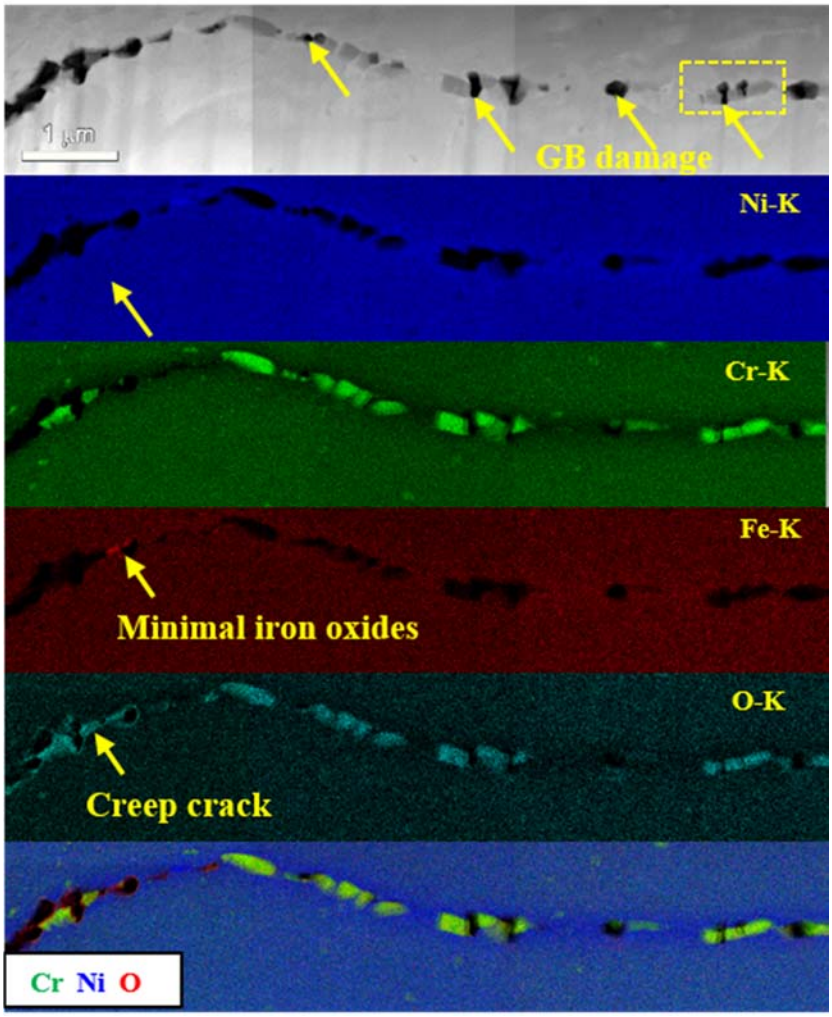

Figure 97. STEM (ADF) and EDS elemental maps of a creep crack and the GB damage ahead of the crack. The oxide signal results from overlap with the Cr-K without any evidence of oxide formation on the crack walls.

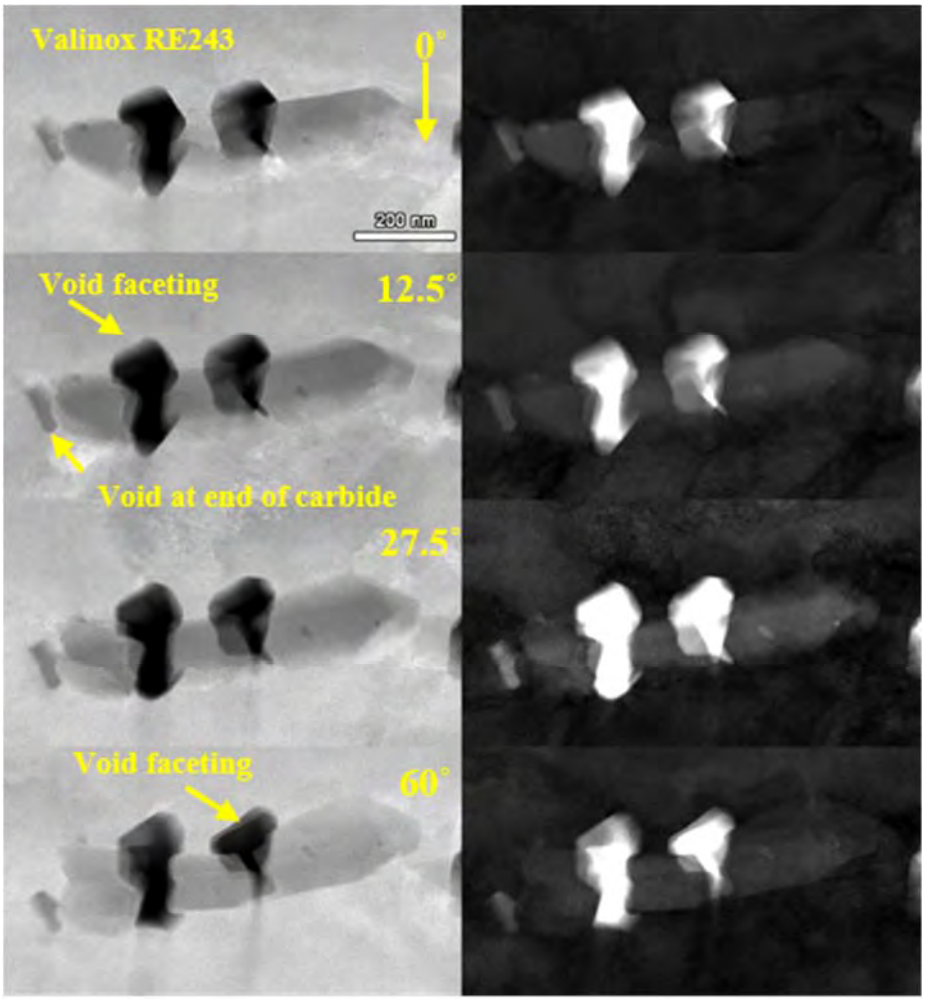

Figure 98. STEM (ADF-left, BF-right) tilt series (0-60˚) about the horizontal axis of the area highlighted in the box in Figure 97 showing how cavities form between IG carbides after ~9,220 hours of test exposure.

As mentioned in the Microstructure Characterizations section, quantification has been performed on the TT+31%CF Valinox and Doosan CRDM specimens to evaluate GB cavity evolution with increase in exposure time and applied stress. These two materials exhibit a similar grain size but very different GB carbide morphologies, enabling a direct comparison on the effect of starting GB microstructure. Results are presented in terms of cavity density and cavity coverage per unit GB length as shown in Figures 99 and 100, respectively. The data for these two materials are shown using the same scale to facilitate comparison. The TT+31%CF Doosan CRDM material exhibits an average of one carbide per every 2-2.5 µm along GBs throughout the specimen. The percentage of GB length containing cavities remained constant at ~5% regardless of test time and applied stress. These results suggest that formation of new cavities has not occurred nor has significant growth of existing cavities taken place in the specimens. In contrast, a large increase in cavity density and cavity coverage at GB was found for the TT+31%CF Valinox CRDM material after Phase II exposure in the gauge section loaded at 100%YS. Although there is scatter in the measurements for these two parameters due to boundary-to-boundary variability in

cavity distribution, the average cavity spacing has grown in average from one cavity per every 0.75 µm after Phase I to one per every 0.67 µm after Phase II, and to one per every 0.5 µm in extreme cases. Meanwhile, the average percentage of cavity coverage at GBs, i.e. decohered fraction of GB has almost doubled in the gauge from ~15% to ~25%, and for some GBs it reached as high as ~37%. It should be noted that cracked portion of the GBs observed in the gauge section were excluded from quantification, therefore the actual value of these two parameters at 100% YS are even higher. The effect of applied stress also started to pick up as testing time proceeds. After Phase I exposure, the GB cavity density and coverage were relatively low until reaching 100% YS, but the increasing trend has become clear starting from ~70% YS after Phase II exposure. Nevertheless, the absolute values are still much lower in comparison to those at 100% YS.

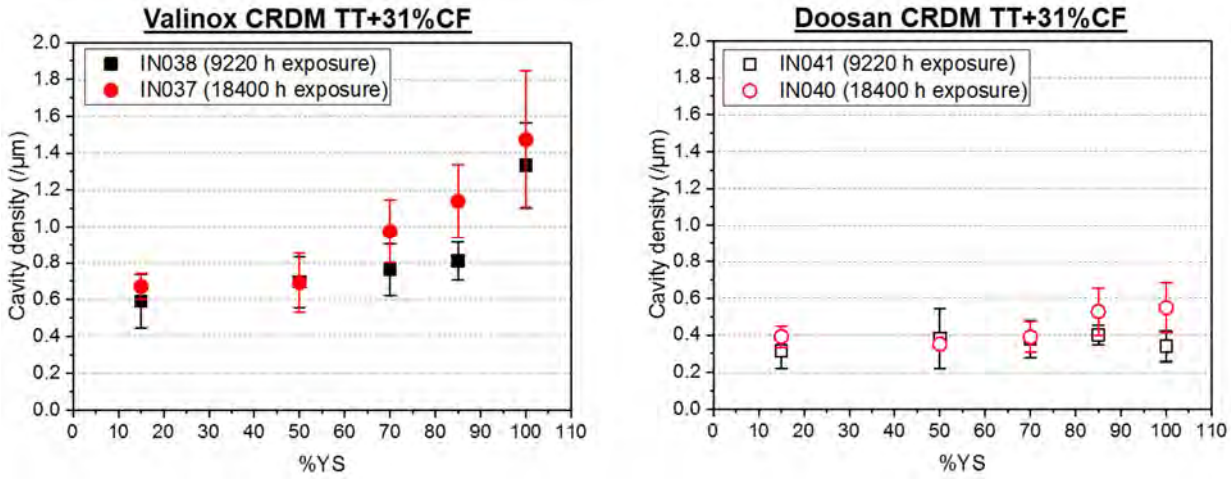

Figure 99. Quantification on cavity density evolution after Phase I and Phase II exposures as a function of applied stress in (a) TT+31%CF Valinox CRDM and (b) TT+31%CF Doosan CRDM SCC initiation specimens.

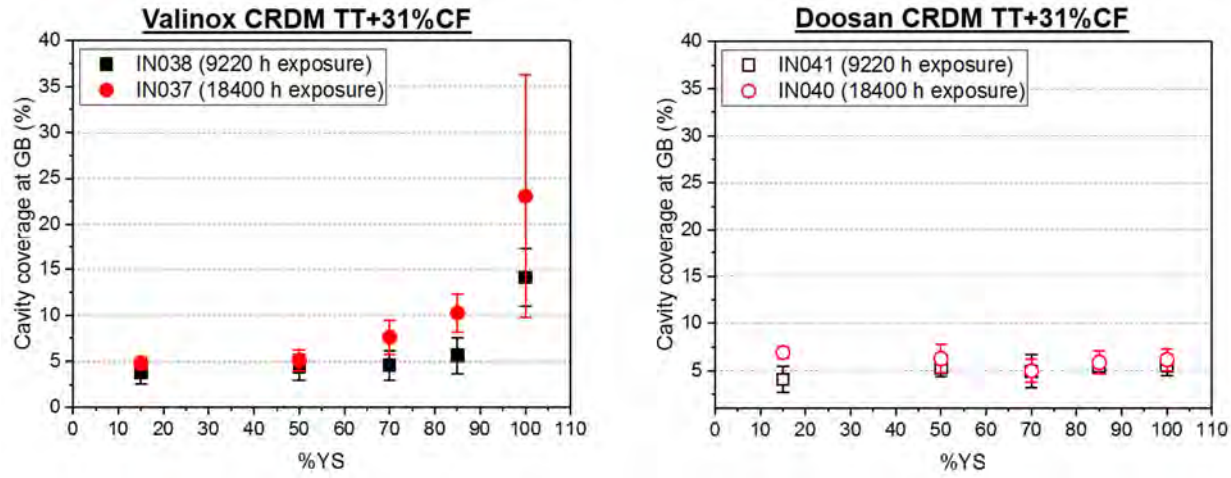

Figure 100. Quantification on GB cavity coverage evolution after Phase I and Phase II exposures as a function of applied stress in (a) TT+31%CF Valinox CRDM and (b) TT+31%CF Doosan CRDM SCC initiation specimens.

DCPD Response

The overall DCPD non-referenced strain response of the instrumented TT+21%CF specimen from the three Alloy 690 CRDM heats during Phase II and Phase III exposure are presented in Figure 101 and Figure 102, respectively. No DCPD indication of crack initiation has been seen in any of these specimens. Plotted using the same scale for the DCPD non-referenced strain in these two figures, it is obvious that these three specimens consistently exhibit a decreasing strain evolution over the entire test period. While resistivity drift is not corrected, this decreasing trend is an indicator of creep that is gradually slowing down. It is also interesting to note that the magnitude of strain evolution in the TT+21%CF specimens is much smaller than that observed in their TT+31%CF counterparts (Figure 81), suggesting % cold work/and the applied stress control the strain evolution for specimens loaded at their yield stress.

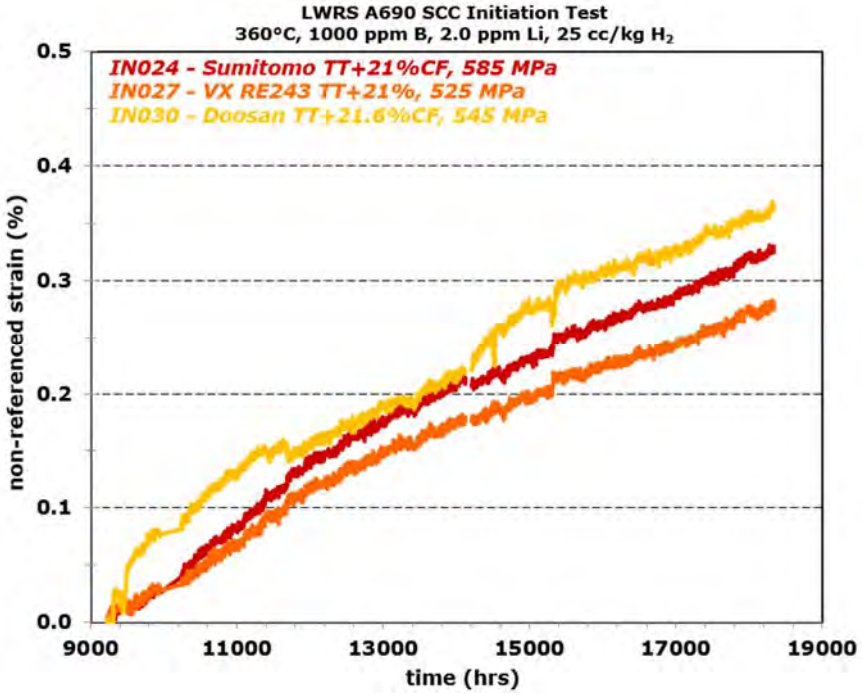

Figure 101. DCPD non-referenced strain response for the instrumented specimens from the three TT+21%CF Alloy 690 CRDM heats during the entire Phase II testing period.

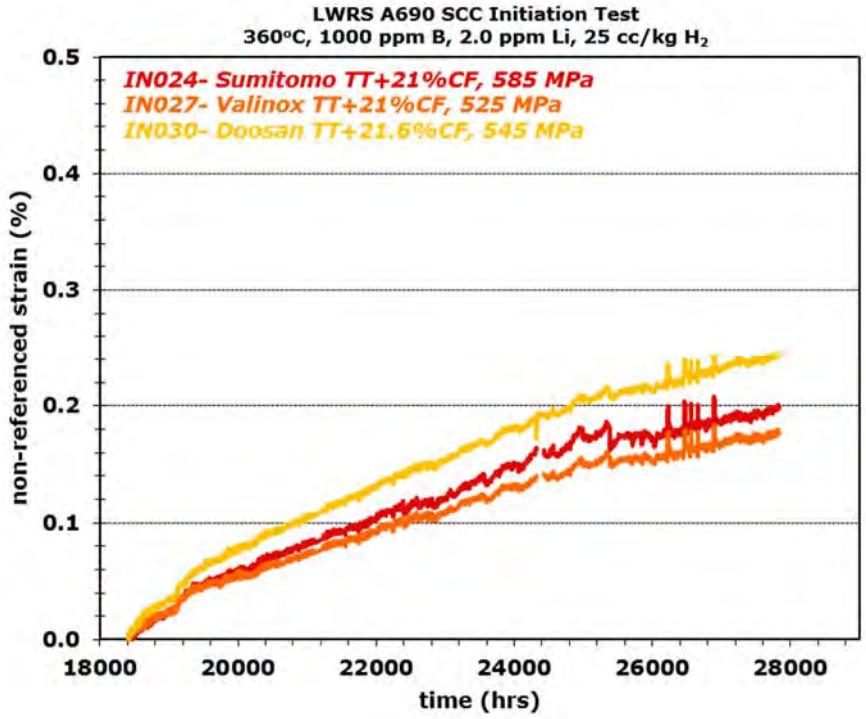

Figure 102. DCPD non-referenced strain response for the instrumented specimens from the three TT+21%CF Alloy 690 CRDM heats during the entire Phase III testing period.

GB Damage Evolution on the Surface

Unlike in the TT+31%CF specimens where obvious cracks can be easily identified in low-magnification SEM-BSE montage images of the gauge surface, the highly polished TT+21%CF specimens exhibit more subtle damage features that can only be resolved under high resolution examination at higher magnifications even after ~28,000 hours of exposure. Therefore, additional close-up SEM examinations were routinely performed at the same randomly selected sites in these specimens after each test interruption. This enabled direct assessment of the evolution of precursor damage with examples shown for the TT+21%CF specimens from the three Alloy 690TT CRDM heats Sumitomo (Figure 103), Valinox (Figure 104), and Doosan (Figure 105). All three specimens exhibit "postage stamp" features along most high-energy GBs after Phase II exposure. As reported in an earlier milestone report [30], these features have been shown to be associated with discrete cavities intersecting the surface using serial FIB trenching. After Phase III exposure, these postage stamp features on the high-energy GBs have started to link up and appear to be forming more continuous IG damage on certain GBs in the TT+21%CF Sumitomo and Valinox materials with closely spaced nanometer-sized carbides (Figures 103 and 104). In comparison, little evolution of the postage stamp features was found in the TT+21%CF Doosan material having larger carbides that are more widely spaced (Figure 105).

Interestingly, the most obvious surface cracks have been identified on the TT+21%CF TK-VDM Plate specimen IN060 after Phase III exposure, where some IG cracks were readily identifiable in the low-magnification SEM-BSE montage images on the gauge surface. The details will be presented in the next section along with cross-section examination performed by serial FIB trenching of the cracks.

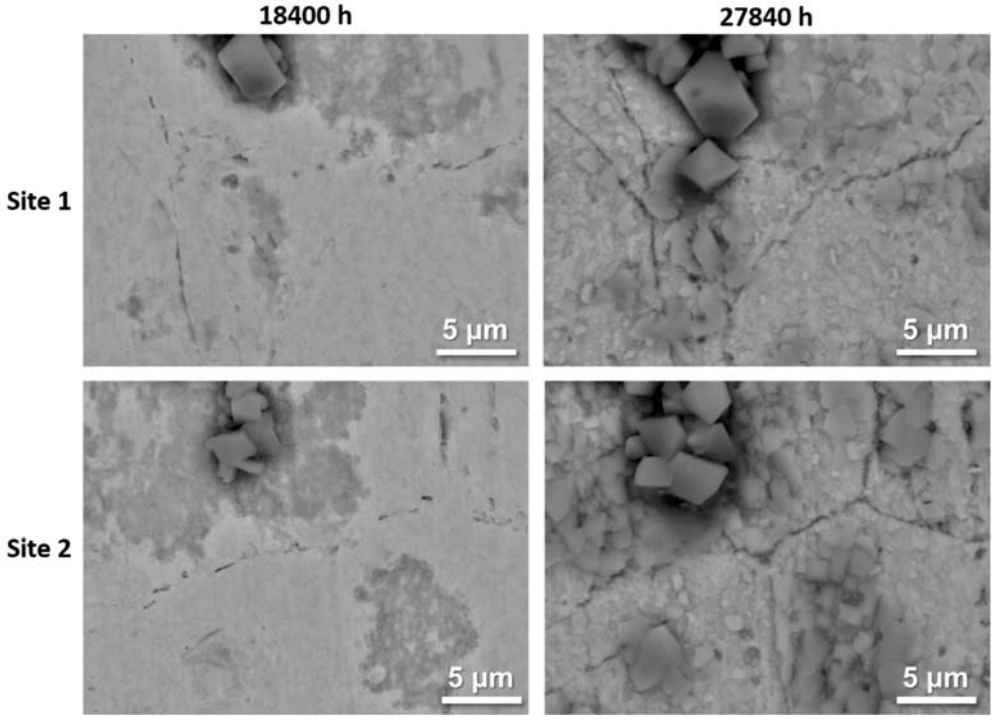

Figure 103. SEM-BSE images of the typical surface morphology examined at the same sites after Phase II (left) and Phase III (right) exposure in the 1 µm finish, TT+21%CF Alloy 690 Sumitomo CRDM specimen IN024.

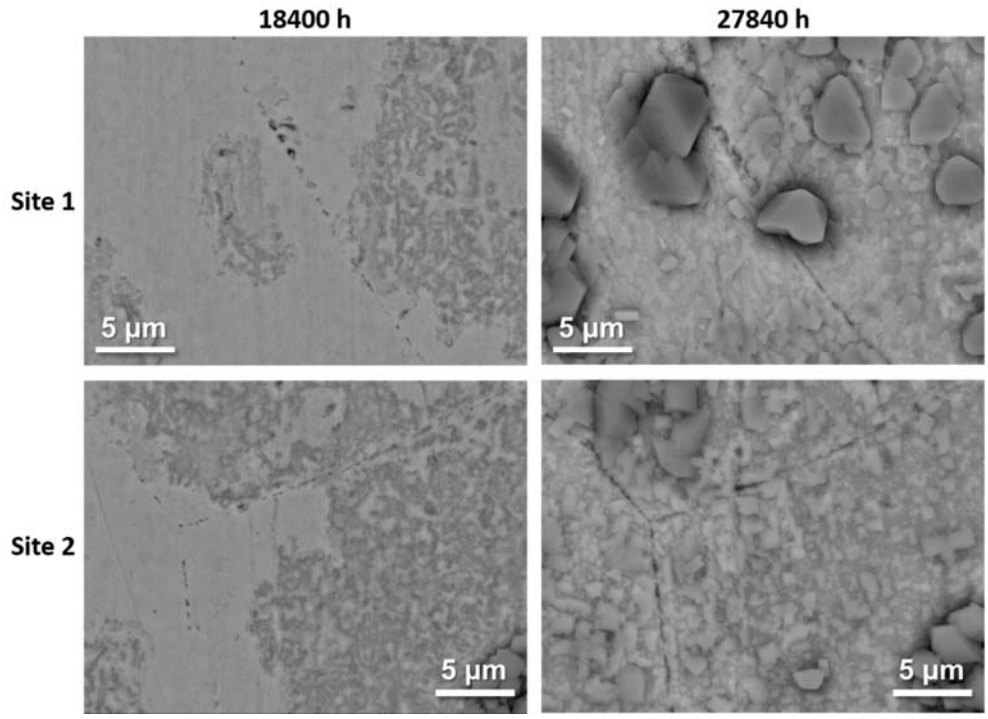

Figure 104. SEM-BSE images of the typical surface morphology examined at the same sites after Phase II (left) and Phase III (right) exposure in the 1 µm finish, TT+21%CF Alloy 690 Valinox CRDM specimen IN027.

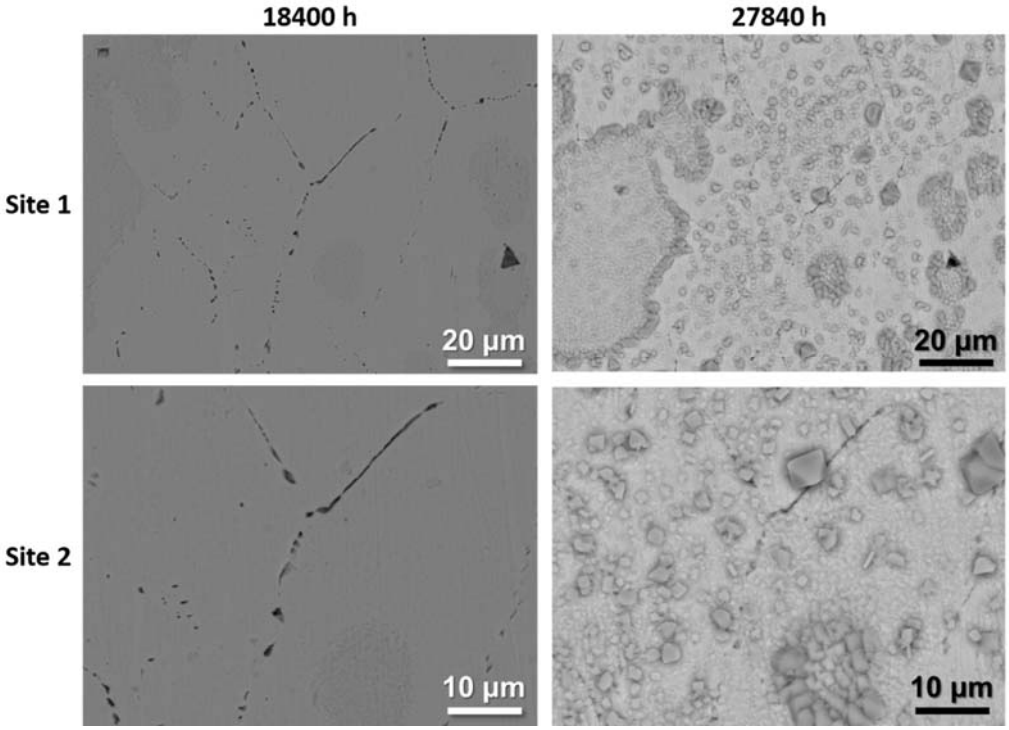

Figure 105. SEM-BSE images of the typical surface morphology examined at the same sites after Phase II (left) and Phase III (right) exposure in the 1 µm finish, TT+21%CF Alloy 690 Doosan CRDM specimen IN030.

GB Damage Evolution in the Cross-Section

One specimen from each of the three TT+21%CF Alloy 690 CRDM materials were removed after Phase II for cross-section examinations throughout the thickness of the entire gauge section with results shown in Figure 106. A slight increase in GB cavity aggregations was observed in the TT+21%CF Sumitomo CRDM material. However, rather than formation of new GB cavities, this is likely due to the increase in the size of existing cavities making them observable in the low-resolution montage images (Figure 106a). As for the 21%CF specimens from the Valinox and Doosan CRDM heats, GB cavities were sporadically evidenced at higher magnifications, but their size and density were too low to be identified in the montage maps (Figures 106b and c). This indicates a much lower kinetics of GB cavity formation and growth in the 21%CW Alloy 690 materials even after extended testing in 360^{o}C simulated PWR primary water. Quantification similar to what has been done on the TT+31%CF Valinox and Doosan specimens is undergoing for the same two materials at 21%CF condition and the results will be reported in near future.

Since there is only one original TT+21%CF specimen from each heat still remaining in test after Phase III exposure, decision was made to only employ non-destructive serial FIB trenching in the specimens to get an idea of the distribution of GB cavity in the bulk. Examples of results is shown for the Valinox CRDM specimen IN027 in Figure 107 and Doosan CRDM specimen in Figure 108. Very shallow IG damage right beneath the surface with a depth of a few hundreds of nanometers were observed in both specimens, but the Valinox CRDM specimen appears to have a higher density of GB cavities than the Doosan CRDM specimen, which can again be associated with the difference in their GB carbide distributions. However, to date only one GB was investigated in each specimen and more data is needed to confirm this trend.

As mentioned in the previous section, crack nucleation was identified in the TT+21%CR TK-VDM Plate specimen IN060 after Phase III exposure. The rotation of the specimen exhibiting the highest density of IG cracks is presented in Figure 109a with zoom-in images (Figure 109b) showing more detailed surface morphology of two selected cracks, one relatively long (surface length ~100 μm) and one very short (surface length <30 μm). Serial FIB trenching was performed on these two cracks starting from region outside the crack tip to opened portion of the crack. The sub-surface morphology of the trenches revealed small, closely spaced GB cavities leading at the crack tips (Figure 109c). This again confirmed the important role of GB creep cavities on IG crack nucleation.

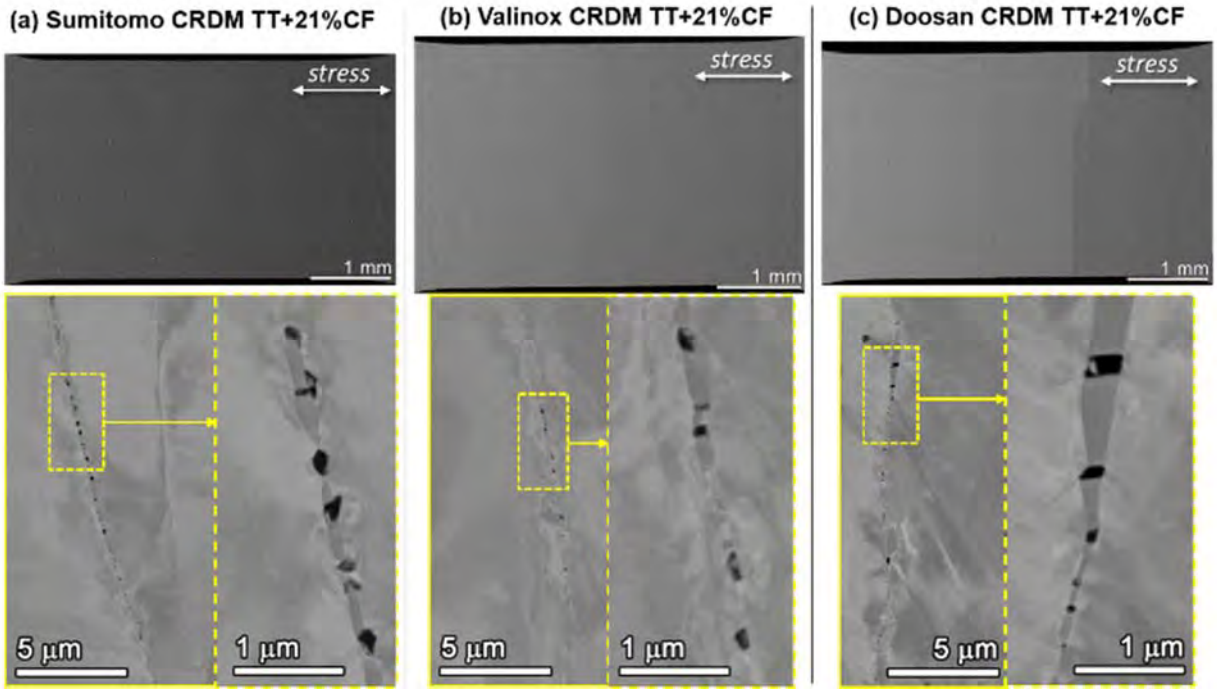

Figure 106. SEM-BSE montage images of the gauge cross-section with higher magnification images on the typical morphology of GB cavity aggregation after Phase II exposure in the ground finish, TT+21%CF Alloy 690 CRDM specimens (a) Sumitomo IN025, (b) Valinox IN028, and (c) Doosan IN031.

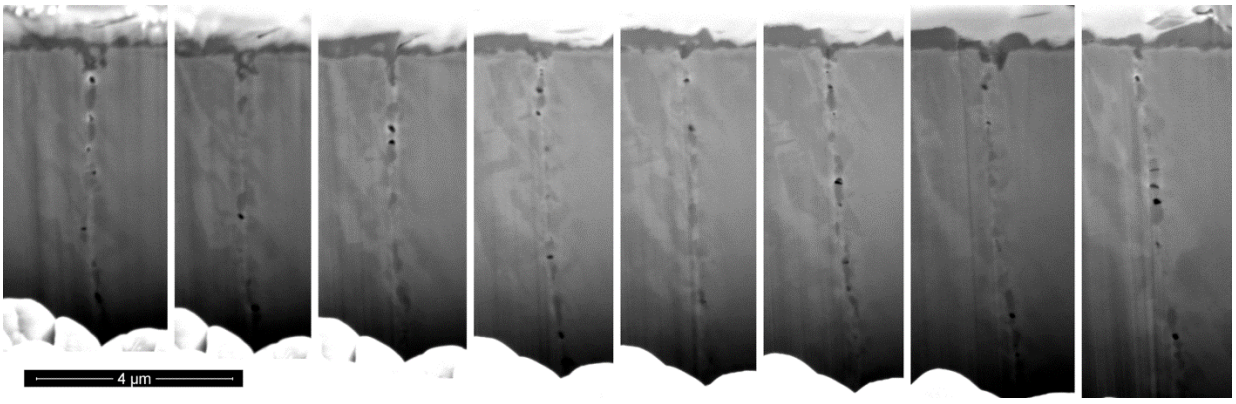

Figure 107. Low-kV FIB-SE image of GB cavities revealed by serial FIB trenching in the 1 µm finish, TT+21%CF Valinox CRDM specimen IN027 tested at yield stress after 27,840 hours of exposure in 360ºC simulated PWR primary water.

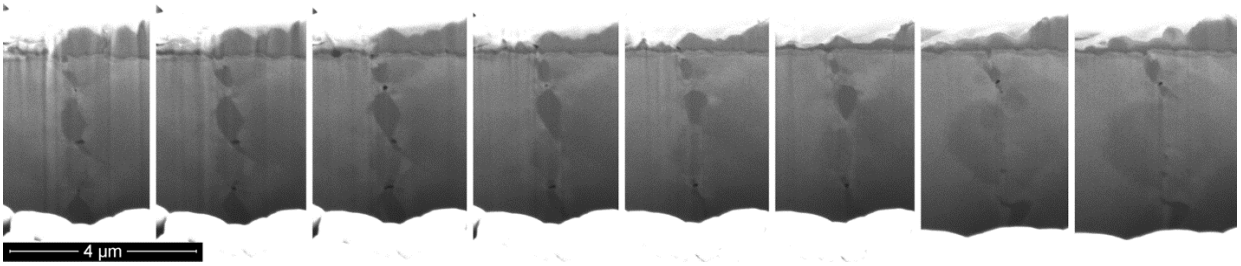

Figure 108. Low-kV FIB-SE image of GB cavities revealed by serial FIB trenching in the 1 µm finish, TT+21.6%CF Valinox CRDM specimen IN030 tested at yield stress after 27,840 hours of exposure in 360ºC simulated PWR primary water.

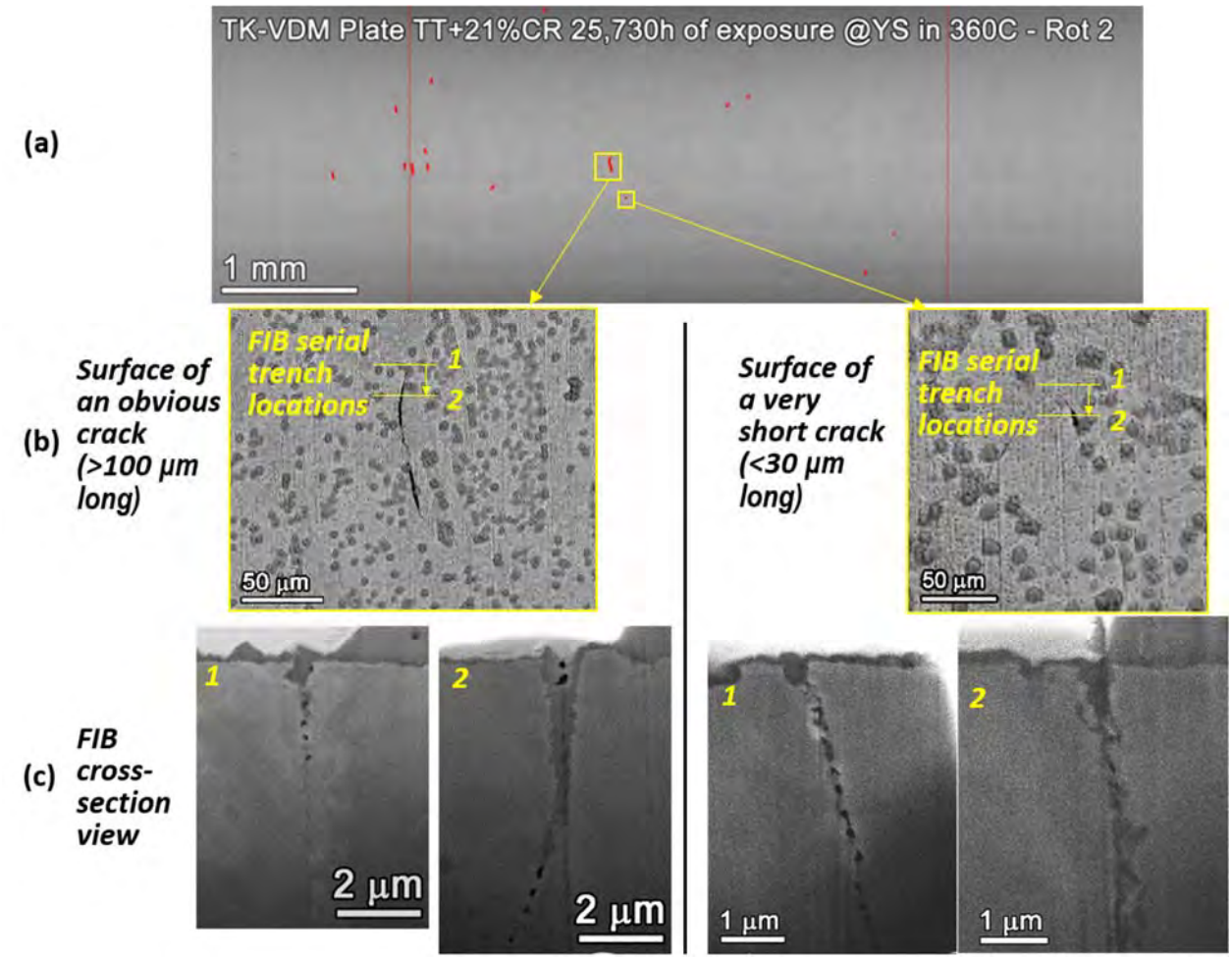

Figure 109. SEM-BSE montage images (a) of one rotation of the TT+21%CR Alloy 690 TK-VDM Plate specimen IN060 after Phase III (25,730 hours) exposure. Higher magnification SEM-BSE images of the surface morphology of identified cracks (b) and FIB-SE images of the cross-section of the cracks (c) are also shown.

Discussion

All of the Alloy 690TT materials evaluated in this report exhibited a semi-continuous distribution of carbides at high energy GBs, but their starting microstructures varied in terms of carbide size, carbide density and grain size. Interestingly, the GB carbide microstructures considered beneficial to IGSCC resistance appears to be the most susceptible to IG cavity formation and growth in highly CW Alloy 690. The homogeneous grain structures with semi-continuous distribution of small carbides at GBs as observed in Sumitomo and Valinox CRDM materials have led to the most prevalent GB cavity distributions in the gauge cross-section for the highly CW conditions after both Phases I and II exposures (Figures 89-90). The detailed quantification of GB cavity distributions between the TT+31%CF Valinox and Doosan CRDM materials suggest that a high density of closely spaced, small GB carbides promotes more rapid cavity nucleation and growth. It is reasonable to assume that the GB cavity distribution prior to testing can be represented by data acquired at the site of 15%YS in the specimen because little increase was observed in terms of cavity coverage and cavity density in either material after exposures up to 18,400 hours (Figures 99 and 100). As indicated in Figure 100, the two materials exhibit similar pre-test GB cavity coverage, but in the TT+31%CF Valinox CRDM material it was due to a moderate density of small-sized cavities while in the TT+31%CF Doosan CRDM material it was due to much fewer but larger cavities. As test proceeds, only the former showed obvious increase in cavity density and coverage at GBs in the gauge section (Figures 99 and 100). In particular, the cavities became so closely spaced at many GBs that they finally link up, resulting in IG creep cracks of a few hundreds of micrometers in length (Figure 90).

It also is worth noting that even among the materials featuring a semi-continuous distribution of small carbides, subtle differences in carbide spacing and grain size can alter cavity evolution over time, especially in the highly stressed gauge area. This is demonstrated in the Phase II observations of the TT+31%CF specimens from the Sumitomo CRDM (Figure 89), Valinox CRDM (Figure 90) and TK-VDM plate (Figure 88) materials. With identical total exposure times, a much slower increase in the cavity size and density took place in the TK-VDM plate material that has slightly larger spacing between GB carbides (~100-500 nm) than the other two materials (~100 nm). The GB carbide size and spacing in the Valinox CRDM material is very similar to those in the Sumitomo CRDM material, but the grain size of the Valinox CRDM is roughly 2.5 times larger than that of the latter (Table 6). After both Phases I and II exposure, the TT+31% CF Sumitomo CRDM specimen always showed the highest density of GB cavities, which is consistent with the statement of Arioka et al. [23] where they believe a smaller grain size will promote more rapid vacancy accumulation and cavity nucleation. Nevertheless, the TT+31% CF Valinox CRDM material has outpaced its Sumitomo counterpart in IG crack formation (so far) and has led to earlier DCPD detection of crack initiation. In addition, a much lower degree of vacancy accumulation took place in the TT+31%CF Doosan CRDM material, although it exhibits a similar grain size as the Valinox CRDM material. These findings suggest that GB carbide distribution may have a more important role over grain size in vacancy diffusion and condensation, of which the mechanism remains to be clarified.

Quantitative analysis has been performed on the TT+31%CF Valinox and Doosan CRDM specimens to evaluate the effect of starting GB microstructure on GB cavity evolution in this report. Neither cavity density nor cavity coverage at GB exhibited observable increase with increase in applied stress from 15% to 100% yield stress or exposure time from 9,220 to 18,400 hours in the Doosan CRDM material featuring micrometer size carbides widely spaced at GBs. In comparison, it is obvious that after 9,220 hours of test exposure, the GB cavity density and coverage increased sharply as the applied stress approaching 100%YS in the TT+31%CF Valinox material (Figures 99 and 100). After 18,400 hours of test exposure, the values of these two parameters started to pick up from an applied stress of ~70%YS. Although the GB cavity distribution development at lower stress is still much less than what needed to form IG cracks, it appears likely that cavity evolution will continue with test time. Further assessment is needed to determine whether this is true and whether it will lead to IG creep cracking at lower applied stresses.

Interestingly, the observation on TT+21%CW Alloy 690 specimens after Phase III (27,840 hours of test exposure) revealed that despite extensive "postage stamp" damage on the GBs in all materials, only the TK-VDM plate heat has shown a low density of obvious IG cracks on the gauge surface. One possible reason of the TK-VDM material being the first to exhibit crack nucleation rather than the Sumitomo or Valinox CRDM materials featuring more refined and continuous GB carbides lies in the difference in their applied stress. As shown in Table 6, the applied stress (yield stress) of the TT+21%CR TK-VDM specimens is 13-22% higher than that of the CRDM materials, which can have a significant effect on cavity formation and growth during long-term exposure. However, the differences in surface precursor damage among the TT+21%CW materials is limited and all indicate the increased resistance to GB cavity evolution and crack formation in comparison to the TT+31%CW materials.

Summary and Conclusions

The effect of GB microstructure on precursor damage evolution and SCC initiation was evaluated in CW Alloys 600 and 690 using constant load testing in 360ºC simulated PWR primary water. The data acquired is providing key information to predict long-term degradation behavior of Ni-base alloys in service-relevant operating conditions, as well as improved mechanistic understanding to model SCC initiation behavior incorporating microstructural variables.

The current investigation focused on one Alloy 600 heat that was received in the MA condition and tested in a range of CW conditions. In order to critically assess GB carbide effects, this material was solution annealed and water quenched to remove most GB carbide precipitates, then thermal treated to produce a semi-continuous distribution of GB carbides without altering the grain size. All three starting conditions (MA, SA and SA+TT) were 15%CF and tested in 360ºC simulated PWR primary water. Long-term corrosion exposures were performed on unstressed coupons to determine IGA behavior and results were compared to SCC initiation response on tensile specimens at constant load. Although the IGA and SCC initiation response of the SA (few GB carbides) and TT (semi-continuous GB carbides) materials were expected to exhibit significant differences, similar IGA depth evolution and SCC initiation times were observed. The SCC initiation results may have been influenced by the fact that the TT+15%CF specimens exhibited a higher yield stress and were loaded at an applied stress that is ~12% higher than that of the SA+15%CF specimens. An obvious increase in IGA depth was found for SCC initiation specimens in all material conditions as compared to the unstressed exposure coupons with the same GB microstructures, indicating a predominant role of mechanical factors in IGA growth regime. In addition, a good inverse-linear relationship was consistently found between steady state creep strain rate and time to SCC initiation in all three material conditions, indicating creep deformation is critical in promoting the growth of short cracks to engineering relevant rates. These findings suggest that a mechanical component is essential to accurately predict the evolution of GB damage precursors that lead to practical SCC initiation in CW Alloy 600.

On the other hand, long-term constant load testing on moderately to highly CW Alloy 690TT materials revealed that creep-induced GB cavity formation can and does occur during long-term exposure in 360ºC simulated PWR primary water. A high density of these internal GB cavities have provided the necessary IG damage required for crack initiation. Detailed characterization and quantification performed on GB cavity evolution in four Alloy 690TT materials with 21% and 31% cold work levels demonstrated that the size and spacing of the carbides directly influence GB cavity formation and growth. Somewhat unexpectedly, the GB microstructure that was considered the most beneficial to SCC resistance, i.e. a semi-continuous distribution of closely spaced nanometer-sized carbides, turned out to be the most susceptible to GB cavity formation and growth. In highly CW conditions, this type of GB microstructure has induced DCPD-detected crack initiation in highly stressed specimen gauge sections due to extensive GB cavity formation and link-up to create internal IG creep cracks at ~15,400 hours of exposure.

Using a thermal activation energy reported for creep (175 kJ/mol [25]) in CW Alloy 690TT, the crack initiation time at 360°C for this 31%CW material suggest a crack initiation time of ~16 years at 320°C. In moderately CW materials with similar GB microstructures, very small precursor IG cracks were identified on specimen gauge surface after 2.9 years of testing. Subsequent FIB cross section trenching revealed small, closely spaced GB cavities leading at the crack tips, confirming the important role of GB creep cavities on IG crack nucleation in CW Alloy 690. While still at a cold work level higher than that expected in service, new results highlight this important degradation issue that may impact long-term performance and justifies continued SCC initiation testing on the 10-15%CW Alloy 690 materials.

Acknowledgement

The authors recognize collaborative research activities funded by the Electric Power Research Institute on the exposure of unstressed Alloy 600 coupons and the Office of Basic Energy Sciences for high-resolution characterizations of GB damage and crack tips. These collaborations have been essential to the success of the SCC initiation research. The helpful discussion with Dr. Daniel Schreiber on interpreting analytical microscopy results on IGA in Alloy 600 is graciously acknowledged. Dr. Karen Kruska is acknowledged for performing the FIB serial trenching on Alloy 690 specimens. Critical technical assistance is also recognized from Rob Seffens and Ryan Bouffioux for SCC experimentation and Anthony Guzman for metallographic specimen preparation.

References

[1] D. K. Schreiber, M. J. Olszta, K. Kruska and S. M. Bruemmer, "Role of Grain Boundary Cr_5B_3 Precipitates on Intergranular Attack in Alloy 600", in *Proceedings of the 18th International Conference on Environmental Degradation of Materials in Nuclear Power Systems – Water Reactors: Volume 1*. 2018, Springer International Publishing, pp. 359-374.

[2] R. A. Etien, E. Richey, D. S. Morton and J. Eager, "SCC initiation testing of alloy 600 in high temperature water", in *15th International Conference on Environmental Degradation of Materials in Nuclear Power Systems - Water Reactors*, 2011, Colorado Springs, CO, USA: The Minerals, Metals & Materials Society.

[3] S. M. Bruemmer, M. J. Olszta, D. K. Schreiber and M. B. Toloczko, *Corrosion and Stress Corrosion Crack Initiation of Cold Worked Alloy 600 and Alloy 690 in PWR Primary Water Environments*. Technical Milestone Report M2LW-13OR0402035, Light Water Reactor Sustainability Program, DOE Office of Nuclear Energy, September 2014.

[4] M. J. Olszta, D. K. Schreiber, M. B. Toloczko and S. M. Bruemmer, *Microstructure, Corrosion and Stress Corrosion Crack Initiation of Alloy 600 in PWR Primary Water Environments*. Technical Milestone Report M3LW-13OR0403032, Light Water Reactor Sustainability Program, DOE Office of Nuclear Energy, March 2013.

[5] Z. Zhai, M. B. Toloczko, M. J. Olszta and S. M. Bruemmer, "Stress corrosion crack initiation of alloy 600 in PWR primary water", *Corrosion Science*, Vol.123, 2017, pp. 76-87.

[6] Z. Zhai, M. B. Toloczko, M. J. Olszta, D. K. Schreiber and S. Bruemmer, *Stress corrosion crack initiation of alloy 600 in simulated PWR primary water*. Pacific Northwest National Laboratory: Technical Milestone Report M2LW-17OR0402034, Light Water Reactor Sustainability Program, DOE Office of Nuclear Energy, September 2017.

[7] M. B. Toloczko, M. J. Olszta, Z. Zhai and S. M. Bruemmer, "Stress corrosion crack initiation measurements of alloy 600 in PWR primary water", in *17th International Conference on Environmental Degradation of Materials in Nuclear Power Systems - Water Reactors*, 2015, Ottawa, ON, Canada: Canadian Nuclear Society.

[8] P. L. Andresen, I. P. Vasatis and F. P. Ford, "Behavior of short cracks in stainless steel at 288°C", in *CORROSION 1990*, Las Vegas, Nevada, USA.

[9] E. Richey, D. S. Morton and M. K. Schurman, "SCC initiation testing of nickel-based alloys using in-situ monitored uniaxial tensile specimens", in *12th International Conference on Environmental Degradation of Materials in Nuclear Power Systems - Water Reactors*, 2005, Salt Lake City, UT, USA: The Minerals, Metals & Materials Society.

[10] S. M. Bruemmer, M. J. Olszta, D. K. Schreiber and M. B. Toloczko, *Stress Corrosion Crack Initiation of Cold-Worked Alloy 600 and Alloy 690 in PWR Primary Water*. Pacific Northwest National Laboratory: Technical Milestone Report M2LW-14OR0404023, Light Water Reactor Sustainability Program, DOE Office of Nuclear Energy, September 2014.

[11] D. K. Schreiber, M. J. Olszta and K. Kruska, *Intergranular oxidation of thermally treated Alloy 600 coupons*. Pacific Northwest National Laboratory: Technical Report DE-AC05-76RL01830, July 2018.

[12] M. Olszta, D. Schreiber, L. Thomas and S. Bruemmer, "High-resolution crack imaging reveals degradation processes in nuclear reactor structural materials", *Advanced Materials & Processes*, Vol.170, Iss.4, 2012, pp. 17-21.

[13] K. Thompson, D. Lawrence, D. J. Larson, J. D. Olson, T. F. Kelly and B. Gorman, "In situ site-specific specimen preparation for atom probe tomography", *Ultramicroscopy*, Vol.107, Iss.2-3, 2007, pp. 131-139.

[14] L. A. Giannuzzi and F. A. Stevie, "A review of focused ion beam milling techniques for TEM specimen preparation", *Micron*, Vol.30, Iss.3, 1999, pp. 197-204.

[15] M. K. Miller and R. G. Forbes, "Atom-Probe Tomography: The Local Electrode Atom Probe". 2014, New York: Springe.

[16] Z. Zhai, M. Toloczko, K. Kruska, D. Schreiber and S. Bruemmer, "Grain Boundary Damage Evolution and SCC Initiation of Cold-Worked Alloy 690 in Simulated PWR Primary Water", in *18th International Conference on Environmental Degradation of Materials in Nuclear Power Systems – Water Reactors*, August 13-17th, 2017, Portland, OR, USA.

[17] S. M. Bruemmer, M. J. Olszta, D. K. Schreiber and M. B. Toloczko, *Corrosion and Stress Corrosion Crack Initiation of Cold Worked Alloy 600 and Alloy 690 in PWR Primary Water Environments*. Pacific Northwest National Laboratory: Technical Milestone Report M2LW-13OR0402035, Light Water Reactor Sustainability Program, DOE Office of Nuclear Energy, September 2014.

[18] Z. Zhai, M. J. Olszta, M. B. Toloczko and S. M. Bruemmer, *Summary of Stress Corrosion Crack Initiation Measurements and Analyses on Alloy 600 and Alloy 690*. Pacific Northwest National Laboratory: Technical Milestone Report M2LW-15OR0402034, Light Water Reactor Sustainability Program, DOE Office of Nuclear Energy, September 2015.

[19] Z. Zhai, M. B. Toloczko and S. M. Bruemmer, *Stress corrosion crack initiation behavior of Alloy 600 and Alloy 690 in PWR primary water*. Pacific Northwest National Laboratory: Technical Milestone Report M2LW-18OR0402034, Light Water Reactor Sustainability Program, DOE Office of Nuclear Energy, September 2018.

[20] Z. Zhai, M. J. Olszta, M. B. Toloczko and S. M. Bruemmer, "Precursor corrosion damage and stress corrosion crack initiation in alloy 600 during exposure to PWR primary water", in *17th International Conference on Environmental Degradation of Materials in Nuclear Power Systems - Water Reactors*, 2015, Ottawa, ON, Canada: Canadian Nuclear Society.

[21] Z. Zhai, M. Toloczko and S. Bruemmer, "Microstructural Effects on SCC Initiation in PWR Primary Water for Cold-Worked Alloy 600", in *18th International Conference on Environmental Degradation of Materials in Nuclear Power Systems – Water Reactors*, August 13-17th, 2017, Portland, OR, USA.

[22] R. N. Parkins, "1990 Plenary Lecture: Strain Rate Effects in Stress Corrosion Cracking", *Corrosion*, Vol.46, Iss.3, 1990, pp. 178-189.

[23] K. Arioka, "2014 Whitney Award Lecture: Change in Bonding Strength at Grain Boundaries before Long Term SCC Initiation", *Corrosion*, Vol.71, Iss.4, 2015, pp. 403-419.

[24] K. Arioka, T. Miyamoto, T. Yamada and M. Aoki, "Role of Cavity Formation in Crack Initiation of Cold-Worked Carbon Steel in High-Temperature Water", *Corrosion*, Vol.69, Iss.5, 2013, pp. 487-496.

[25] K. Arioka, T. Yamada, T. Miyamoto and T. Terachi, "Dependence of Stress Corrosion Cracking of Alloy 690 on Temperature, Cold Work, and Carbide Precipitation - Role of Diffusion of Vacancies at Crack Tips", *Corrosion*, Vol.67, Iss.3, 2011, pp. 035006-035001-035006-035018.

[26] K. Arioka, R. W. Staehle, T. Yamada, T. Miyamoto and T. Terachi, "Degradation of Alloy 690 After Relatively Short Times", *Corrosion*, Vol.72, Iss.10, 2016, pp. 1252-1268.

[27] Z. Zhai, M. Toloczko, K. Kruska and S. Bruemmer, "Precursor Evolution and Stress Corrosion Cracking Initiation of Cold-Worked Alloy 690 in Simulated Pressurized Water Reactor Primary Water", *Corrosion*, Vol.73, Iss.10, 2017, pp. 1224-1236.

[28] S. M. Bruemmer, M. B. Toloczko and M. J. Olszta, *Pacific Northwest National Laboratory Investigation of Stress Corrosion Cracking in Nickel-Base Alloys, Volume 2*. Pacific Northwest National Laboratory: NUREG/CR-7103 Vol. 2, Nuclear Regulatory Commission, Office of Nuclear Regulatory Research, 2012.

[29] M. B. Toloczko, N. R. Overman, M. J. Olszta and S. M. Bruemmer, *Pacific Northwest National Laboratory Investigation of Stress Corrosion Cracking in Nickel-Base Alloys, Volume 3: Stress Corrosion Cracking of Cold-Worked Alloy 690*. Pacific Northwest National Laboratory: NUREG/CR-7103 Vol. 3, Nuclear Regulatory Commission, Office of Nuclear Regulatory Research, 2015.

[30] Z. Zhai, M. B. Toloczko, K. Kruska, D. K. Schreiber, M. J. Olszta, N. R. Overman and S. Bruemmer, *Precursor damage evolution and stress corrosion crack initiation of cold-worked alloy 690 in PWR primary water*. Pacific Northwest National Laboratory: Technical Milestone Report M2LW-16OR0402034, Light Water Reactor Sustainability Program, DOE Office of Nuclear Energy, September 2016.